

**THE NEMATIC – SMECTIC-A PHASE  
TRANSITION: A HIGH RESOLUTION  
EXPERIMENTAL STUDY.**

by

Anand Yethiraj

B.Sc., St. Xavier's College, 1988

M.S., University of Houston, 1991

THESIS SUBMITTED IN PARTIAL FULFILLMENT  
OF THE REQUIREMENTS FOR THE DEGREE OF  
DOCTOR OF PHILOSOPHY  
in the Department  
of  
Physics

© Anand Yethiraj 1999  
SIMON FRASER UNIVERSITY  
April 1999

All rights reserved. This work may not be  
reproduced in whole or in part, by photocopy  
or other means, without permission of the author.



National Library  
of Canada

Acquisitions and  
Bibliographic Services

395 Wellington Street  
Ottawa ON K1A 0N4  
Canada

Bibliothèque nationale  
du Canada

Acquisitions et  
services bibliographiques

395, rue Wellington  
Ottawa ON K1A 0N4  
Canada

*Your file* *Votre référence*

*Our file* *Notre référence*

The author has granted a non-exclusive licence allowing the National Library of Canada to reproduce, loan, distribute or sell copies of this thesis in microform, paper or electronic formats.

The author retains ownership of the copyright in this thesis. Neither the thesis nor substantial extracts from it may be printed or otherwise reproduced without the author's permission.

L'auteur a accordé une licence non exclusive permettant à la Bibliothèque nationale du Canada de reproduire, prêter, distribuer ou vendre des copies de cette thèse sous la forme de microfiche/film, de reproduction sur papier ou sur format électronique.

L'auteur conserve la propriété du droit d'auteur qui protège cette thèse. Ni la thèse ni des extraits substantiels de celle-ci ne doivent être imprimés ou autrement reproduits sans son autorisation.

0-612-51939-2

Canada

# Abstract

An important development in the theory of phase transitions was the understanding of how thermal fluctuations can alter the analytical properties of the free energy, modifying the critical exponents of a second-order phase transition. A second consequence, equally fundamental but less widely explored, is that thermal fluctuations can also change the order of the transition.

One specific mechanism for a fluctuation-induced first-order transition was proposed over two decades ago by Halperin, Lubensky and Ma (HLM). In this mechanism, the coupling between the fluctuations of a gauge field and the order parameter can convert a second-order transition into a first-order one. Such an effect is expected in two systems: in type-1 superconductors and the nematic–smectic-A (NA) transition. This effect is immeasurably small in superconductors; at the NA transition it is weak but detectable.

In this thesis, I explore the HLM effect at the NA transition experimentally. Because of the anisotropy of the nematic phase and the importance of both nematic and smectic fluctuations, this transition has remained an incompletely understood problem in condensed matter physics. The role of fluctuations is particularly interesting and complicated in the region of material-parameter space close to the Landau tricritical point (LTP), where the HLM effect is expected to be most pronounced.

I introduce a new high-resolution, real-space optical technique to probe the order of the NA transition. I have looked at the liquid crystal 8CB experimentally by measuring, using real-space imaging, the magnitude of nematic director fluctuations near  $T_{NA}$ . Although the latent heat of 8CB is smaller than the resolution of the best adiabatic calorimeters, a well-resolved, discontinuous jump in the magnitude of the fluctuations is observed on crossing the NA transition. This discontinuity is quantified by the dimensionless temperature  $t_0$ .

Theoretically, on adding an external field to the HLM theory, one finds that a modest (magnetic) field of  $\lesssim 10$  T can drive the transition in 8CB back to second order. Moreover, the theory predicts a linear suppression of  $t_0$  for small fields, with a non-analytic cusp at  $H = 0$ . Using these results, one can test this non-analytic signature of the HLM theory in detail.

Looking for this effect experimentally, I find, surprisingly, no evidence for this effect at magnetic fields up to  $\simeq 1.5$  T, implying a critical field of  $> 30$  T. This and measurements in 8CB-10CB mixtures close to the LTP put bounds on the validity of the HLM theory, while at the same time confirming quantitatively the existence of a weakly first-order regime on the “second-order” side of the LTP.

# Acknowledgments

I would like to acknowledge a number of people for having contributed, knowingly or unknowingly, to my time in Simon Fraser University and in Vancouver:

John Bechhoefer, for years of advice, encouragement, and support, and for his patience. Lab-mates Jeff Hutter, Nancy Tamblyn, Mike Degen, Ralph Giles, and Gavin Wheeler, and the visitors, Andrei Sonin, Francois Coulombe, Laurent Daudet, Wenceslao Gonzalez-Viñas, Nick Costanzino and Damien Jurine. Michael Plischke, Michael Wortis and Barbara Frisken for being available for advice and discussions. Brett Heinrich for his generous access to the electromagnet, and all those in his lab (Ken, Ted, Andrew, Radek, and Maciej) for their help. David Cannell for guidance on an early design of the gradient hot-stage, and Art Bailey, whose Ph.D. thesis was an invaluable reference. Mike Billany, who taught me machining and was always there when I needed help with machining or designing equipment. Jim Shoults in the machine shop, for putting up with me cheerfully during the design stages of my apparatus, and all the other people, past and present, at the machine shop, the glass shop, and the electronics shop. Scott Wilson, Mehrdad Rastan, and Jeff Rudd for letting me borrow lamps, lenses, and technical advice. Sada Rangekar, Sharon Beever, Candida Mazza, and Susan Roy in the Physics office, who were always helpful. The Teaching and Support Staff Union (TSSU) for providing me with a (semi-) unionised workplace. Many thanks to Mike Degen and Dan Vernon for their companionship in a window-less universe and for proof-reading this thesis, and Ranjan Mukhopadhyay for many discussions on physics and other interesting things. My other friends in Vancouver. And my brother, sister and mother. And Tali.

# Contents

<b>Approval</b>	<b>ii</b>
<b>Abstract</b>	<b>iii</b>
<b>Acknowledgments</b>	<b>v</b>
<b>Contents</b>	<b>vi</b>
<b>List of Tables</b>	<b>xi</b>
<b>List of Figures</b>	<b>xii</b>
<b>1 INTRODUCTION</b>	<b>1</b>
1.1 Phases of Matter . . . . .	1
1.2 Phase Transitions . . . . .	2
1.2.1 Entropic Phase Transitions, Thermotropics and Lyotropics . . . . .	3
1.3 The Nematic and Smectic-A Phases . . . . .	4
1.3.1 The Nematic Phase . . . . .	4
1.3.2 The Smectic-A Phase . . . . .	6
1.4 Fluctuations . . . . .	8
1.4.1 Orientational Fluctuations in the Nematic . . . . .	8
1.4.2 The Landau-Peierls Instability in the Smectic-A . . . . .	10
1.5 The Nature of the NA Transition . . . . .	10
1.5.1 Thermal Fluctuations and Transition Order . . . . .	11
1.5.2 Experimental Perspective . . . . .	12

1.5.3	Anisotropy of the NA Transition . . . . .	13
1.6	Scope of this Thesis . . . . .	14
<b>2</b>	<b>A REVIEW OF THE NA TRANSITION</b>	<b>16</b>
2.1	THEORY . . . . .	16
2.1.1	Introduction . . . . .	16
2.1.2	The Landau Free Energy . . . . .	18
2.1.3	Kobayashi-McMillan theory . . . . .	20
2.1.4	Mean-Field Theory vs. Landau theory . . . . .	21
2.1.5	A Return to Landau Theory . . . . .	22
2.1.6	Coupling of the Nematic and Smectic-A Order Parameters — The Effect of Fluctuations. . . . .	24
2.1.7	A Field-Induced Tricritical Point . . . . .	28
2.1.8	The analogy with superconductivity . . . . .	28
2.1.9	The H L M Effect . . . . .	32
2.1.10	Monte Carlo Simulations of the de Gennes Model . . . . .	32
2.1.11	The “Laplace” Model: A Modification of the de Gennes Model . . . . .	33
2.1.12	The Nelson-Toner (Dislocation-Unbinding) Model . . . . .	34
2.1.13	Anisotropic Scaling . . . . .	35
2.1.14	Weak Anisotropy of the NA Transition . . . . .	36
2.1.15	Theoretical Summary . . . . .	36
2.2	EXPERIMENT . . . . .	37
2.2.1	Introduction . . . . .	37
2.2.2	Ways to probe tricritical behaviour . . . . .	39
2.2.3	X-ray structure factor measurements . . . . .	40
2.2.4	Elastic constant measurements . . . . .	41
2.2.5	Heat capacity measurements . . . . .	44
2.2.6	Front velocity measurements . . . . .	46
2.2.7	Capillary-length measurements . . . . .	46
2.2.8	Thermal transport measurements . . . . .	46
2.2.9	Effects of an external field on the NA transition . . . . .	47
2.3	Conclusion: Assessment of the current understanding of the NA transition . . . . .	50

2.3.1	Near the “Type-2” limit. . . . .	50
2.3.2	Near the “Type-1” limit . . . . .	51
<b>3</b>	<b>THE “HLM” MECHANISM IN AN EXTERNAL FIELD</b>	<b>52</b>
3.1	Introduction . . . . .	52
3.2	Derivation of the HLM effect . . . . .	53
<b>4</b>	<b>EXPERIMENTAL APPARATUS AND TECHNIQUES</b>	<b>61</b>
4.1	The Design of a Real-Space Technique . . . . .	61
4.1.1	Motivation for a study in real-space. . . . .	61
4.1.2	Quantitative Microscopy . . . . .	63
4.2	The Optical System . . . . .	66
4.2.1	Optics . . . . .	67
4.2.2	Optical Adjustments . . . . .	71
4.2.3	Depth of Field . . . . .	72
4.3	The Sample Hot Stage — Elements and Design . . . . .	73
4.4	Temperature Control . . . . .	75
4.4.1	Hardware . . . . .	75
4.4.2	Software . . . . .	78
4.4.3	A Summary of the Temperature Control System . . . . .	81
4.4.4	Applied Temperature Gradient . . . . .	82
4.4.5	Unwanted Temperature Gradients . . . . .	82
4.5	Sample Preparation . . . . .	83
4.5.1	Glass cleaning . . . . .	84
4.5.2	Surface Treatment of the Glass Cubes or Slides . . . . .	85
4.5.3	Thickness adjustment and measurement . . . . .	88
4.5.4	Polishing of the Copper Surfaces . . . . .	88
4.5.5	Glue . . . . .	89
4.5.6	Liquid crystal purification and filling . . . . .	89
4.6	Preparation of Liquid Crystal Mixtures . . . . .	89
4.7	Summary . . . . .	91

<b>5</b>	<b>INTENSITY FLUCTUATION MICROSCOPY: CALIBRATIONS</b>	<b>92</b>
5.1	Characterising the Intensity Fluctuations . . . . .	92
5.1.1	Introduction . . . . .	92
5.1.2	The signal and the noise . . . . .	92
5.1.3	Variances in the isotropic, nematic and smectic-A Phases . . . . .	96
5.1.4	Dependence of $\hat{\zeta}$ on the incident light intensity . . . . .	97
5.1.5	Angle dependence in the nematic phase . . . . .	100
5.1.6	Thickness dependence . . . . .	103
5.1.7	A closer look at intensity fluctuations . . . . .	107
5.1.8	Spatial and temporal averaging in the imaging . . . . .	109
5.2	The gradient trick . . . . .	111
5.3	Summary . . . . .	113
<b>6</b>	<b>INTENSITY FLUCTUATION MICROSCOPY: RESULTS</b>	<b>114</b>
6.1	Introduction . . . . .	114
6.2	Fluctuations in 8CB . . . . .	115
6.2.1	Zero-Field Measurements . . . . .	115
6.2.2	Magnetic Field Measurements . . . . .	122
6.2.3	Summary of Results in 8CB . . . . .	126
6.3	The effect of varying thickness . . . . .	127
6.4	Measurements at the LTP . . . . .	133
6.5	The variation of the first-order discontinuity in 8CB-10CB mixtures . . . . .	133
6.5.1	Zero-field results in 8CB-10CB mixtures . . . . .	134
6.6	A Note on Errors . . . . .	137
6.7	Summary of Results . . . . .	138
6.7.1	Zero-field Results in 8CB . . . . .	138
6.7.2	Zero-field Results in 8CB-10CB mixtures . . . . .	138
6.7.3	Magnetic-Field Studies . . . . .	139
6.7.4	Thickness Studies . . . . .	140
<b>7</b>	<b>CONCLUSIONS AND FUTURE DIRECTIONS</b>	<b>141</b>

<b>Appendices</b>	<b>146</b>
<b>A 8CB MATERIAL PARAMETERS</b>	<b>146</b>
A.1 Structure and Properties of 8CB and 10CB . . . . .	146
A.2 8CB-10CB Phase Diagram . . . . .	147
A.3 Temperature dependence of Elastic constants and Correlation Lengths . . . .	148
<b>B LANDAU THEORY ESTIMATES</b>	<b>153</b>
B.1 Introduction . . . . .	153
B.1.1 Latent-heats . . . . .	154
B.1.2 Front Velocity . . . . .	156
B.1.3 Capillary Length . . . . .	157
B.1.4 Electric Field Studies . . . . .	157
B.1.5 Intensity Fluctuation Microscopy . . . . .	158
<b>Bibliography</b>	<b>159</b>

# List of Tables

2.1	Critical exponents. . . . .	23
2.2	Superconducting analogy . . . . .	29
2.3	Chemical structures . . . . .	37
4.1	Materials table . . . . .	74
6.1	Fitted value of $C_0$ for different choices of the exponent $\bar{\nu}$ . . . . .	136
6.2	Table of $t_0$ for different mixtures. . . . .	139
A.1	Phase Sequence . . . . .	146

# List of Figures

1.1	A cartoon of molecular ordering in the nematic and smectic-A phases. . . . .	4
1.2	The elastic deformations in a nematic. . . . .	5
1.3	Nematic splay accommodates smectic-A layer bending. . . . .	7
1.4	The two-component smectic order parameter. . . . .	8
1.5	The specific-heat exponent in various liquid crystalline materials . . . . .	12
2.1	Free energy landscape for a continuous (second-order) transition. . . . .	19
2.2	Free energy landscape for a first-order transition. . . . .	20
2.3	The nematic order parameter magnitude $S$ as a function of temperature. . . . .	25
2.4	A small rotation corresponds to layer displacement. . . . .	27
2.5	Experimental values for smectic susceptibility and correlation length exponents	38
2.6	Crossover from linear to nonlinear dependence of the latent heat on mixture concentration. . . . .	45
3.1	Plot of $t_0$ as a function of the scaled magnetic field. . . . .	58
3.2	The (scaled) smectic order parameter $\psi_0$ at the transition as a function of $H$ .	59
4.1	Sample geometry. (a) Side view: light direction is from left to right. (b) Front view: light direction is into the paper. (c) Expanded region of (a) in the liquid crystal gap between the glass substrates. . . . .	64
4.2	Sample at a distance. . . . .	65
4.3	Schematic of the optical system. . . . .	66
4.4	Flashlamp spectral output. . . . .	67
4.5	CCD spectral response. . . . .	70

4.6	The depth of field has a wave-optics contribution and a geometric-optics contribution. The depth of field for the $N.A. = 0.25$ optics in this experiment is $\approx 20 \mu\text{m}$ . . . . .	73
4.7	Schematic of gradient hot stage. . . . .	75
4.8	Measurement of “proportional droop” in the temperature-control system. . .	79
4.9	Schematic of temperature control system. . . . .	80
4.10	A time-series of the measured temperature. . . . .	82
4.11	Two cause of interface smearing. . . . .	83
4.12	Apparatus for unidirectionally dip-coating glass with a polyimide-precursor solution. (a) Front view. (b) Side view showing glass and beaker with polyimide solution. . . . .	86
4.13	Interferometric set-up to measure and correct thickness gradients. . . . .	87
4.14	The nematic range as a function of mixture concentration in the 8CB-10CB system. . . . .	90
5.1	A “difference” image showing the NA interface. . . . .	93
5.2	Histogram of the intensity distribution of a $100 \times 100$ square-pixel region at $T - T_{NA} \approx 0.1K$ . $\Delta = I_1 - I_2$ , and $\langle I \rangle$ is the average intensity of an instantaneous image. The probability weight is normalised so as to give the distribution unit area. . . . .	95
5.3	Probability distribution functions in the nematic and smectic-A phases, and in a blank field. . . . .	97
5.4	The variance $\hat{\zeta}$ as a function of the mean intensity. . . . .	98
5.5	Mean intensity and variance as a function of $\theta$ . . . . .	101
5.6	Intensity distributions for different angles. . . . .	102
5.7	A schematic of the fluctuation profile across the thickness of the sample. The signal collected typically integrates over this profile. . . . .	104
5.8	A schematic diagram of the wedge sample. . . . .	105
5.9	The thickness dependence of the mean intensity and the normalised fluctuations in the wedge sample. (a) Mean intensity, normalised to the saturation value of the CCD. (b) Normalised fluctuations. . . . .	105

5.10	The peak-to-peak oscillation in the fluctuations, $\Delta\zeta_{peak-peak}$ , gets progressively washed out with increasing thickness. . . . .	106
5.11	The autocorrelation function. . . . .	109
5.12	Increase in fluctuation sensitivity as the exposure time gets smaller. $\zeta^{-1}$ scales linearly with the exposure time. . . . .	110
6.1	Interface Calibration for Sample 1 . . . . .	117
6.2	Interface Calibration for Sample 2 . . . . .	117
6.3	Sample 1: $\zeta$ vs. $T - T_{NA}$ . . . . .	118
6.4	Sample 1: $\log_{10} \zeta$ vs. $\log_{10}(T - T_{NA})$ . . . . .	119
6.5	Data from Fig. 6.3 fit to a convolution of a power law with a temperature gradient. The top curve in the graph shows the residuals between the data and the convolution fit. . . . .	121
6.6	Sample 2: $\zeta$ vs. $T - T_{NA}$ . . . . .	123
6.7	Magnetic-Field Effect in 8CB: Sample 2 . . . . .	124
6.8	The non-critical magnetic-field effect. . . . .	125
6.9	The field-induced suppression at different temperatures . . . . .	125
6.10	Temperature-dependence of the field-suppression coefficient $g_H$ . . . . .	126
6.11	Discontinuity in the mean intensity in the 8CB wedge sample. . . . .	128
6.12	Temperature-dependence of fluctuations in the 8CB wedge sample. . . . .	130
6.13	The dependence of $t_0$ on thickness $d$ . . . . .	131
6.14	Fluctuations in at the LTP for $H = 0$ T and $H = 1.2$ T. . . . .	133
6.15	$g_H$ vs. $T - T_{NA}$ . . . . .	134
6.16	Fit of $t_0$ data (this thesis) to Anisimov parameters. . . . .	135
6.17	Latent-heat estimate based on the fitted Landau parameters. Also shown is the HLM fit and the latent-heat data of Marynissen <i>et al.</i> . . . . .	137
A.1	Chemical structure of 8CB and 10CB. . . . .	147
A.2	8CB-10CB phase diagram. . . . .	147
A.3	Correlation lengths $\xi$ vs. $t$ . . . . .	148
A.4	Temperature dependence of $K_1$ , $K_2$ , and $K_3$ vs. $t$ . . . . .	149
A.5	Temperature dependence of $S$ vs. $t$ . . . . .	150
A.6	Temperature dependence of $S$ vs. $t$ , close to $T_{NA}$ . . . . .	150

A.7 Temperature dependence of  $S$ ,  $\Delta\epsilon$ , and  $\Delta\chi$  vs. reduced temperature  $t$ . . . . . 151

A.8 Thermal conductivity vs. Temperature. . . . . 152

A.9 Thermal diffusivity vs. Temperature. . . . . 152

B.1 Fit of latent heat data (Marynissen *et al.* ) to the Anisimov parameters. . . . . 156

# Chapter 1

## INTRODUCTION

*An introduction to phase transitions, liquid crystals, the nematic and smectic-A phases, and the nematic–smectic-A phase transition. An outline of the main unresolved issues and a guide to the thesis that follows.*

### 1.1 Phases of Matter

Much of the world around us can be classified into three phases of matter: the air we breathe is a gas, the water we drink is a liquid, and earth we walk on is a solid. The word “phase” refers to the idea that the state of matter can be changed from gas to liquid to solid by varying environmental parameters (such as pressure, concentration or temperature).

The gaseous and liquid state are *fluid*—they are formless. They are also isotropic (having no preferred direction in space), and the molecules in the fluid have no long-range orientational order. The solid state is distinguished from fluids by having three-dimensional positional order. Because of this, solids have form.

Liquid crystals are materials that exhibit phases of matter which have some liquid-like and some solid-like properties; these liquid-crystalline phases have some degree of order between that of isotropic liquids (which have none) and three-dimensional solid crystals.<sup>1</sup> Liquid-crystalline materials are, in fact, ubiquitous: the lipid bilayer in red-blood cells is liquid crystalline, and materials that make up liquid crystals can be found in soap, polymers,

---

<sup>1</sup>For a simple introduction to liquid crystals, see Ref. [1], and see Refs. [2, 3, 4] for a more advanced treatment.

and tomato blight.

## 1.2 Phase Transitions

Phase transitions are dramatic collective events where macroscopic quantities are drastically affected over a small range of temperature (or any other external parameter, such as pressure, concentration, etc.).

The first conceptual leap in understanding phase transitions is the idea that both phases (one can think of liquid and solid for concreteness) and the phase transition separating them can all be described by a single free energy function. This free energy is a sum of energetic and entropic parts,

$$F = U - T S, \quad (1.1)$$

where  $U$  is the internal energy arising from the attractive interactions,  $T$  is the temperature, and  $S$  is the entropy. At zero temperature, the free energy is minimised by minimising just the internal energy, and thus the system finds its most ordered state. Typically, the ordered phase has lower entropy, while the disordered state has higher entropy—there are usually many more ways to make a disordered state than an ordered state. At finite temperature, there is a competition between energy and entropy, and the system may make a transition to less-ordered states so as to minimise the free energy. The phase transition is a non-analytic point of the free energy function  $F$ . The non-analyticity of  $F$ , in turn, arises from the notion of the thermodynamic limit, wherein one postulates that the number of atoms or molecules involved in the phase change is large enough as to be physically indistinguishable from infinity.

In particular, these transitions can be either “first order,” where the first derivatives of the free energy, like the entropy, are discontinuous, or “continuous,” (also often referred to as second-order transitions) where these first-order derivatives are continuous. At a continuous transition, the correlation length (and any first derivative of thermodynamic extensive quantities) diverges. The universal scaling laws of systems close to a continuous transition are termed “critical phenomena,” and the exponents of the respective power laws are termed “critical exponents.”

The entropy jump in a first-order transition is proportional to the latent heat; it is the heat absorbed by the system in order to change phase. At a first-order transition, the

correlation length does not diverge but stays finite.

Materials with liquid-crystalline phases provide interesting model systems for phase transitions because they exhibit discrete changes in ordering, from a completely disordered liquid to a complete three-dimensionally ordered solid, with several possible intermediate phases of ordering in less than three dimensions. Moreover, they provide physical realisations [5] of *purely entropic* phase transitions—where the internal energy need not play a part.

### 1.2.1 Entropic Phase Transitions, Thermotropics and Lyotropics

Typically, the higher-entropy state is more disordered; however, there are exceptions. A simple example is that of packing a suitcase with clothes [6]. There are certainly many more ways to put in clothes in a disordered way than in an ordered way. But when you add the constraint that the suitcase be closed, the situation changes. For low densities, the disordered state is still entropically preferred. But for high enough densities, there will eventually be *no way* that one can shut the suitcase, without folding the clothes. In contrast, there are still several ways to arrange the folded clothes. Thus, in this case, the more-ordered folded state is preferred entropically. The trade-off here is between three-dimensional translational entropy and an entropy of reduced dimensionality. This trade-off always exists in liquid crystal phase transitions, even when attractive interactions are also present.

A solution of a liquid-crystalline material in a solvent provides a simple way to change the packing density of molecules, simply by changing the concentration. A system of this kind is called a *lyotropic* liquid crystal. The solvent can also play the role of screening the attractive interactions, and thus a lyotropic liquid crystal can be made athermal.<sup>2</sup>

In a *thermotropic* liquid crystal, on the other hand, attractive interactions are indeed important, and the phase transition is driven by varying the temperature. Here, both energetic and competing entropic effects are important. This is therefore the more generic case, and a vast number of liquid crystals, including those in this study, are thermotropic.

In regular “hard” solids, the free energy is dominated by the internal energy  $U$ , and thermal fluctuations can be treated as a perturbation about a minimum-energy state. In liquid crystals (and soft materials, in general), the entropic effects are large, and thermal

---

<sup>2</sup>Temperature does not affect a phase transition that is driven purely by entropic effects.

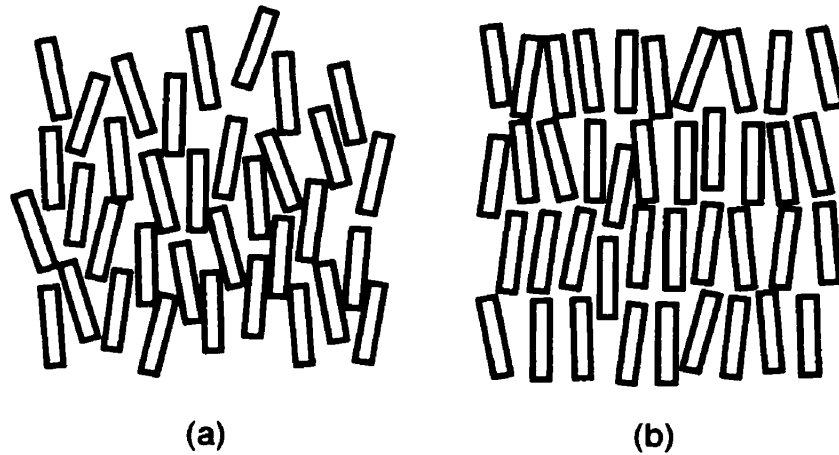


Figure 1.1: (a) Orientational ordering in the nematic. (b) Orientational ordering and layering in the smectic-A.

fluctuations are important. Liquid crystals are therefore good model systems in which to study the effects of thermal fluctuations.

## 1.3 The Nematic and Smectic-A Phases

### 1.3.1 The Nematic Phase

Materials that exhibit a nematic phase are often composed of elongated or rod-like molecules, or some other characteristic form of molecular anisotropy. The nematic phase has long-range orientational order but no long-range positional order: a cartoon of this ordering is shown in Fig. 1.1(a). The phase transition from isotropic liquid to nematic liquid crystal (the IN transition) is driven by both subtle competing entropic effects, and anisotropic attractive interactions. Decreasing the temperature is equivalent to increasing the mass density. This energetically favours the rods' lining up. There is also a gain in translational entropy. On cooling, these two effects compete with the loss in rotational entropy.

#### The nematic order parameter

The order parameter in the nematic can be written as a symmetric, traceless two-tensor  $Q_{\alpha\beta} = S(3n_\alpha n_\beta - \delta_{\alpha\beta})/2$  (the normalisation is chosen so that  $Q_{zz} = 1$  when  $S = 1$ ,

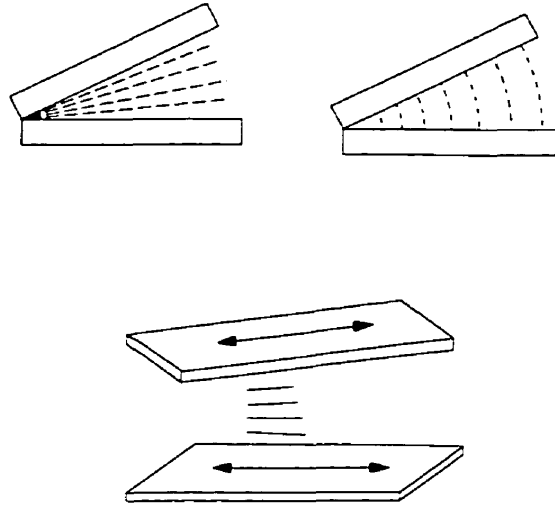


Figure 1.2: Splay, bend and twist in the nematic. The dashed lines represent the molecular orientation in the bulk which is influenced by the boundary conditions at the surfaces.

which in turn corresponds to a perfect ordering of the molecules along the  $\hat{z}$  direction). Here  $S$  is a scalar that sets the magnitude and  $\hat{n}$  is a unit vector that sets the direction of the orientational ordering. The order parameter is symmetric under the operation  $\hat{n} \rightarrow -\hat{n}$ .<sup>3</sup> This order can be seen in all macroscopic tensor properties. For example, a nematic is birefringent, with its optic axis along  $\hat{n}$ . When an isotropic liquid is cooled into the nematic phase, three-dimensional rotational symmetry is spontaneously broken, and the average direction picked out is usually governed by weaker surface anchoring effects. This has two outcomes: First, one can easily make a single domain nematic (analogous to a single crystal in solid-state physics) by controlling the surface treatment of the bounding surfaces. Second, long-wavelength orientational fluctuations cost little energy, i.e. they are a soft mode in the nematic. Because of this, the nematic has only partial orientational order. This partial order is illustrated in Fig. 1.1 (a) where there is a variation in the direction that the rods point—the average direction is denoted by  $\hat{n}$ .

<sup>3</sup>Because of the  $\hat{n} \rightarrow -\hat{n}$  symmetry, one cannot use a simpler vector order parameter. See Ref. [2], Chapter 2.

### Elastic deformations in the nematic

The nematic has anisotropic elasticity, and the elastic modulus is a tensorial quantity [7, 8, 9]. In a uniaxial nematic, the elasticity can be decomposed into three modes: splay, bend and twist, pictorially depicted in Fig. 1.2. The three corresponding elastic constants  $K_1, K_2, K_3$  of a nematic (called Frank constants) typically have an order of magnitude that is not too different from  $K \simeq k_B T / L$ , where  $L$  is a molecular length.<sup>4</sup> Taking  $L \simeq 1$  nm, one gets

$$\begin{aligned} K &\simeq 4 (\text{pN})(\text{nm}) / 1 \text{ nm}, \\ &\simeq 4 \times 10^{-7} \text{ dynes}. \end{aligned} \quad (1.2)$$

The bulk deformation energy of the nematic can be completely described as a combination of these 3 distortion modes. This is the Frank-Oseen free energy density [7, 8, 9] (see also Ref. [2]) :

$$f_N = \frac{1}{2} K_1 (\nabla \cdot \hat{n})^2 + \frac{1}{2} K_2 (\hat{n} \cdot \nabla \times \hat{n})^2 + \frac{1}{2} K_3 (\hat{n} \times (\nabla \times \hat{n}))^2. \quad (1.3)$$

### 1.3.2 The Smectic-A Phase

In the smectic-A phase, there is also a layering along the average director, giving the material one-dimensional positional order as well as orientational order. A cartoon of the molecular ordering in the smectic-A is shown in Fig. 1.1(b). At lower temperature, the layered phase is favoured energetically relative to the nematic phase, because of a competition between energy and in-plane translational entropy on one hand against out-of-plane translational entropy on the other.

### Elastic deformations in the smectic-A

The layer structure poses a restriction on the kind of deformations allowed in the smectic. Compressing the layers requires considerable energy; one can assume that they are incompressible. Then, the integral

$$\frac{1}{d} \int_A^B \hat{n} \cdot d\mathbf{r} \quad (1.4)$$

---

<sup>4</sup>As we shall see, near the NA transition,  $K_2$  and  $K_3$  may be much larger than this estimate. See Section 2.1.13.

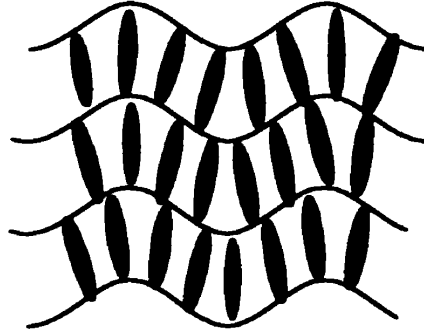


Figure 1.3: Nematic splay accomodates layer bending in the smectic.

represents the number of layers crossed on going from A to B, where  $d$  is the layer thickness. For a closed loop

$$\oint \hat{n} \cdot d\mathbf{r} = 0 \implies \nabla \times \hat{n} = 0. \quad (1.5)$$

Thus, both twist and bend distortions are expelled in an incompressible smectic. The splay deformation, however, is allowed and corresponds to layer bending.

In a real smectic, for small layer displacements  $u$ , one can write down the smectic free-energy density to lowest order:

$$f_{Sm} \simeq \frac{1}{2}B \left( \frac{\partial u}{\partial z} \right)^2 + \frac{1}{2}K_1 \left[ \left( \frac{\partial^2 u}{\partial x^2} + \frac{\partial^2 u}{\partial y^2} \right) \right]^2, \quad (1.6)$$

where typically the layer compressibility,  $B \simeq 10^7$  dyne/cm<sup>2</sup>, and the splay constant  $K_1 \simeq 10^{-6}$  dyne. The first term makes it hard for the layer spacing to change from its equilibrium value ( $u = 0$ ). The second term, which is equivalent to the splay term in the nematic, is the energetic cost of layer bending (see Fig. 1.3).

### The smectic order parameter

As a result of the importance of layer fluctuations, the picture of thermotropic smectics as being organised in well-defined layers is modified; in fact, the smectic ordering can be described by a sinusoidal density modulation in the layering direction.<sup>5</sup> (See Fig. 1.4).

<sup>5</sup>In contrast, recent studies in virus solutions, which are lyotropics, have found smectics with very well-defined layers. Here the density modulation is not well-described by a sinusoidal modulation. With  $\mu\text{m}$ -size rod lengths, and sample sizes of  $O(\mu\text{m})$  as well,  $\langle u^2(r) \rangle$  in this case is a factor of 10 lower. See Ref. [5] for a review of experiments on phase transitions in virus solutions.

Higher harmonics can be ignored; the second-order diffraction of the Bragg peak in X-ray scattering is usually a few orders of magnitude weaker than the first harmonic [10]. One can write

$$\rho(\mathbf{r}) = \rho(z) = \rho_0 + \rho_1 \cos(q_0 z - \phi), \quad (1.7)$$

where  $\rho_1$  is the first harmonic of the density modulation and  $\phi$  is an arbitrary phase, reflecting the choice of origin. In the nematic,  $\rho_1 = 0$ . Smectic order is therefore characterised by the numbers  $\rho_1$  and  $\phi$ . This can be written more elegantly as a complex order parameter

$$\psi(r) = \rho_1(r) e^{-i\phi(r)}, \quad (1.8)$$

where we have in addition allowed the order parameter to be spatially varying on length scales that are large compared to the layer repeat spacing.

Because of the suppression of twist and bend fluctuations, the smectic, in addition to translational order, also has a stronger orientational order than the nematic.

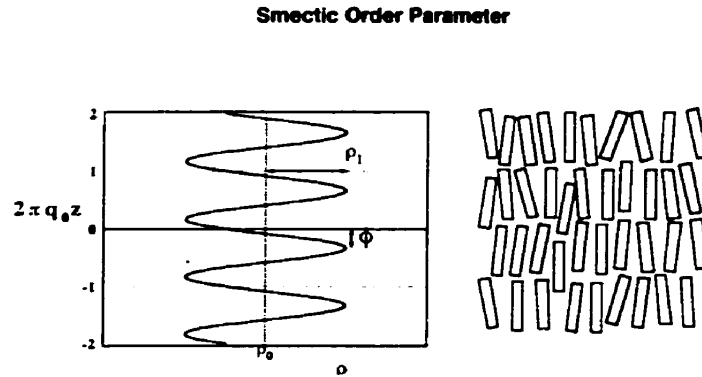


Figure 1.4: The two-component smectic order parameter.

## 1.4 Fluctuations

### 1.4.1 Orientational Fluctuations in the Nematic

It is useful and pertinent to discussions that follow to briefly sketch the form of the correlation function in the nematic phase.<sup>6</sup> The Frank-Oseen free energy density (Eq. 1.3) can be

<sup>6</sup>This subsection follows the treatment in Ref. [2] very closely.

expanded to second order in  $n_x$  and  $n_y$ . Writing the free energy to second order, we have

$$F_N = \frac{1}{2} \int d^3x \left\{ K_1 \left( \frac{\partial n_x}{\partial x} + \frac{\partial n_y}{\partial y} \right)^2 + K_2 \left( \frac{\partial n_x}{\partial y} - \frac{\partial n_y}{\partial x} \right)^2 + K_3 \left[ \left( \frac{\partial n_x}{\partial z} \right)^2 + \left( \frac{\partial n_y}{\partial z} \right)^2 \right] \right\}. \quad (1.9)$$

Imposing a magnetic field  $H$  along  $\hat{z}$  will add a term,

$$F_{mag} = \frac{1}{2} \int d^3x \chi_a H^2 (n_x^2 + n_y^2) + \text{constant}, \quad (1.10)$$

where  $\chi_a$  is the anisotropic part of the diamagnetic susceptibility. Note that this term is the lowest order analytic term that is independent of the up-down orientation of the field or of the director. In Fourier space, we can define  $n_x(\mathbf{q}) = \int n_x(\mathbf{r}) e^{i\mathbf{q}\cdot\mathbf{r}}$ , and  $n_y(\mathbf{q}) = \int n_y(\mathbf{r}) e^{i\mathbf{q}\cdot\mathbf{r}}$ , and the free energy then becomes

$$F = \frac{1}{2} V^{-1} \sum_{\mathbf{q}} \left\{ K_1 |n_x(\mathbf{q})q_x + n_y(\mathbf{q})q_y|^2 + K_2 |n_x(\mathbf{q})q_y + n_y(\mathbf{q})q_x|^2 + (K_3 q_z^2 + \chi_a H^2) \{ |n_x(\mathbf{q})|^2 + |n_y(\mathbf{q})|^2 \} \right\}. \quad (1.11)$$

This expression takes on a diagonal form if we replace  $(n_x, n_y)$  with  $(n_1, n_2)$ , defined by  $n_\alpha = \hat{n} \cdot \hat{\mathbf{e}}_\alpha$ , where  $\hat{\mathbf{e}}_1$  and  $\hat{\mathbf{e}}_2$  are unit vectors in the  $(x, y)$  plane such that  $\hat{\mathbf{e}}_2 \cdot \mathbf{q} = 0$ , and  $\hat{\mathbf{e}}_1 \cdot \hat{\mathbf{e}}_2 = 0$ . In its diagonalised form, the free energy is

$$F = \frac{1}{2} V^{-1} \sum_{\mathbf{q}} \sum_{\alpha=1,2} |n_\alpha(\mathbf{q})|^2 (K_3 q_{\parallel}^2 + K_\alpha q_{\perp}^2 + \chi_a H^2). \quad (1.12)$$

From the equipartition theorem, the average free energy in thermal equilibrium per degree of freedom is  $\frac{1}{2} k_B T$ . This allows us to obtain an expression for the ensemble average of the director-director correlation functions:

$$\langle |n_\alpha(\mathbf{q})|^2 \rangle = \frac{V k_B T}{K_3 q_{\parallel}^2 + K_\alpha q_{\perp}^2 + \chi_a H^2}. \quad (1.13)$$

The two-point correlation function  $\langle n_x(\mathbf{r}_1) n_x(\mathbf{r}_2) \rangle$  can now be calculated; the calculation is simplified by using the one-constant approximation, i.e. setting  $K_1 = K_2 = K_3 = K$ , and the result is

$$\begin{aligned} \langle n_x(\mathbf{r}_1) n_x(\mathbf{r}_2) \rangle &= \langle n_y(\mathbf{r}_1) n_y(\mathbf{r}_2) \rangle = (2V)^{-2} \sum_{\mathbf{q}} \langle |n_1(\mathbf{q})|^2 + |n_2(\mathbf{q})|^2 \rangle \exp(-i\mathbf{q} \cdot \mathbf{R}) \\ &= (2\pi)^{-3} \int d^3q \frac{k_B T}{K(q^2 + \xi_H^{-2})} \exp(-i\mathbf{q} \cdot \mathbf{r}) \\ &= \left( \frac{k_B T}{4\pi K R} \right) \exp(-R/\xi_H), \end{aligned} \quad (1.14)$$

where  $\mathbf{R} = \mathbf{r}_1 - \mathbf{r}_2$ , and  $\xi_H = \sqrt{\frac{K}{\chi_a}} \frac{1}{|H|}$  is the magnetic coherence length.

When a field is present, the range of correlations is set by the magnetic coherence length  $\xi_H$ . All fluctuations of length-scale greater than  $\xi_H$  are suppressed by the field. In this case the fluctuations are said (in the language of field theory) to be “massive.” In zero field, there is no characteristic length above which the correlations die out rapidly. Here, the fluctuations are “massless.” This property of the correlation function is generic to systems featuring a spontaneously broken continuous symmetry; in the nematic case, it is three-dimensional rotational symmetry that is broken on going through the isotropic-nematic (IN) transition.

### 1.4.2 The Landau-Peierls Instability in the Smectic-A

Writing the free energy of Eq. 1.6 in terms of the Fourier components of  $u$  and applying the equipartition theorem, we get

$$\langle |u_q|^2 \rangle = \frac{K_B T}{Bq_z^2 + K_1 q_\perp^4}. \quad (1.15)$$

From this, we can get the mean-square fluctuation

$$\langle u^2(r) \rangle = \frac{K_B T}{4\pi(BK_1)^{\frac{1}{2}}} \ln \left( \frac{\ell}{d_0} \right), \quad (1.16)$$

where  $d_0$  is the layer spacing and  $\ell$  is the sample dimension.

Putting in numbers, one finds that the sample dimension where the layer fluctuations become comparable to the layer spacing is about 1 metre. Most samples studied are on the centimetre scale or less.<sup>7</sup>

## 1.5 The Nature of the NA Transition

In Chapter 3, the importance of coupling between the nematic and smectic order parameter at the NA transition is discussed in detail. However, if one simply-mindedly ignores this coupling and considers a Landau expansion only in  $\psi$ , one can immediately guess the universality class of the phase transition from the dimensionality of the order parameter ( $n = 2$ ) and that of the space in which the liquid crystal lives ( $d = 3$ ). The transition

---

<sup>7</sup>Typical sample thicknesses for microscopy range from 10 – 100 $\mu\text{m}$ .

would then be expected to fall into the 3DXY universality class. All the subtleties of the NA transition can be phrased in terms of deviation from 3DXY behaviour.

### 1.5.1 Thermal Fluctuations and Transition Order

One of the most important advances made in our understanding of phase transitions in the last few decades has been the effects of thermal fluctuations on critical phenomena. The most celebrated of these effects is the modification of critical exponents from the values predicted by mean-field theory, an effect understood via an application of the renormalisation group [11, 12, 13].

But thermal fluctuations have another effect [13], one that is less-well-understood theoretically, and only studied to a limited extent experimentally: when two order parameters are simultaneously present and interact with each other, the fluctuations of one may drive the phase transition of the other first order. The strong deviation from second-order 3DXY behaviour at the NA transition in a number of liquid-crystalline materials, prompts a serious consideration of such fluctuation effects at the NA transition. Over two decades ago, Halperin, Lubensky and Ma (HLM) [14] proposed an unusual mechanism, wherein the coupling of a gauge field to the order parameter drove a second-order transition first order. This was predicted to occur in two settings: the normal-superconducting phase transition in type-1 superconductors and the NA transition in liquid crystals. There exists a very useful analogy between the normal-superconducting and the NA transitions which is discussed in detail in Chapter 2. Here, we simply note that in both the superconductor and the smectic settings, the transition is predicted to be *always* at least weakly first order. The strength of “first-order-ness” is given by the size of the discontinuity; e.g., one measure would be the temperature difference between the transition point and the spinodal point,  $\Delta T$ . In superconductors,  $\Delta T$  is at most a few microKelvin, but at the NA transition, it is estimated to be on the order of several milliKelvin and is therefore more accessible to experiment.

At the NA transition, there is very suggestive evidence [15, 16] arguing for the existence of this effect; it does not, however, preclude another fluctuation mechanism. In particular, the HLM mechanism does not take into account smectic fluctuations,<sup>8</sup> and a more detailed

---

<sup>8</sup>The neglect of smectic fluctuations at the NA transition is only valid for very small nematic range (the

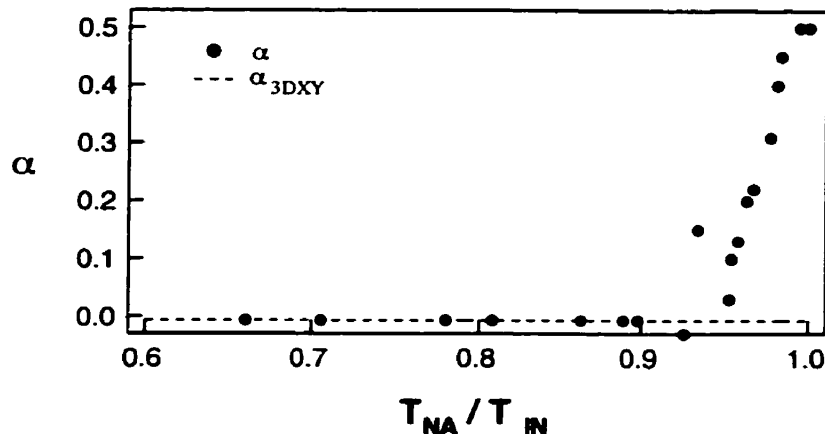


Figure 1.5: Specific-heat exponent obtained by calorimetry on various different liquid-crystalline materials (from Ref. [17]).

experimental check of the HLM theory is desirable. Such a check is also quite plausible, since the HLM mechanism modifies the structure of the free energy, making it non-analytic. To look for this non-analytic signature, one can study theoretically the effect of an external magnetic (or electric) field; the field-dependence then gives a detailed prediction based on the HLM effect, which one can then look for experimentally. This is the programme, with a primarily experimental motivation, that underlies this thesis.

### 1.5.2 Experimental Perspective

In comparing experiments at the NA transition with expected exponents in the 3DXY universality class, it is instructive to compare the experimental status with that for other critical phenomena. A comparison of the specific-heat exponent at the NA transition, defined by

$$C \sim t^{-\alpha}, \quad (1.17)$$

where  $t = (T - T_{NA})/T_{NA}$  is the reduced temperature,<sup>9</sup> with that at the lambda transition of helium, is instructive. The specific heat exponent at the NA transition is a function of analog in superconductors is the strongly type-1 limit.) In the opposite limit, for very large nematic range (the analog in superconductors being the type-2 limit), one can neglect nematic fluctuations and consider only smectic fluctuations. In this limit the transition is expected to be second-order XY. A general treatment of both nematic and smectic fluctuations remains an open problem.

<sup>9</sup>We define  $t = (T - T^*)/T^*$ ; at a continuous transition,  $T^* = T_{NA}$ .

material parameters. We see in Fig. 1.5, that varying the nematic range (parametrised by the dimensionless number  $T_{NA}/T_{NI}$ ) continuously varies the apparent specific heat exponent from  $\alpha \approx 0$  to  $\alpha \approx 0.5$ . Clearly this spread of values must be taken into account before comparing data. The  $\alpha \approx 0$  limit is one where the transition is indistinguishable from second order, while the  $\alpha \approx 0.5$  limit is in the region where the transition is weakly first order. Restricting ourselves to the large nematic range, “second-order” limit, we find that the specific heat value  $\alpha = 0 \pm 0.06$ . While this is in agreement with the theoretically predicted value  $\alpha = -0.007$ , the large uncertainty in the experimental values is the primary barrier to a more sensitive test of the theory.

At the lambda transition, the precision is an order of magnitude better. The experimental value, obtained from high-resolution heat-capacity measurements [18], is  $\alpha = -0.0127 \pm 0.0026$ . This allows a much more sensitive test of deviations from the theoretical value, from renormalisation-group calculations, of  $\alpha = -0.007 \pm 0.006$ . In this case, it is the confidence levels in the theoretical value that is the limiting factor.

Since the uncertainties in the NA transition exponents are an order of magnitude larger, any statements of agreement with theory are substantially weaker. On the other hand, we will see in the next chapter that even with this larger uncertainty, the correlation length exponents show qualitative disagreement with theoretical 3DXY predictions. This highlights the fact that, in spite of broad aspects of agreement between experiments and theory, there remain profound unresolved issues at the NA transition.

### 1.5.3 Anisotropy of the NA Transition

Even in materials that lie on the “clearly second-order” side, there is an unambiguous, but weak, anisotropy of the critical exponents. The correlation lengths parallel and perpendicular to the director both diverge on approaching the phase transition. This divergence is even seen when the transition is first order, because the discontinuity strength is weak enough to observe pretransitional effects. Although there are explanations for this phenomenon (discussed in the next chapter), there is no solid theory.

## 1.6 Scope of this Thesis

To go beyond mean-field theory, one must simultaneously take into account fluctuations in the nematic as well as the smectic-A. Theoretical efforts in this direction have begun [19]. Experimentally, improved experimental resolution could make the critical region accessible. In fact, the fundamental question of the order of the transition remains only partially answered. In this work, we address the following issues:

1. We have designed a new real-space technique that is at least ten times more sensitive than current calorimetric techniques or existing scattering techniques. This increased sensitivity is due to the improved temperature resolution possible because one measures a spatially resolved signal.
2. With our new technique, we probe the order of the phase transition in the cyanobiphenyl liquid crystal 8CB and in mixtures of 8CB and 10CB.
3. We modify the HLM theory by studying the effect of an external magnetic (or electric) field on the order of the NA transition. The external field is expected to suppress the director fluctuations and to drive the first-order transition back to second order.
4. We study experimentally the effect of magnetic field on the order of the NA transition, both in 8CB—10CB mixtures and in pure 8CB.

The thesis is arranged as follows:

- In Chapter 2, I review the theoretical and experimental status of the NA transition.
- Chapter 3 contains an extension of the Halperin-Lubensky-Ma theory to a Hamiltonian containing a coupling between director fluctuations and an external magnetic (or electric) field.
- In Chapter 4, I describe the experimental techniques and methods designed to study this transition.
- Chapter 5 is a description of the experimental calibrations, and experimental results, without and with a field, in 8CB, and in a mixture of 8CB and 10CB.
- Chapter 6 contains the analysis of field effects and studies in mixtures.

- In Chapter 7, I summarise my results and suggest directions for future work.

## Chapter 2

# A REVIEW OF THE NA TRANSITION

*A theoretical and experimental review of the current state of knowledge of the NA transition.*

### 2.1 THEORY

#### 2.1.1 Introduction

A review of the entire subject of the NA transition would restate what can be found in a number of books and reviews (see for example references [2, 3, 4, 17, 10, 20, 21, 22, 23]). This chapter is written with emphasis on two broad themes: the weak anisotropy of the NA transition and the question of phase transition order.

#### **First-principles Theory**

An exact statistical mechanical theory of the NA transition is forbiddingly difficult because of the need to calculate higher-order fluctuation effects. Calculations based on the Onsager model [24] have only been done to the lowest-order terms in the virial expansion and are therefore correct only for a system of very long rods with hard-core interactions. The impetus for the renewed interest in the last decade in rigid-rod systems with hard-core interactions has come from computer simulations [25]. Density-functional theory has been employed as well [26, 27], and efforts are under way to extend the study to rigid rods of aspect ratio less

than 10. The current experimental systems closest to rigid rods are virus particles, which have aspect ratios ranging from 20 to greater than 100. Recent experiments using solutions of virus particles [5, 28] show that the angular correlations in the nematic phase of these athermal lyotropics is consistent with predictions based on the Onsager theory. The NA transition in these athermal systems is also currently under study [29]. The existence of these experimental systems provides a fertile testing ground for computer-inspired models that explore two extensions to the large-aspect-ratio rigid-rod models: the effect on the phase behaviour and the phase transition order of the flexibility of the molecules and of smaller aspect ratios, ranging from 1 to 50.

### **Phenomenology of the NA Transition**

Most thermotropic liquid crystals exhibiting a nematic and a smectic-A phase can be crudely described as having a short rigid part (often getting their rigidity from phenyl groups) and a flexible alkyl chain. In addition, attractive interactions between molecules are important, and the phase behaviour reflects an interplay between energetic and entropic effects. The NA transition in these materials has been observed to be either continuous or very weakly first order.<sup>1</sup> Pretransitional effects in the nematic phase are strong.

Mean-field theory has been applied to the NA transition by Kobayashi [30] and McMillan [31]. This captures the qualitative phase behaviour and provides the foundation for the theoretical understanding of the subject. Close to the transition, one can write down the Landau free energy as a gradient expansion in  $\psi$ . With the Landau free energy as the starting point, one can allow fluctuations of the smectic and nematic order parameters, leading to the Landau-de Gennes free energy. The solution of the Landau-de Gennes free energy in its entirety still eludes us, although attempts have been made using different approximations. No one theory explains all the observed phenomena, but the shortcomings provide us with clues as to the nature of the transition.

---

<sup>1</sup>Observing a continuous transition is essentially a null measurement: the latent heat is either non-existent or smaller than the resolution of the instrument.

### 2.1.2 The Landau Free Energy

#### General Ideas

There are general principles that put constraints on the structure of the Landau free energy  $F$  (see Ref. [12], p.140):

1.  $F$  has to be consistent with the symmetries of the system.
2. In the disordered phase, the order parameter is zero, while it is non-zero in the ordered phase.
3. Near the transition,  $F$  can be expanded in a power series in the order parameter  $\psi$ .
4. With a spatially varying order parameter  $\psi(\mathbf{r})$ ,  $F$  is a local function, as it depends only on  $\psi(\mathbf{r})$  and its derivatives.
5. Symmetry constraints further restrict the structure of  $F$ . For example, when the system has  $\psi \rightarrow -\psi$  symmetry,  $F$  should be invariant with respect to the sign of  $\psi$ . Such a symmetry would restrict the free energy only to terms even in  $\psi$ .

#### The Landau free energy applied to the NA transition

The existence of pre-transitional effects suggests that one can expand the free energy in the nematic phase close to the NA transition in powers of the smectic order parameter  $\psi$ , defined in Chapter 1.

The free energy should be invariant to arbitrary translations along the direction of the layer normal. Choosing the  $\hat{z}$  coordinate along the layer normal, an arbitrary translation  $a$  results in a change of phase in  $\psi$ :

$$z \rightarrow z + a \implies \psi \rightarrow \psi e^{iq_0 a}. \quad (2.1)$$

In the previous section, we implicitly assumed a real order parameter. For a complex order parameter, this discussion can be generalised. The choice of a complex order parameter for the smectic phase is motivated by the existence of the translational invariance in the the choice of origin for the layering. This translational invariance along  $\hat{z}$  can naturally be

taken into account requiring each term in the free energy power series to be a product of equal numbers of  $\psi$  and  $\psi^*$  terms; i.e.,  $F = F(|\psi|^2)$ :

$$f(r) = \frac{1}{2} A |\psi|^2 + \frac{1}{4} C' |\psi|^4 + \frac{1}{6} E |\psi|^6. \quad (2.2)$$

In the mean-field approximation, the phase transition is driven by a change in the sign of the lowest order ( $|\psi|^2$ ) term:  $A = \alpha \cdot t$ , where  $t = (T - T_{NA})/T_{NA}$  is the reduced temperature.

If  $C' > 0$ , then the high temperature (nematic) phase has only one (local and global) minimum. In the low-temperature (smectic-A) phase, this minimum becomes a local maximum, and the minima shift symmetrically to non-zero  $\psi$ . The transition is second-order: there is no metastability or hysteresis, and the disordered phase becomes absolutely unstable at the transition point (see Fig. 2.1).

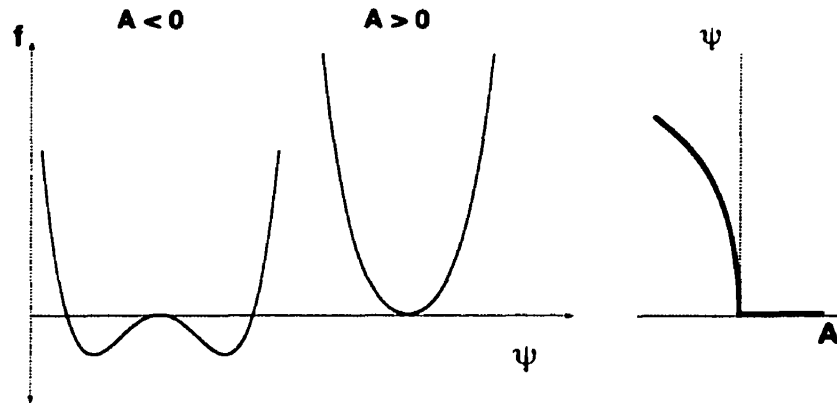


Figure 2.1: When  $C' > 0$  the phase transition at  $A = 0$  is continuous (second order) with no metastable behaviour.

For  $C' < 0$ , the high-temperature phase has a local minimum at  $\psi = 0$ . Above  $A = A_c$ , this is also the global minimum. In this case, the nematic phase is stable. Below  $A = A_c$ , the nematic phase becomes metastable. Not until  $A = 0$  does the nematic phase become absolutely unstable (this point,  $A^*$  is the nematic spinodal point). There is, correspondingly, a smectic spinodal point  $A = A^{**} > A_c$ , which is the point above which the smectic phase becomes absolutely unstable. Such a transition is first-order or discontinuous (see Fig. 2.2). The region between  $A^{**}$  (above which the smectic phase is absolutely unstable) and  $A^*$  (below which the nematic phase is absolutely unstable) is the *region of metastability*.

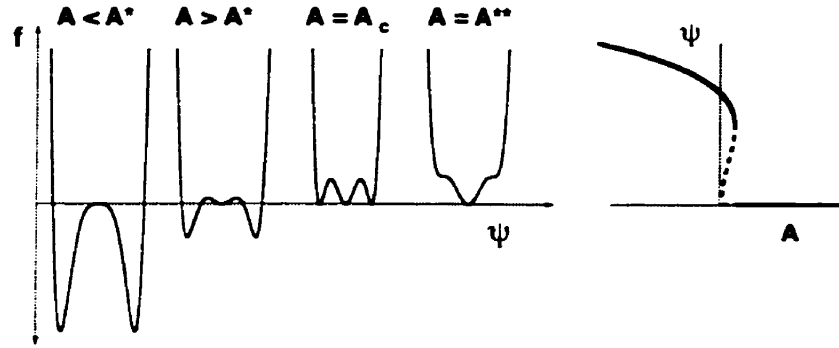


Figure 2.2: When  $C' < 0$  the phase transition is discontinuous (first-order), and has a metastable region between  $A^* = 0$  (the nematic spinodal point) and  $A^{**}$  (the smectic spinodal point). The phase transition is at  $A_c$ .

The tricritical point is at  $C' = 0$ . It is the point in parameter-space where the second-order line ends, and the transition becomes first order. Thus, the sign of the fourth-order term mediates a change from a second- to a first-order phase transition. What do theories of the NA transition tell us about the sign of  $C'$ ? The Kobayashi-McMillan theory, discussed in the next section, suggests that the sign of  $C'$  is positive and that the transition is second order, except when  $T_{NA}$  is very close to  $T_{IN}$ . But this calculation is mean field, and fluctuations can change the situation. This is discussed in the following sections.

### 2.1.3 Kobayashi-McMillan theory

Kobayashi [30] and McMillan [31] independently proposed a simple, phenomenologically motivated extension to the Maier-Saupe theory [32, 33] of the isotropic-nematic (IN) transition, including an additional order parameter for the smectic phase. Their modification was to introduce a term that reflects the short-range interaction between the molecules. One can write a single-particle potential as follows:

$$V_1(z, \cos(\theta)) = -V_0 \cdot [S + \bar{\psi}\alpha' \cos(2\pi z/d)] \cdot (3 \cos^2 \theta - 1)/2, \quad (2.3)$$

where  $\alpha' = 2 \cdot e^{-(\pi r_0/d)^2}$ .

This form ensures that the energy is a minimum when the molecule is in the smectic layer and a maximum half-way in between the layers. Note that this puts the layering into

the physics by hand; however, it is a self-consistent theory that at least provides a clear foundation for developing an experimental intuition for the transition. The single-particle distribution function is then

$$f_1(z, \cos \theta) = e^{-V_1(z, \cos \theta)/k_B T}, \quad (2.4)$$

and self-consistency demands that

$$\begin{aligned} S &= \left\langle \frac{(3 \cos^2 \theta - 1)}{2} \right\rangle \\ \bar{\psi} &= \left\langle \cos(2\pi z/d) \cdot \frac{(3 \cos^2 \theta - 1)}{2} \right\rangle, \end{aligned} \quad (2.5)$$

where the angular brackets are an average over the distribution function  $f_1$ . The order parameter  $\bar{\psi}$  gives the smectic density modulation associated with smectic layering, while  $S$  is the nematic order parameter magnitude. The last two equations can be solved to give the different regimes of behaviour:

$$\begin{aligned} \bar{\psi} &= 0, S = 0 \quad (\text{isotropic phase}), \\ \bar{\psi} &= 0, S \neq 0 \quad (\text{nematic phase}), \\ \bar{\psi} &\neq 0, S \neq 0 \quad (\text{smectic phase}). \end{aligned} \quad (2.6)$$

Moreover, this theory also predicts that the order of the transition depends on the ratio  $T_{NA}/T_{IN}$ :

1. second-order phase transition for  $T_{NA}/T_{IN} < 0.87$ .
2. first-order phase transition for  $T_{NA}/T_{IN} > 0.87$ .
3. the point  $T_{NA}/T_{IN} = 0.87$ , where the second-order line becomes a first-order one, is the mean field “tricritical point.”

#### 2.1.4 Mean-Field Theory vs. Landau theory

In order to go beyond mean-field theory, one needs to take into account the spatially non-uniform fluctuations of the system, and calculate the free-energy density as a function of the order parameter, its spatial derivatives, and temperature.<sup>2</sup> A rigorous determination

<sup>2</sup>The dependence on pressure is neglected in this discussion.

of the free-energy-density function is extremely difficult. However, close to a second-order (or weakly first-order) phase transition, this free-energy density function can be expanded as a power series in the order parameter and its derivatives, with temperature-dependent coefficients. Landau theory is simpler mathematically than mean-field theory and provides semi-quantitative information about quantities such as the specific heat, the latent heat, and the order parameter. Simplicity and the inclusion of spatial derivatives are its main advantages over mean-field theory. However, it is useful only close to the transition point, and it contains more phenomenological parameters than mean-field theory.

The following sections are devoted to a study of Landau theory as applied to the NA phase transition—the Landau-de Gennes model [2].<sup>3</sup>

### 2.1.5 A Return to Landau Theory

#### The Landau-de Gennes Model

In a previous section, we introduced the Landau free-energy density, neglecting the gradient terms (Eq. 2.2). Adding gradient terms to this function allows one to take into account spatial inhomogeneities.

$$f_{Sm}(r) = \frac{1}{2} A |\psi|^2 + \frac{1}{4} C' |\psi|^4 + \frac{1}{6} E |\psi|^6 + f_{grad}, \quad (2.7)$$

where

$$f_{grad} = \frac{1}{2} C_{\parallel} \cdot |\nabla_{\parallel} \psi|^2 + \frac{1}{2} C_{\perp} \cdot |\nabla_{\perp} \psi|^2. \quad (2.8)$$

In Fourier space, neglecting  $|\psi|^4$  and higher-order terms.

$$f_{Sm}(\mathbf{q}) = \langle |\psi|^2 \rangle \left[ \frac{1}{2} A + C_{\parallel} (q_{\parallel} - q_0)^2 + C_{\perp} q_{\perp}^2 \right] \quad (2.9)$$

Using the equipartition theorem and assigning each mode an energy  $\frac{1}{2} k_B T$ , we find that the structure factor for the smectic fluctuations is

$$\begin{aligned} S(\mathbf{q}) &= \frac{k_B T}{\frac{1}{2} A + C_{\parallel} (q_{\parallel} - q_0)^2 + C_{\perp} q_{\perp}^2} \\ &= \frac{\sigma}{1 + \xi_{\parallel}^2 (q_{\parallel} - q_0)^2 + \xi_{\perp}^2 q_{\perp}^2}, \end{aligned} \quad (2.10)$$

<sup>3</sup>For a detailed exposition of Landau-de Gennes theory, see Ref.[34].

Exponent	Mean Field	3DXY	Tricritical
$\alpha$	0	-0.007	0.5
$\gamma$	1	1.316	1
$\nu_{\parallel} = \nu_{\perp}$	0.5	0.669	0.5

Table 2.1: Critical exponents for the 3DXY model, mean field theory and the tricritical point (from Ref. [10]).

where  $\sigma$  is the smectic susceptibility, and  $\xi_{\parallel}$  and  $\xi_{\perp}$  are correlation lengths parallel and perpendicular to the nematic director, respectively. The exponents,  $\gamma$ ,  $\nu_{\parallel}$ , and  $\nu_{\perp}$ , describe the divergence of  $\sigma$ ,  $\xi_{\parallel}$  and  $\xi_{\perp}$ , respectively, as a function of the reduced temperature  $t$ :

$$\begin{aligned}
 \sigma &= 2k_B T/A \simeq t^{-\gamma} \\
 \xi_{\parallel} &= (2C_{\parallel}/A)^{1/2} \simeq t^{-\nu_{\parallel}} \\
 \xi_{\perp} &= (2C_{\perp}/A)^{1/2} \simeq t^{-\nu_{\perp}}.
 \end{aligned} \tag{2.11}$$

### Critical Exponents

One can derive theoretical values for the critical exponents  $\gamma$ ,  $\nu_{\parallel}$ ,  $\nu_{\perp}$ , and the specific heat exponent  $\alpha$  in the mean-field approximation, via renormalization-group calculations based on the de Gennes model, and also for the tricritical model. These allow direct comparison between theory and experiment (see Table 2.1). In the mean-field case, one can read off the exponents trivially from Eq. 2.11, since all the temperature dependence is in the coefficient  $A \equiv \bar{\alpha}t$ .<sup>4</sup> The renormalization group captures features close to the phase transition that depend only on the dimensionality of the order parameter and that of the bulk medium — so that the two-component smectic order parameter falls into the 3DXY universality class. Close to the tricritical point, the specific heat exponent goes from the second-order 3DXY value of  $-0.007$  (experimentally indistinguishable from zero) to the tricritical value of  $0.5$ .

These exponents form the basis for comparison between theory and experiment. This analysis, however, presupposes that the transition is indeed second-order ( $C' > 0$ ). For a first-order transition, if the discontinuity is weak, the power-law behaviour can still be observed; however in this case, the divergence towards the spinodal point  $T^*$  is cut off abruptly

<sup>4</sup>Note that the symbol  $\alpha$  is used both for the specific-heat exponent and the quadratic term of the Landau free energy. Where necessary to avoid confusion, the latter will be denoted  $\bar{\alpha}$ .

at  $T_{NA}$ . The spinodal point is then merely a phantom divergence, and the thermodynamic quantities remain finite at the transition. Next, we discuss how fluctuations of the *nematic* order parameter can change not only the value of the critical exponents but, more strikingly, even the order of the phase transition.

### 2.1.6 Coupling of the Nematic and Smectic-A Order Parameters — The Effect of Fluctuations.

#### The $\delta S - \psi$ coupling

The isotropic-nematic (IN) transition in thermotropics is a weakly first-order transition. The strength of “first-order-ness” can be characterised by a number  $t^* = (T_{IN} - T^*)/T^*$ , where  $T_{IN}$  is the IN transition temperature and  $T^*$  is the spinodal temperature for the high-temperature (isotropic) phase.<sup>5</sup> For a second-order transition, there is no metastable phase, and  $t^* = 0$ . For a first-order transition,  $t^*$  is a positive number. For a strong first-order transition such as liquid-solid, this number is large (of order 1). For the IN transition in most thermotropics, it is of order  $10^{-3}$ .

The nematic order parameter magnitude

$$S = \left\langle \frac{3 \cos^2 \theta - 1}{2} \right\rangle = 0 \quad (2.12)$$

in the isotropic phase. However  $0 < S < 1$  in the nematic phase, and, in principle, only goes to 1 (i.e., the molecules become perfectly orientationally ordered) when the temperature  $T \rightarrow 0$ ; in real materials, other phases intervene. For temperatures just below the IN transition, the order parameter magnitude  $S$  increases rapidly and saturates only well into the nematic phase (see Fig. 2.3). In a typical liquid crystal that exhibits both nematic and smectic-A phases,  $S$  might go from  $S \approx 0.3$  at the IN transition to  $S \approx 0.6 - 0.7$  at the NA transition. Since the NA transition is often close in temperature to the IN transition, the value of  $S$  may be strongly temperature-dependent at the NA transition. Thermally driven  $\delta S$  fluctuations are therefore important at the NA transition. There is a sharp increase in  $S$  at the NA transition, because orientational (twist and bend) fluctuations are suppressed in

---

<sup>5</sup>One could equally well define the dimensionless temperature to be  $(T^* - T^{**})/T^{**}$ , where  $T^{**}$  is the spinodal point for the low-temperature (nematic) phase, but  $T_{IN}$  is easier to measure than  $T^{**}$ .

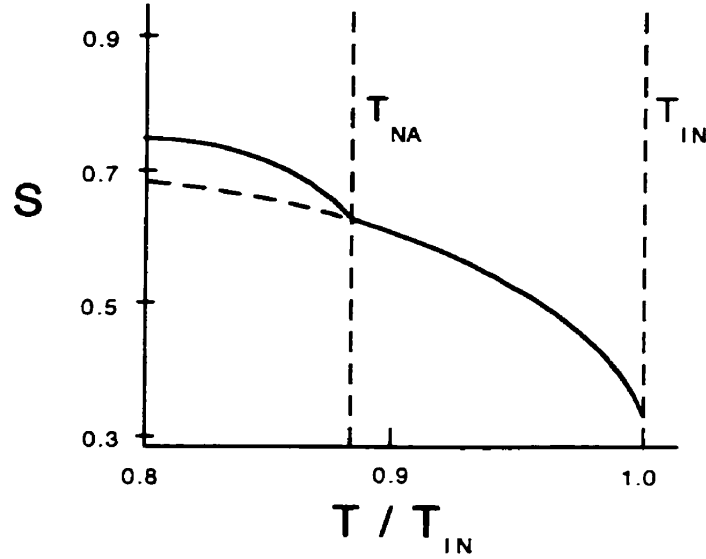


Figure 2.3: The nematic order parameter increases, from a small non-zero value near  $T_{IN}$ , to a larger value deep in the nematic. There is typically a sharp increase in  $S$  at the NA transition. If the NA transition is weakly first order then there would be a small jump at  $T_{NA}$ .

the smectic phase. The incomplete orientational ordering in the nematic phase intrinsically couples the nematic order parameter with the emergence of smectic ordering.

This implies that the advent of the smectic phase, i.e., an increase in the smectic order parameter  $\psi$ , is coupled with an increase in the nematic order parameter magnitude,  $S$ . Since the temperature dependence of  $S$  close to  $T_{IN}$  is strong, thermal fluctuations give rise to appreciable fluctuations in  $S$

$$\delta S \equiv S - S_0, \quad (2.13)$$

$S_0$  being the value of  $S$  given by setting  $f'_N(S) = 0$ , i.e., excluding any smectic coupling.<sup>6</sup> As we saw earlier, the  $|\psi|^2$  term is the lowest-order allowed term in  $\psi$ . Odd powers of  $S$

<sup>6</sup>Here,  $f_N(S)$  is the dependence of the nematic free energy on the order parameter magnitude,  $S$ , and the prime refers to a derivative with respect to  $S$ . It is not important in this analysis to write down the actual  $S$  dependence.

are not forbidden, however.<sup>7</sup> Therefore, to lowest order the  $\delta S - \psi$  coupling is

$$f_1 = -k |\psi|^2 \delta S. \quad (2.14)$$

Having introduced this coupling, we must also include in  $f$  (Eq. 2.2) the nematic free-energy density  $f_N$  (Eq. 1.3), which is a minimum for  $S = S_0$ . Since  $f'_N(S)|_{S=S_0} = 0$ , the lowest-order, non-zero fluctuation is  $O(\delta S^2)$ :

$$f_N = f_N(S_0) + \frac{1}{2\chi} \delta S^2, \quad (2.15)$$

where  $\chi(T)$  is a response function that is large close to  $T_{IN}$ , but small far away.

Adding Eq. 2.14 and Eq. 2.15 and minimising with respect to  $\delta S$ , one gets

$$\delta S_{min} = k \chi |\psi|^2. \quad (2.16)$$

One can get an effective free-energy density that depends only on  $\psi$  by replacing  $\delta S$  with  $\delta S_{min}$ . The structure of the free-energy density does not change in this process:

$$f(r) = \frac{1}{2} A |\psi|^2 + \frac{1}{4} C |\psi|^4 + \frac{1}{6} E |\psi|^6, \quad (2.17)$$

where  $C = C' - 2k^2\chi$ . The coefficient  $C$  is now renormalized so that even when the bare value  $C'$  is positive, the fourth-order term can still be negative when  $\chi$  is large enough (or equivalently, as seen earlier in the Kobayashi-Macmillan theory, when  $T_{NA}$  is close enough to  $T_{IN}$ ). Thus, the transition is driven first order when this coupling is strong enough. The point  $C = 0$  is termed the Landau tricritical point (“LTP”). The fluctuations of the nematic order parameter magnitude,  $S$ , are especially large near the IN transition. The above coupling-induced renormalisation of the quartic coefficient is thus expected get stronger as  $T_{NA}/T_{IN} \rightarrow 1$ , i.e. on approaching the I—N—A triple point.

### The $\delta \hat{n} - \psi$ coupling

Since  $S$  is not equal to 1 in the nematic phase, it indicates imperfect orientational ordering: the molecules fluctuate thermally about their average orientation. The average direction

---

<sup>7</sup>Changing the sign of the nematic order parameter magnitude  $S = \langle (3 \cos^2 \theta - 1)/2 \rangle$  results in different physical orientations: for example,  $S = -\frac{1}{2}$  and  $S = +\frac{1}{2}$  correspond to different average orientations with  $\langle \cos^2 \theta \rangle = \frac{1}{6}$  and  $\langle \cos^2 \theta \rangle = \frac{1}{2}$ , respectively. With no  $S \rightarrow -S$  symmetry, terms linear in  $S$  are allowed.

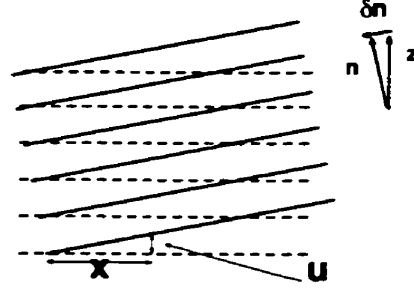


Figure 2.4: Rotation of the layers  $\delta n_x$  corresponds to a layer displacement  $u = -\delta n_x$ .

is denoted by the (headless) vector  $\hat{n}$ ; fluctuations in this average direction give rise to a subtle coupling. The gradient terms in the free-energy density expansion are anisotropic. They are taken parallel and perpendicular to the director. Defining the  $\hat{z}$  coordinate to be along the average director, we write the director fluctuations as

$$\delta \hat{n} \equiv \hat{n} - \hat{z}. \quad (2.18)$$

To linear order,  $\delta \hat{n} = \delta \hat{n}_\perp$ . In the sketch shown in Fig. 2.4,  $\delta \hat{n}_\perp$  is in the  $x$ - $y$  plane. A small rotation of the layers  $\delta \hat{n}_x$  corresponds to a layer displacement  $u = -\delta \hat{n}_x x$ , which should not change the free energy of the system. This corresponds to a phase shift in  $\psi$ :

$$\psi = \psi_i e^{+iq_s \delta \hat{n}_x}, \quad (2.19)$$

where  $\psi_i$  is the order parameter defined in the local reference frame. Therefore,

$$\nabla_\perp \psi_i = (\nabla_\perp - iq_s \delta \hat{n}_\perp) \psi \quad (2.20)$$

and  $\nabla_\parallel$  is unchanged to lowest order. The gradient terms of Eq. 2.8 are thus modified:

$$f_{grad} = C_\parallel |\nabla_\parallel \psi|^2 + C_\perp |(\nabla_\perp - iq_s \delta \hat{n}_\perp) \psi|^2 \quad (2.21)$$

Having included the nematic director explicitly, one has to introduce the nematic (Frank) free-energy density (Eq. 1.3 and restated here), as the NA free-energy density is now a function of both  $\psi$  and  $\hat{n}$ .

$$f_N = \frac{1}{2} K_1 (\nabla \cdot \hat{n})^2 + \frac{1}{2} K_2 (\hat{n} \cdot \nabla \times \hat{n})^2 + \frac{1}{2} K_3 (\hat{n} \times (\nabla \times \hat{n}))^2. \quad (2.22)$$

Thus, we get the full Landau-de Gennes free-energy density for the NA transition:

$$f_{NA} = \frac{1}{2} A \psi^2 + \frac{1}{4} C \psi^4 + \frac{1}{6} E \psi^6 + f_{grad} + f_N \quad (2.23)$$

### 2.1.7 A Field-Induced Tricritical Point

We first consider, briefly, the effect of external magnetic (or electric) fields on the de Gennes-McMillan coupling, discussed in Section 2.1.6. Rosenblatt [35] considered the effect of a coupling between the field and the fluctuations of the nematic order parameter magnitude<sup>8</sup>  $\delta S$ ,

$$F_M = -KH^2\delta S. \quad (2.24)$$

This coupling penalises negative  $\delta S$  fluctuations. Following a minimisation procedure similar to that in Section 2.1.6, one finds modification of the quadratic and quartic coefficients in Eq. 2.17,

$$\bar{A} = A - kK\chi H^2, \quad (2.25)$$

and

$$\bar{C} = C - \frac{1}{2}k^2\chi. \quad (2.26)$$

The magnetic field increases the transition temperature directly through Eq. 2.25; moreover, it quenches microscopic fluctuations and reduces  $\chi$ , which affects transition order indirectly through Eq. 2.26. The fields required to observe this effect are rather large; experiments observing this effect are discussed in Section 2.2.9.

This treatment studies the effect of a field on the phase behaviour via its effect on the  $\delta S - \psi$  coupling; the subtler effect of a field on the  $\delta n - \psi$  coupling has not been explored in detail until now. Our studies of this effect are summarised in Chapter 3.

### 2.1.8 The analogy with superconductivity

The free-energy density function in Eq. 2.23 is complicated, and a useful heuristic for understanding it is the analogy with superconductivity. The Landau-Ginsburg free-energy density describing the normal-superconducting transition is

$$f_{SC} = \frac{1}{2} A\psi^2 + \frac{1}{4} C\psi^4 + \frac{1}{2m} \left| \left( \hbar \nabla - i\frac{q}{c} \mathbf{A} \right) \psi \right|^2 + \frac{1}{16\pi\mu} (\nabla \times \mathbf{A})^2, \quad (2.27)$$

where  $A$ , the quadratic coefficient, is distinct from  $\mathbf{A}$ . The formal analogy with superconductivity, as well as a definition of terms, is illustrated in Table 2.2 (see [2] for details).

---

<sup>8</sup>Note that the linear power of the magnetic field is excluded by symmetry in any local free energy. In Chapter 3, we will see a linear  $H$  dependence in an *effective* free energy derived by integrating out of director fluctuations.

Smectic-A	Superconductor
$\psi$ smectics (density wave) director fluctuation $\delta n_{\perp}$ $C_{\parallel,\perp}$ $q_0$ $K$ (Frank constants) Gradient energy Frank elastic energy	$\psi$ superconductors (Cooper pairs) magnetic vector potential $\mathbf{A}$ $m^{-1}$ where $m$ = mass of Cooper pairs $q/c$ charge of Cooper pairs divided by speed of light $1/\mu$ inverse magnetic permittivity Kinetic energy Magnetic energy
Two coherence lengths $\xi_{\parallel,\perp} = (C_{\parallel,\perp}/ A )^{1/2}$	Order-parameter coherence length $\xi = (1/ A m)^{1/2}$
Four penetration lengths $\lambda_{\parallel,\perp}^{2,3} = (K_{2,3}C/C_{\parallel,\perp} A )^{1/2}$	London penetration depth $\lambda = (Cm/4\pi\mu A )^{1/2}$
Landau-Peierls divergence of layer fluctuations	True long-range order in $\psi$
Additional splay length breaks gauge symmetry $\lambda_1 = (K_1/B)^{1/2}$	Gauge symmetry

Table 2.2: The correspondence between smectic-A phases and superconductors.

The regimes  $\lambda\sqrt{2} < \xi$  and  $\lambda\sqrt{2} > \xi$  in a superconductor correspond to type-1 and type-2 behaviour, respectively. The NA transition does, broadly speaking, display type-1 and type-2 behaviour as does a superconductor. In the smectic, the superconducting analogy would imply two classes of response to a bending or twisting stress. A “type-1” smectic would resist the applied stress until a critical stress induces a transition to the nematic phase. In the “type-2” smectic, the transition to a nematic at a critical stress would be preceded by another transition at a lower threshold value where dislocations would set in [36].<sup>9</sup>

There are, however, important differences as well, which, in principle, restrict the usefulness of the analogy. First, there are two coherence lengths (not one) and five penetration lengths (not one), arising from the anisotropic gradient terms and the three elastic constants in the nematic. In principle, there is a regime where some penetration lengths are larger and some smaller than the coherence lengths. This regime would then be neither strictly type 1 nor type 2. The extent and importance of this regime in *real* liquid crystals has not been conclusively established.

Also, the Landau-Peierls divergence of the mean-square fluctuations in the layer spacing (Section 1.4.2) implies that the smectic does not have long-range order, while the superconductor, in contrast, has true long-range order.

Finally, the superconducting free energy is gauge invariant. The Landau-de Gennes free energy is not gauge invariant; indeed, only one gauge has physical meaning, namely the “liquid-crystal” gauge, where  $\delta n_z = 0$ .

### The framework for existing theories

Experimentally, one goes from type-1 to type-2 behaviour by widening the nematic range. In the extreme type-1 limit, fluctuations in the smectic order parameter can be neglected. In particular, this approximation is valid at the Landau tricritical point (LTP), defined in Section 2.1.6. For wider nematic range, the transition is weakly type 1. In the extreme type-

---

<sup>9</sup>A beautiful example of this analogy is the twisted-grain boundary (TGB) phase, which is the analogue of the Abrikosov vortex lattice in superconductors. In a chiral nematic, the twisting structure is not compatible with the layering in the smectic. Twist then plays the role of the magnetic field in the superconductor. If the smectic is type-2, instead of completely expelling the twist from the bulk, it allows instead a regular lattice of grain boundaries. The smectic slabs on either side of a grain boundary are twisted with respect to each other. See Ref. [37] for a good, current review.

2 limit, on the other hand, one can neglect fluctuations in the magnitude of  $\psi$  and consider only the phase fluctuations. In the intermediate region, in principle both the nematic and the smectic order parameters are active. Not much is known theoretically about this region of the NA phase diagram (see below).

The superconductor analogy is useful in shaping intuitions about the different classes of theories to study the NA transition:

1. In the extreme type-1 limit, the homogeneous nematic-smectic-A coupling mechanisms (de Gennes-McMillan and HLM) drive the transition first order. While the deGennes-McMillan mechanism has been well-explored, there are still open questions about the HLM mechanism.
2. In the extreme type-2 limit, the basic question is whether the 3DXY model, which is isotropic (i.e.,  $\nu_{\parallel} = \nu_{\perp}$ ) is exact, or whether there is an intrinsic anisotropy even in the extreme type-2 limit. Experiments [38, 39] have shown that as  $T_{NA}/T_{IN}$  is reduced (by choosing liquid crystals with wider nematic range), the ratio  $\nu_{\parallel}/\nu_{\perp}$  comes closer to 1. (See also the review article by Garland and Nounesis [17] and Fig. 2.5 and Fig. 1.5.) But even for the widest nematic ranges, a weak anisotropy persists.<sup>10</sup> Two very different approaches in the type-2 limit are the dislocation-mediated mechanism [40] and the theory of Dasgupta and Halperin [41], which predicts *inverted* 3DXY exponents. (The inverted 3DXY transition has critical exponents that are the same as the normal (non-inverted) 3DXY exponents; it is the temperature scale that is inverted. Thus, the shape of the specific heat curve in the inverted 3DXY universality class, for example, would be the mirror image of that in the non-inverted case.)
3. The crossover from type-1 to type-2 has been addressed by the theory of Patton and Andereck [42, 43, 20]. Although a qualitative comparison between their predictions and experimental observations has been made in Ref. [17], no quantitative comparisons have been made, primarily because of the extremely fine experimental resolution required.

---

<sup>10</sup>In the case of X-ray measurements, the interpretation of the measured exponents is gauge-dependent. The anisotropy of exponents in the physical liquid-crystal gauge is not inconsistent with isotropic 3DXY exponents (in the superconductor gauge), since the theoretical exponents are valid in the superconductor gauge (where  $\nabla \cdot (\delta \hat{n})$  is zero).

4. The weak type-1 limit has been addressed only by Monte Carlo simulation [44].

### 2.1.9 The HLM Effect

One simplification of the coupled two-order-parameter superconducting free energy was considered by Halperin, Lubensky and Ma (“HLM”) [14]. Applied to the NA transition,<sup>11</sup> the HLM theory assumes a “type-1 smectic” and neglects  $\psi$  fluctuations. Experimentally, this assumption should be valid for smectics with small nematic range, where the de Gennes-McMillan first-order mechanism is still active. This assumption allows one to integrate out the nematic degrees of freedom and derive an effective free-energy density that depends only on the smectic order parameter  $\psi$ . The effective free-energy density thus derived has a cubic term that is small and negative. Its negativity implies that the transition (if the calculation is valid) should always be first order; the weakness of the cubic term implies that this effect only becomes noticeable close to the Landau tricritical point (LTP). Experimentally, the latent heat *does not* go to zero at the LTP [46, 15, 16], and thus effects due to nematic director fluctuations are clearly important. Moreover, this cubic term has a non-analytic signature; we will see in Chapter 3, for example, that this leads to a non-analytic dependence of the zero-field discontinuity,  $t_0$ , on the external magnetic field. The HLM theory is so far the only theory that addresses this interesting region close to the LTP. Since this region is also the focus of this experimental study, the HLM theory and modifications made to it as part of this thesis will be discussed in detail in Chapter 3.

### 2.1.10 Monte Carlo Simulations of the de Gennes Model

In the type-2 limit, Dasgupta and Halperin [41] presented analytic and numerical evidence showing that the normal-superconducting (and in analogy the NA) transition is continuous

---

<sup>11</sup>The calculation is based on an expansion in  $\epsilon = 4 - d$ , where  $d$  is the spatial dimension, and the order parameter is an  $n$ -component generalisation of the two-component order parameter in the superconductor and smectic-A. For  $n > n_c = 367.9$ , they find the transition to be second order, and first order otherwise. For our study of the NA transition, the number  $n_c$  is a measure of how important smectic fluctuations are: the larger  $n_c$  is, the less important are smectic fluctuations at the physical  $n = 2$ . Restricting the director fluctuations to an easy plane, Halsey and Nelson [45] found that a similar calculation gave  $n_c = 110.8$ . This suggests that fluctuation effects should be stronger with planar director fluctuations—see Chapter 7.

and belongs to the “inverted” 3DXY universality class.<sup>12</sup>

In this analysis based on the superconducting analogy, the missing ingredient for the NA transition is the role of splay deformations. The effect of splay was explicitly examined in Monte Carlo simulations by Dasgupta [47], using as a Hamiltonian a discretised version of the de Gennes model. In this model, there are phase fluctuations but no fluctuations of the magnitude of the smectic order parameter; thus, the model is in the extreme “type-2” limit. The Monte Carlo simulation was done keeping the bare values of the twist and bend elastic constants  $K_2^0$  and  $K_3^0$  fixed, varying  $K_1^0$  for two non-zero values of the bare splay elastic constant ( $K_1^0 = 0.5$ , and  $K_1^0 = 5$ ). No sign of a first-order transition was found. Moreover, the ratio  $\frac{\xi_{\parallel}}{\xi_{\perp}}$ , calculated from correlation functions in the (unphysical) superconducting gauge, is constant. The temperature scale of the critical behaviour is *not inverted* for both values of splay. In contrast,  $K_1^0 = 0$  reduces via a gauge transformation to the lattice superconductor model and exhibits an inverted XY transition [41].

The final question concerns the crossover region between type 1 and type 2. This is, in fact, the appropriate region to look for a tricritical point. Allowing the superconducting order parameter magnitude to vary as well. Bartholomew [44] showed in a lattice simulation of the superconducting free energy that there was a crossover from a first-order transition to a second-order transition. No work has been done up to now in this region for the Landau-de Gennes free energy.

### 2.1.11 The “Laplace” Model: A Modification of the de Gennes Model

Another Monte Carlo study probing tricritical behaviour was done by Kleinert and Langhammer [48, 49]. They propose a *modification* to the Landau-de Gennes model, motivated by the problems *in principle* with the Landau-de Gennes model away from the type-2 region. In the vicinity of the I-N-A triple point, fluctuations of the nematic director become large. In their opinion, extension of the de Gennes model into this regime is “bound to fail

---

<sup>12</sup>In a type-2 superconductor, the transition from normal to superconducting is mediated by the appearance of magnetic vortex lines, which are screened from the normal phase by super-currents. The current loops are defined in the normal phase while the vortices are defined in the superconducting phase. Since the gauge fluctuations are massless, the current-loop interaction is long-range: the result is a 3DXY universality class with an inverted temperature scale. The topological defect in the smectic-A phase that corresponds to vortex loops in the superconductor is the dislocation loop.

precisely there, due to its built-in small director fluctuations” [49]. The authors consider a generalisation of the de Gennes model, which deep inside the nematic reduces to the original free energy. They propose an effective energy density

$$h(\mathbf{x}) \equiv A(T) |\psi(\mathbf{x})|^2 + \frac{B}{2} |\psi(\mathbf{x})|^4 + h_{sm}(\mathbf{x}), \quad (2.28)$$

with

$$h_{sm}(\mathbf{x}) = \frac{1}{2} |(\Delta + b^2)\psi(\mathbf{x})|^2. \quad (2.29)$$

This effective energy is invariant under global rotations and is called the “Laplace model”. The Laplace model is expected to be more general, being applicable not only to the second-order and tricritical region of the NA transition but to the smectic-isotropic transition as well. The results obtained from this model are as yet incomplete. The simulations are consistent with the existence of a tricritical point somewhere in the region  $0 \leq b^2 \leq \frac{3}{2}$ . For  $b^2 > \frac{3}{2}$ , the transition is first order, with the internal energy exhibiting hysteresis, while for  $b^2 < 0$ , the transition is second order. A renormalisation-group analysis of this model remains to be done, and the critical exponents implied by this model are not as yet known.

### 2.1.12 The Nelson-Toner (Dislocation-Unbinding) Model

A rather different theoretical approach was pursued by Nelson and Toner [40]. This method starts from the smectic-A side, with the continuum elastic free-energy density (Eq. 1.6). They then show that a smectic-A with a finite concentration of unbound dislocations behaves like a nematic, with Frank constants  $K_2$  and  $K_3$  that depend on the edge and screw dislocation energies, respectively. This behaviour occurs at wavelengths that are long compared to the distance between dislocation loops. The geometry of the dislocations then gives their dependence on correlation lengths

$$\begin{aligned} \delta K_2 &\propto \xi_{\perp}^2 / \xi_{\parallel} \\ \delta K_3 &\propto \xi_{\parallel}. \end{aligned} \quad (2.30)$$

Thereafter, a scaling argument based on the required density and spacing of the edge dislocations to decorrelate the translational order leads to a strongly anisotropic relation between the correlation lengths

$$\xi_{\perp}^2 \propto \xi_{\parallel}. \quad (2.31)$$

Toner [50] did a renormalisation-group analysis on this model; the resulting recursion relations yield finite values for the elastic constants  $B$  and  $K_1$  at the NA transition.

### 2.1.13 Anisotropic Scaling

The scaling form in Eq. 2.30 is more general than the dislocation-unbinding model; it is a consequence, too, of a more general anisotropic scaling hypothesis for the free energy, the two-point correlation function of the smectic order parameter, and the nematic director-director correlation function [51] (see Ref. [2], p. 517). The anisotropic scaling laws also predict a divergence of the layer compression modulus at  $T_{NA}$ , with a scaling form

$$B \propto \xi_{\parallel} / \xi_{\perp}^2. \quad (2.32)$$

The laws do not, however, predict a value for the correlation length exponents, since the scaling laws are not derived by solving the free energy, but by imposing scaling constraints on it, above and below  $T_{NA}$ .

Note that the splay constant  $K_1$  does not diverge at the transition. The above anisotropic scaling laws hold if one finds an anisotropic fixed point in a renormalisation-group calculation. Via an involved analysis (see Ref. [2], p. 521 for a summary) three possibilities emerge for the fixed point of the splay constant  $K_1^*$ :

1.  $K_1^* = 0$ . It is stable for  $\nu_{\parallel} < 2\nu_{\perp}$ , which reduces the problem exactly to the normal-superconducting transition, and implies that  $\nu_{\parallel} = \nu_{\perp}$ .
2.  $K_1^* = \infty$ . It is stable for  $\nu_{\parallel} > 2\nu_{\perp}$ .
3.  $K_1^*$  finite. In three dimensions, this requires  $\nu_{\parallel} = 2\nu_{\perp}$ .

The dislocation-unbinding transition, discussed in the previous section, satisfies the third possibility, while the prediction of isotropic (inverted) 3DXY behaviour satisfies the first condition. However, it is a crucial point that all three fixed points imply either a strong anisotropy ( $\nu_{\parallel} \geq 2\nu_{\perp}$ ), or no anisotropy at all ( $\nu_{\parallel} = \nu_{\perp}$ ). Experimentally, a weak anisotropy is observed: This suggests strongly that the renormalisation-group procedure outlined above does not describe the NA transition correctly. This leaves two other options:

1. The transition is first order.

2. All existing experiments at the NA transition are done in a crossover region.

The HLM mechanism, described briefly in Section 2.1.9, and in greater detail in Chapter 3, is one possibility, as it predicts that the transition is always weakly first order. Another possibility is the Andereck-Patton theory, discussed next.

### 2.1.14 Weak Anisotropy of the NA Transition

The relatively recent theory of Patton and Andereck [42, 43, 20] predicts a broad crossover from isotropic behaviour ( $\nu_{\perp} = \nu_{\parallel}$ ) to the anisotropic ( $\nu_{\perp} = \nu_{\parallel}/2$ ) behaviour. This theory is a self-consistent one-loop calculation that begins with the Landau-de Gennes free-energy density. In this picture, most experimentally observed liquid-crystal systems lie in the early phase of this crossover, and we simply never see the strong coupling region. However, quite interestingly, this crossover should also be seen in the nematic phase as a function of temperature. The Patton-Andereck theory would predict a crossover from high-temperature isotropic behaviour through a weakly anisotropic intermediate region, to a low-temperature, strongly anisotropic region. For typical values of the physical parameters, the intermediate weakly anisotropic regime spans six decades in reduced temperature! There is therefore some hope that this could be observed experimentally, but in order to do so conclusively, experiments with temperature resolution approaching  $10 - 100 \mu\text{K}$  might be necessary. The Patton-Andereck formalism could in principle be (but has not yet been) used to predict the order of the NA transition, as well.

### 2.1.15 Theoretical Summary

We have discussed several theories that attempt to explain different features of the NA transition. As we shall see in the next two sections in this chapter, no theory is able to completely describe all the observed phenomena at the NA transition. Mean-field theory was first described in Section 2.1.3, and then the Landau-de Gennes formalism upon which most other theories are based (Section 2.1.5). The Landau-de Gennes free-energy density was analysed using the superconducting analogy, which gave some intuitive expectations for the phase behaviour, and the notion of type-1 and type-2 smectics (Section 2.1.8). We then discussed several mutually-incompatible extensions to this formalism including the Nelson-Toner dislocation-mediated mechanism (Section 2.1.12), the anisotropic scaling

Symbolic Name	Chemical Structure
<b>NONPOLAR</b>	
$\bar{n}Sm$	$C_nH_{2n+1} - O - \phi - COS - \phi - C_mH_{2m+1}$
$\bar{n}O\bar{m}$	$C_nH_{2n+1} - O - \phi - COO - \phi - O - C_mH_{2m+1}$
$\bar{n}O \cdot \bar{m}$	$C_nH_{2n+1} - O - \phi - CH = N - \phi - C_mH_{2m+1}$
<b>POLAR</b>	
$nCB$	$C_nH_{2n+1} - \phi - \phi - CN$
$nOCB$	$C_nH_{2n+1} - O - \phi - \phi - CN$

Table 2.3: Symbolic names and chemical structures of a few smectic materials (after Ref.[17]). Phenyl groups are denoted by  $\phi$ ;  $n$  and  $m$  are integers.

theory (Section 2.1.13), the HLM theory (Section 2.1.9), and the Patton-Andereck theory (Section 2.1.14). Also discussed were Monte-Carlo simulations of the de Gennes model, and the implications of results from simulations in the superconducting gauge (Section 2.1.10). We also briefly described an extension to the Landau-de Gennes model (Section 2.1.11). In order to concretely compare these theories, we must first confront the experimental situation at the NA transition.

## 2.2 EXPERIMENT

### 2.2.1 Introduction

The NA transition has been studied by a wide variety of experimental techniques, and on a variety of liquid-crystalline materials. The first logical question is that of transition order. Since the transitions are either continuous or weakly first order, they are characterised by power-law divergences of various thermodynamic quantities as a function of the reduced temperature,  $t$ , on approaching the NA transition. Several experiments on numerous materials have contributed to the current understanding of the transition. The critical exponents,  $\alpha$ ,  $\gamma$ ,  $\nu_{\parallel}$ , and  $\nu_{\perp}$  obtained from a number of these experiments are compiled graphically in Figs. 2.5 and 1.5 (from Ref. [17]).

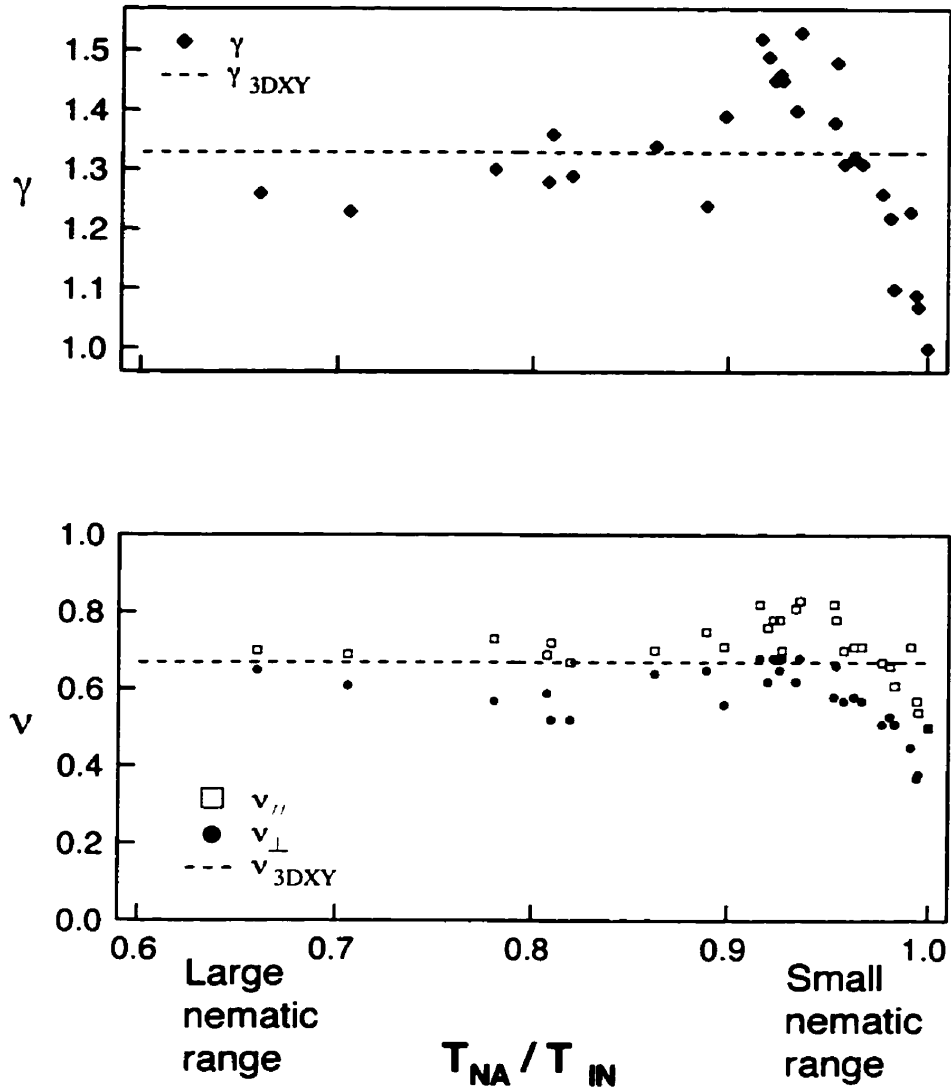


Figure 2.5: Smectic susceptibility and correlation-length exponents obtained by X-ray scattering on various different liquid-crystalline materials (from Ref. [17]).

### 2.2.2 Ways to probe tricritical behaviour

The crucial parameter in studies at the NA transition is the nematic range, denoted by the ratio  $T_{NA}/T_{IN}$ , where  $0 < T_{NA}/T_{IN} < 1$ . These transition temperatures are different for different materials, and experimental values for  $T_{NA}/T_{IN}$  range 0.6 to 1. The crucial issue is to vary this parameter without altering the chemical structure appreciably, as this will change interactions on the molecular level drastically.

Data on critical exponents as a function of  $T_{NA}/T_{IN}$  have been compiled from several distinct experiments on liquid crystals with different chemical structures. In varying  $T_{NA}$  and  $T_{IN}$ , one varies at the same time other properties, for example molecular anisotropy and the interaction of the material with surfaces. This temperature dependence on the material properties is large because it is impossible to get the broad range of transition temperatures that one needs in any other way. For  $T_{NA}/T_{IN} \simeq 1$ , the nematic range vanishes, while for  $T_{NA}/T_{IN} = 0.6$ , the nematic range is 180 °C! Thus, it is not surprising that the broad dependence of the critical exponents seen in Figs. 2.5 and 1.5 is rather noisy.

A cleaner way to study the dependence on  $T_{NA}/T_{IN}$  is to pick a series of liquid crystals that have very similar chemical structure. The typical liquid crystal molecule used in these studies has a rigid part made from a backbone of phenyl groups and a flexible alkyl chain. The length of the alkyl chain can be varied without changing the chemical interactions significantly. Increasing the length of the alkyl chain stabilises the smectic phase and therefore reduces the nematic range. This has been experimentally realised in two ways:

1. Vary  $T_{NA}/T_{IN}$  coarsely in a “homologous” series of increasing  $n$  (where every member of this series is identical but for the number  $n$  of alkyl groups in the chain).
2. *Mix* two members of a homologous series in different molar proportions to achieve a much finer variation of  $T_{NA}/T_{IN}$ .

These two methods are limited in the variation they can make to the nematic range—typically 10 °C, equivalent to a variation of  $T_{NA}/T_{IN}$  of less than 0.05. However, studies with homologous series of liquid crystals have been instrumental in elucidating the physics in the narrow region close to the I-N-A triple point [52, 53, 46] and are of use in searching for the tricritical point.

A third method, much more recent in its use, is the use of an external electric or magnetic

field [35, 54]. Via this method, one can directly quench fluctuations in the nematic phase; in contrast the first two methods achieve the quenching of fluctuations indirectly. This method also has the advantage of being cleaner, and an external field is an easier parameter to vary continuously.

### 2.2.3 X-ray structure factor measurements

In a smectic material, the electron density reflects the mass density, whose modulation is described by the smectic order parameter. X-rays scatter off electrons. The smectic structure factor has the calculated form [55]

$$\begin{aligned} S(q_{\parallel}, q_{\perp}=0) &\propto (q_{\parallel} - q_0)^{-2+\eta} \\ S(q_{\parallel} = q_0, q_{\perp}) &\propto q_{\perp}^{-4+2\eta} \\ \eta &= \frac{k_B T q_0^2}{8\pi\sqrt{BK}} \ll 1, \end{aligned} \quad (2.33)$$

that arises from the absence of true long range order (See also Section 1.4.2).

In X-ray scattering studies [56, 57, 38, 58], it is found necessary to fit the measured intensity to a structure factor of the form in Eq. 2.10 with an additional quartic term:<sup>13</sup>

$$S(\mathbf{q}) = \frac{\sigma}{1 + \xi_{\parallel}^2 (q_{\parallel}^2 - q_0^2) + \xi_{\perp}^2 q_{\perp}^2 + \xi_s^4 q_{\perp}^4}. \quad (2.34)$$

The physical significance of the quartic term is explained as a crossover from the  $q_{\perp}^{-2}$  behaviour in the nematic phase to the  $q_{\perp}^{-4+2\eta}$  behaviour in the smectic-A phase. X-ray measurements as a function of temperature can be used to determine the critical exponents  $\nu_{\parallel}$ ,  $\nu_{\perp}$  and  $\gamma$ .

It is observed in various independent experiments [17] (Fig. 2.5) that the exponent  $\nu_{\perp}$  is always smaller than  $\nu_{\parallel}$ . In the large nematic range limit, the correlation-length exponents are close to the 3DXY value, but the anisotropy remains. With progressively smaller nematic range, a crossover is seen from values close to 0.67 (the 3DXY value) to  $\nu \simeq 0.5$  (the tricritical value).

---

<sup>13</sup>Actual fitting involves convoluting the above with the instrumental resolution function and the mosaic spread that arises because of macroscopic variation in the nematic director orientation and hence the smectic planes over the region of illumination in the sample.

Note that in comparing X-ray exponents with 3DXY results, the latter must be transformed from the superconductor (SC) gauge, where they are valid, to the physical liquid crystal (LC) gauge. Thus, in this picture [59], even isotropic correlation lengths in the SC gauge, would become anisotropic in the LC gauge. Thus, Ref. [38] reports the following critical exponents in a large nematic range liquid crystal 8OPCBOB:

$$\begin{aligned}\gamma &= 1.40 \pm 0.06 \\ \nu_{\parallel} &= 0.71 \pm 0.03 \\ \nu_{\perp} &= 0.53 \pm 0.03.\end{aligned}\tag{2.35}$$

These correlation-length exponents are in fact anisotropic. However, they are, indeed, in agreement with the theoretical prediction in the LC gauge

$$\begin{aligned}\gamma &\leq 1.32 \\ \nu_{\parallel} &> \nu_{\perp}.\end{aligned}\tag{2.36}$$

while the smectic susceptibility exponent  $\gamma$  is only marginally outside the theoretically predicted range.

Another curious fact is that there is a marked increase in the smectic susceptibility exponent  $\gamma$ , from the 3DXY value of  $\approx 1.3$  to over 1.5 before going down to the tricritical value of 1.0. This behaviour is seen to some extent also in the correlation-length exponents, but not in the specific-heat exponent.

#### 2.2.4 Elastic constant measurements

##### The Frank elastic constants

Frank elastic constants have been measured by two techniques, light-scattering and Fréedericks transition measurements. Light scattering in the nematic phase is used to study the critical behaviour of the Frank elastic constants for twist,  $K_2$  and bend,  $K_3$ . The twist and bend divergences have the form

$$\begin{aligned}\delta K_2 &= t^{\rho_2} \\ \delta K_3 &= t^{\rho_3}\end{aligned}\tag{2.37}$$

Anisotropic scaling, discussed in Section 2.1.13, demands that

$$\begin{aligned}\rho_2 &= \nu_{\parallel} - 2\nu_{\perp} \\ \rho_3 &= -\nu_{\parallel}\end{aligned}\tag{2.38}$$

The exponents  $\nu_{\parallel}$  and  $\nu_{\perp}$  can thus be determined experimentally via elastic constant measurements. Since, theoretically,  $K_2$  and  $K_3$  are gauge independent, the experimental observations can directly be related to the correlation lengths in the superconducting gauge. This gauge-independence allows direct comparison to the theoretical predictions for different universality classes. For the isotropic 3DXY universality class,  $K_2$  and  $K_3$  should have the same divergence  $\rho_2 = \rho_3 = -\nu = -0.67$ . For the anisotropic class, one expects  $\rho_2 = 0$  and  $\rho_3 = \nu_{\parallel}$ . But once again, the exponents in all experiments show a weak anisotropy. The scatter in the values of the exponents is large enough that ambiguities persist on at least two points:

1. whether X-ray and light-scattering measurements actually give us information about different gauges or not.
2. whether correction-to-scaling terms are essential for analyzing the data or not.

The Fréedericks transition is an orientational instability in nematics that is driven by an external electric or magnetic field. It can be observed in planar-anchored nematics when a voltage is applied between the parallel glass plates that the nematic is sandwiched between. In the presence of a large-enough external field, the orientation changes continuously from parallel to perpendicular. The magnitude of the field required, known as the Fréedericks threshold, can be estimated from dimensional analysis. One compares the magnetic (or electric) field energy with the elastic energy (or alternatively sets  $\xi_H = \ell$ , where  $\xi_H$  is the magnetic coherence length defined in Section 1.4.1 and  $\ell$  the sample thickness). By varying the geometry, one can measure the twist, bend and splay elastic constants.

Gooden *et al.* [60] and Mahmood *et al.* [61] simultaneously measured  $K_2$  and  $K_3$  in three liquid crystals (8OCB, 8S5 and 6O9) by both light-scattering and Fréedericks transition methods, obtaining for the first time a consistent fit to all data using the same value of  $T^*$  as a fit parameter. In all cases, they found that the bend exponent  $\rho_3 = \nu_{\parallel} \simeq 2/3$ , giving the XY value for  $\rho_3 = \nu_{\parallel}$ . For the twist exponent it is expected that  $\rho_2 = 2\nu_{\perp} - \nu_{\parallel}$ ; the value obtained, however, is less than the XY value ( $\simeq 2/3$ ) and is non-universal.

Unlike the X-ray case,  $K_2$ ,  $K_3$ , and  $B$  are all gauge-independent quantities, and direct comparisons can be made with superconducting correlation lengths. Therefore, an anisotropy in the correlation-length exponents in this case is directly counter to 3DXY predictions.

### The layer compression modulus

The anisotropic scaling theory predicts that the layer-compression modulus should diverge at the NA transition, scaling as

$$B = t^\phi, \quad (2.39)$$

where, once again, anisotropic scaling requires that  $\phi = \nu_\perp - 2\nu_\parallel$ . On the smectic side, one can use light scattering and second-sound measurements to measure the critical behaviour of the layer compression constant  $B$ . The excitation of second-sound resonances has been studied by Benzekri *et al.* [62] by light-scattering in  $n$ CB and  $n$ OCB materials. They found that the elastic modulus  $B$  did not vanish at the NA transition but instead went to a non-zero value in the smectic phase. They explained this behaviour by the Landau-Peierls argument; i.e., that the smectic layer fluctuations should diverge logarithmically with the sample size  $L$  (see Eq.1.16). However, using the Lindemann melting criterion [63] implies that the smectic-A should melt to a nematic when the layer fluctuations exceed a small fraction (typically  $\sim 0.1$ ) of the layer spacing. The expression for  $\langle u^2(r) \rangle$  sets a lower limit on the compressional modulus  $B \simeq 10^6 - 10^7 \text{ dyn cm}^{-2}$ . The saturation is then not surprising. What is surprising, however, is the large value of reduced temperature  $t \equiv (T - T_c)/T_c$  at which it is observed, implying that the mechanism was *purely mean field*. This not only conflicts with observations of exponents in the nematic phase that differ from mean-field values (as seen earlier in this section), it also implies that any first-order jump cannot be fluctuation induced.

Recently, Martinoty *et al.* [64] have presented results from dynamic compression experiments that challenge this interpretation and show that the saturation effect observed by Benzekri *et al.* is a nonhydrodynamic effect. The true hydrodynamic ( $\omega \rightarrow 0$ ,  $q \rightarrow 0$ ) behaviour in the temperature range between a few mK and  $1^\circ\text{C}$  is in fact a pure power-law dependence. The Landau-Peierls argument is still valid, however, and looking for the non-vanishing of  $B$  at smaller  $t$  remains an interesting project (see Chapter 7).

### 2.2.5 Heat capacity measurements

Two high-resolution calorimetric methods have been used to study the specific heat and the latent heat at the NA transition.

Adiabatic calorimetry [65, 46, 53] has been used on relatively large liquid-crystal samples in order to measure with high resolution the change of enthalpy with temperature. In adiabatic calorimetry, the jacket surrounding the calorimeter is kept at the same temperature as the calorimeter, in order to minimise heat transfer to the surroundings. This method allows not only the tracking of the dependence of specific heat with temperature but also the measurement of any latent heat at the transition. In order to successfully measure the extremely small latent heats at the NA transition, one must use large samples (typically a few grams).

AC calorimetry is useful for small samples and looks at the temperature response to an oscillatory heat input. The precision of  $C_p$  values is very good (0.01% – 0.1%). But since it measures  $C_p$  rather than the enthalpy, it does not give a value for the latent heat  $\Delta H$ .<sup>14</sup>

As discussed before, one can vary, coarsely, the material parameter  $T_{NA}/T_{IN}$  simply by changing the liquid crystal, and, more finely, by varying the concentration in a binary mixture chosen from a homologous series. Fig. 1.5 shows the coarse dependence of  $\alpha$ . Below  $T_{NA}/T_{IN} = 0.93$ , the exponent  $\alpha$  is clearly consistent with the 3DXY value of  $-0.007$ . Most of the studies on homologous series have been done in the region where  $T_{NA}/T_{IN} \gtrsim 0.97$ .

Thoen, Marynissen, and Van Dael [65] used adiabatic calorimetry on 8CB and showed the transition to be second order. They also located the (“apparent”) tricritical point using alkycyanobiphenyl mixtures [46]. They used various concentrations of 9CB-10CB mixtures and 8CB-10CB mixtures. Extrapolating the functional dependence of the latent heat on mixture concentration, they deduced that the latent heat of pure 8CB to be less than 0.4 J/mol. For the 8CB-10CB mixture, they found the tricritical point to be at a 10CB concentration of 0.314 (mole-fraction). Far from the tricritical point, the latent heat decreased linearly with decreasing 10CB concentration on the first-order side. Close to the “apparent” tricritical point, there was a nonlinear deviation in this dependence. Anisimov *et al.* [15] showed that this behaviour was consistent with the existence of a negative cubic

---

<sup>14</sup>Garland *et al.* [66] have shown that however, reported a qualitative indicator of anomalous phase shifts in the oscillating sample temperature indicate, qualitatively, the two-phase coexistence characteristic of a first-order transition.

term in the free energy, which in turn had been predicted in 1974 by Halperin *et al.* [14]. A normalised universal form for the latent heat showing the crossover from linear to nonlinear dependence on mixture concentration, compiled from data on three different liquid-crystal mixtures, is shown in Fig. 2.6. The extrapolation of the linear part of the above dependence was identified as the Landau tricritical point (LTP) (discussed in Section 2.1.6, and defined theoretically as the point where the quartic coefficient,  $C$ , is zero), and can be understood in terms of the effect of  $(\delta S - \psi)$  coupling on the Landau free energy. The simplest candidate for the nonlinear “correction” is the effect of  $(\delta n - \psi)$  coupling on the free energy (see Chapter 3).

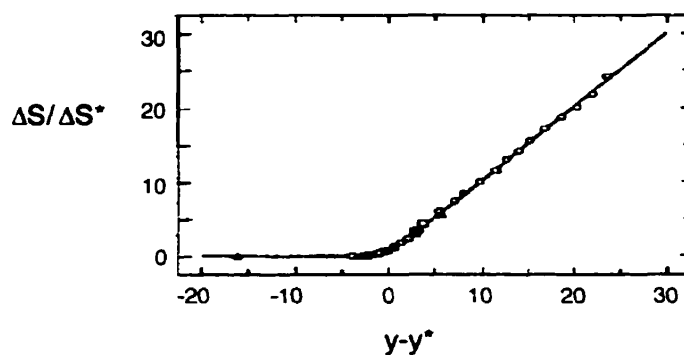


Figure 2.6: Normalised universal form for the latent heat, showing the crossover from linear to non-linear dependence on mixture concentration (after Ref.[15]). The data is compiled from experiments in 8CB-10CB, 9CB-10CB and  $\overline{6}O\overline{1}0$ - $\overline{6}O\overline{1}2$  mixtures.

Another way of determining the location of the tricritical point is by looking at the dependence of the the specific heat exponent, which should cross over to the tricritical value  $\alpha = 0.5$ . This crossover was first demonstrated by Brisbin *et al.* [67] in  $\overline{n}S5$  mixtures and later by Thoen *et al.* [53] in the  $nCB$  series. Stine *et al.* [68] used AC calorimetry and differential scanning calorimetry on 40·8 - 60·8 mixtures and found a similar dependence. Qualitatively, there was a broad crossover in all cases from 3DXY to tricritical behaviour, although there was no obvious universal form when the dependence of the exponents was plotted against the ratio  $T_{NA}/T_{IN}$ .

Note that in all cases where the exponents are consistent with 3DXY behaviour, the temperature-scale is not inverted, in contrast with the theoretical prediction of an inverted 3DXY universality class [41] but in agreement with numerical simulations [21].

### 2.2.6 Front velocity measurements

An indirect calorimetric method of measuring very small latent heats was devised by Cladis *et al.* [16]. Step temperature jumps of varying magnitudes are applied to a sample very close to the NA transition. The NA front moves across the field of view at varying speeds, depending on the magnitude of the jump. The form of this dependence allows a determination of the entropy change at the transition. Using this method, it was seen that the front velocity was linear in  $t$  ( $t$  is the reduced temperature, defined in Section 2.1.2). For second-order transitions, the front propagation speed should be proportional to  $t^{\frac{1}{2}}$ . It was suggested for the first time in this work that the phase transition in pure 8CB was in fact first order.

### 2.2.7 Capillary-length measurements

Another method, devised by Tamblyn *et al.* [69, 70], directly measures the capillary length  $d_0$  (the ratio of the surface tension to the latent heat per volume of an  $n$ CB mixture. The NA interface was pinned to a surface defect on the substrate. A fit to the resulting shape of the interface gave the capillary-length information. A plot of  $d_0$  vs.  $x$  ( $x$  is the mole fraction of 10CB in 8CB) shows a crossover from linear to nonlinear behaviour that agrees with the earlier results [15], showing further evidence consistent with the HLM scenario.

### 2.2.8 Thermal transport measurements

Very few experiments have probed critical behaviour of transport properties, on account of the difficulties posed by the physics of the equilibrium phenomena. However, a photopyroelectric technique has recently been used [71, 72] to study the critical behaviour of the specific heat,  $C_p$ , thermal conductivity,  $k$ , and thermal diffusivity,  $D$ , at the NA transition (see Appendix A). In this technique, light from an acousto-optically modulated He-Ne laser was absorbed by a thin metallic coating in contact with one of the liquid crystal surfaces, and the temperature oscillations introduced in the sample were detected on the opposite plate of the sample with a transducer. The quantities,  $C_p$  and  $k$  can be obtained from the amplitude and phase of the signal, while  $D$  can be inferred from the relation  $D = k/\rho C_p$ .

Both planar and homeotropic samples can be prepared in order to study the heat transport parallel and perpendicular to the director. The critical behaviour of  $C_p$  agrees with

other measurements [65] and is independent of the anchoring boundary conditions. Though the values of the thermal transport parameters show a clear anisotropy, the critical behaviour of the thermal diffusivity is isotropic, suggesting that the mode couplings that govern the dynamics associated with the thermal parameters are isotropic.

### 2.2.9 Effects of an external field on the NA transition

Finally, we touch on external field effects at the NA transition. This is especially pertinent as the experiments comprising this thesis use the suppression of nematic fluctuations by an external magnetic field. First, we discuss previous work on non-critical field effects on the nematic order parameter [73, 74] far from the NA transition. Then we discuss the electric-field-induced tricritical point [54], driven by the suppression of  $\delta S$ - $\psi$  coupling. In Chapter 3, we will compare the predicted magnitudes for this effect with the one we predict (via the suppression of the  $\delta n$ - $\psi$  coupling) for the HLM mechanism.

#### Field effects in the nematic

Early work on the effect of the magnetic field on the order parameter in the nematic phase was done by Poggi and Filippini [73]. They measured the variations with magnetic field of the optical phase shift  $\Delta\phi$  introduced by the sample. This phase shift is caused by the anisotropy of the optical dielectric constant. (The nematic is an optically uniaxial medium.) Thus their experiment tested the de Gennes prediction [2, 75] for the field-dependence of the dielectric anisotropy:<sup>15</sup>

$$\langle \epsilon_{\parallel} - \epsilon_{\perp} \rangle = \epsilon_a(T) + \frac{\epsilon_{a0} k_B T \chi_a^{1/2}}{2\pi K^{3/2}} |\vec{H}|. \quad (2.40)$$

They verified the existence of this linear dependence. The coefficient of  $|\vec{H}|$  is small: taking  $\epsilon_{a0} = 1$ ,  $T = 300$  K,  $\chi_a = 10^{-7}$  cgs,  $K = 10^{-6}$ , one finds a correction term of the order  $3 \times 10^{-4}$  for  $H = 10^5$  Oe (10T).

More recently, Lelidis and Durand [74] extended this study by looking at the effect of a large electric field. Typically, when large electric fields are used, one cannot use a DC field;

---

<sup>15</sup>Note that the linear dependence on  $H$  comes from evaluating  $\langle (\delta n)^2 \rangle$ , and is non-analytic at  $H = 0$ . A similar term arises in the NA free energy with an applied magnetic field, when smectic fluctuations are ignored. This is discussed in detail in Chapter 3.

the presence of ionic impurities in most liquid crystals gives rise not only to a screening effect with the charges migrating to the surfaces, but also to an electrohydrodynamic instability. Hence high-frequency AC fields are used, with

$$f^{-1} < \tau \quad (2.41)$$

where  $f$  is the frequency of the applied field and  $\tau$  is the timescale associated with ion mobility. However, the oscillating ions dissipate considerable energy, giving rise to a noticeable heating of the liquid crystal, which is a concern while studying phase transitions. As a result, Lelidis and Durand used a pulsed AC electric field [76]; the duration of the pulses is  $t_{pulse} \approx 100\mu s$  with a time interval between pulses of  $t_{int} \approx 10s$ . The small value  $\frac{t_{pulse}}{t_{int}} \approx 10^{-5}$  improves the temperature-resolution from  $\approx 1^\circ C$  to about 25 mK.

The electric field couples directly to the order parameter magnitude  $S$ . Lelidis and Durand applied electric fields up to  $30V/\mu m$ , equivalent to a 300T magnetic field. In the small-field limit, they confirm the earlier magnetic-field results but also find a quadratic dependence at higher fields. The linear part is due to the quenching of macroscopic angular fluctuations of the director  $\hat{n}$ ; the quadratic part was ascribed to a microscopic field-induced variation of the order parameter (the Kerr effect).

### Electric-field-induced tricritical point

Using the technique described above, Lelidis and Durand [77, 54] studied the effect of an electric field on the I-N-A phase diagram. Their study of the effect of the field on the  $\delta S$ - $\psi$  coupling led to the following conclusions:

1. The IN and NA transitions can be induced by an electric field.
2. The NA transition can be driven second order by a large external field ( $\approx 30V/\mu m$ ). This field effect is one that suppresses  $\delta S$  fluctuations and drives the transition back to second order.
3. They also gave very tentative evidence for the existence of the HLM effect at large fields ( $5V/\mu m$  to  $20V/\mu m$ ) (See Chapter 3).

Moreover, they use the field dependence to estimate values for the Landau parameters for both the IN and the NA transitions (see Appendix B).

### Experimental Summary

A broad range of studies has provided some insight into the nature of the NA transition. These include X-ray scattering (Section 2.2.3), light-scattering, Fréedericks transition measurements and measurements of second-sound resonances and dynamic compression (Section 2.2.4), calorimetry (Section 2.2.5), thermal conductivity (Section 2.2.8), NA front velocity measurements (Section 2.2.6), surface tension (Section 2.2.7) and optical studies in an external field (Section 2.2.9). These experiments provide different windows to look at the NA transition, but a coherent and complete picture is as yet lacking.

Some salient conclusions are:

1. The X-ray scattering studies are clearest on the approach to the tricritical point, where a crossover to tricritical exponents has been observed [78]. In the large nematic range limit, they are weakly consistent with 3DXY exponents [38, 58]; however, the temperature scale is *not inverted*.
2. Elastic-constant measurements, whose interpretation is not gauge-dependent, show an unambiguous weak anisotropy in correlation-length exponents that is at odds with predictions of isotropic exponents.
3. Heat-capacity measurements are in fairly good agreement with the picture of 3DXY behaviour in the type-2 limit and tricritical behaviour in the extreme type-1 limit, with a broad crossover in between. Note, however, that the temperature scale is once again non-inverted.
4. Front-velocity and capillary-length measurements are consistent with the transition being first order beyond (on the larger-nematic-range side of) the LTP.
5. Field effects provide a way of systematically exploring the phase diagram in the region close to the LTP.
6. Thermal transport measurements can shed light on the role of anisotropy in nonequilibrium behaviour.

## 2.3 Conclusion: Assessment of the current understanding of the NA transition

The isotropic models, although not completely correct quantitatively *or qualitatively*, do manage to capture important features of the transition:

- In liquid crystals with large nematic range, the transition is not only indistinguishable from second order, the specific heat exponent is in good agreement with the 3DXY value, and the correlation lengths are not far from the 3DXY values [38, 39].
- Close to the I-N-A triple point, the predicted mean-field tricritical point is observed. Mean-field theory predicts a tricritical point at  $T_{NA}/T_{IN} = 0.87$ ; experimentally, it is observed at much smaller nematic range, at  $T_{NA}/T_{IN} \approx 0.98$ .

### 2.3.1 Near the “Type-2” limit.

At the next level of refinement, however, inconsistencies pop up. In the type-2 limit, the theory of Dasgupta and Halperin [41] predicts an inverted 3DXY universality class, in contradiction with experiment. (Note again that the inverted 3DXY universality class has the same critical exponents as the normal (non-inverted) 3DXY class, but the temperature scale is inverted.) The superconducting analogy has been invaluable in providing an intuition about the NA transition. Further progress, however, seems to involve going beyond this analogy and confronting the effect of the splay term. In the simulations of Dasgupta [47], splay gives rise to a non-inverted temperature scale in the type-2 limit, in agreement with experiment [38]. The field-theoretic, one-loop theory of Patton and Andereck [42, 43] also takes the splay term into account, but a confrontation with experiment still awaits.

Experimentally, the X-ray scattering results are unable to probe the weak anisotropy of the correlation length exponents in a quantitative manner, because the transformation of the 3DXY results to the LC gauge gives rise to inequalities for the values of  $\nu_{\perp}$  and  $\gamma$ . On the other hand, when the exponents are derived from the divergence of the elastic constants (which are gauge-independent quantities), they exhibit a weak anisotropy. Thus, much of the intractability of the NA transition stems from the observation that although experiments show a crude crossover from 3DXY behaviour to tricritical behaviour, they also show a

clear, but weak anisotropy in the divergence of correlations parallel and perpendicular to the director, with  $\nu_{\parallel} > \nu_{\perp}$ .

### 2.3.2 Near the “Type-1” limit

The region close to the LTP poses some fundamental open questions; the question of phase transition order is still not settled. Although the deGennes-McMillan coupling is basically well-understood, the effect of  $\delta n - \psi$  coupling on the order of the NA transition is conceptually more difficult. The Patton-Andereck theory does not address the question of phase-transition order. The HLM theory is strictly correct only in the strongly type-1 limit because it neglects  $\psi$  fluctuations, and its validity for nematic ranges larger than those at the LTP has thus far not been established. This complicated issue can be summed up in the following question:

What effect do smectic fluctuations have on a mean-field *second-order transition* that is driven *first order* when only nematic director fluctuations are taken into account?

Experimentally, Anisimov, Cladis, and coworkers [15, 16] have presented experimental evidence for the existence of the HLM effect. Although they have shown clearly that the transition is first order at the LTP and remains first order for slightly larger nematic range, the existence or position of the true tricritical point remains an unanswered question. The evidence for the HLM mechanism is, however, indirect, and a more direct test is feasible. In particular, as we show in the next chapter, applying a modest external field along the preferred orientation of the nematic leads to effects that may be unambiguously attributed to the coupling proposed by HLM, providing a direct test of the HLM scenario. The experimental search for this “field HLM effect” is a primary motivation for this work. In the following chapter, the theory underlying the HLM effect is presented following the work of Halperin, Lubensky, and Ma [14], but modified to include the effect of a field [79]. Thereafter, we can embark on the search for field effects close to the Landau tricritical point.

## Chapter 3

# THE “HLM” MECHANISM IN AN EXTERNAL FIELD

*We study theoretically the effect of an external field on the nematic–smectic-A (NA) transition close to the tricritical point, where fluctuations effects govern the qualitative behavior of the transition.<sup>1</sup> An external field suppresses nematic director fluctuations, by making them massive. For a fluctuation-driven first-order transition, we show that an external field can drive the transition second order. In an appropriate liquid crystal, we predict the required magnetic field to be of order 10 T. The equivalent electric field is of order 1 V/μm.*

### 3.1 Introduction

We have seen that the fundamental open question close to the Landau tricritical point (LTP) and beyond, in the “type-1” region of the NA transition, is the role played by fluctuations in determining phase-transition order. The simplest approach to studying this problem was proposed by Halperin, Lubensky and Ma [14] (HLM) in 1974. They neglected  $\psi$  fluctuations completely and examined the structure of the Landau-de Gennes free-energy density, Eq. 2.23, after integrating out the nematic fluctuations. The effective smectic free energy contains a new, nonanalytic cubic term, the existence of which would ensure that the transition is always at least weakly first order. This mechanism thus predicts that nothing special

---

<sup>1</sup>This chapter follows closely Ref. [79].

happens at the LTP; there is simply a crossover from a first-order transition mediated by  $\delta S - \psi$  fluctuations to one mediated by  $\delta n - \psi$  fluctuations.

In Sections 2.2.5, 2.2.6, and 2.2.7, we saw experimental evidence for the existence of the HLM effect [80, 15, 16]. Although these experiments suggest the existence of the non-analytic cubic term in the smectic free energy, they do not show unambiguously that this effect arises from the HLM mechanism. One can directly probe the effect of director fluctuations on the nature of the transition by expanding the parameter space of the free energy to include an external magnetic (or electric) field. As we shall see below, the HLM theory, thus modified, gives rise to a peculiar form for the external-field dependence of measured quantities. An experimental observation of this specific form would be hard to attribute to any other mechanism.

In addition, applying an external field affords an experimentalist two other opportunities: First, direct suppression of fluctuation effects provides a continuously variable parameter with which to study the approach to the tricritical point in a single material. In contrast, each data point in mixtures corresponds to a different concentration and is therefore a different experiment. More important, mixtures may differ in properties other than simply the ratio of  $T_{NA}/T_{NI}$ , which complicates the comparison of different experiments. Second, the external field provides a way of suppressing the anisotropic coupling that gives the correlation-length exponents at the NA transition their weak anisotropy. In Sections 2.1.7 and 2.2.9, we discussed a field-induced tricritical point driven by the suppression of  $\delta S - \psi$  coupling. The critical fields involved are large: magnetic fields of  $\approx 300$  T or electric fields of  $\approx 30$  V/ $\mu\text{m}$  are required to make continuous a first-order transition driven by  $\delta S - \psi$  coupling. In what follows, we will show that the subtle fluctuation effects at play at the NA transition can be tuned by relatively modest magnetic (or electric) fields, making concrete predictions that can be checked experimentally.

### 3.2 Derivation of the HLM effect

We now consider the fluctuation-induced first-order phase transition driven by  $\delta n - \psi$  coupling. We start with the Landau-de Gennes free-energy density (Eq. 2.23) [2]. When the coupling of the smectic order parameter with the fluctuations of the partially-ordered nematic order parameter is taken into account, the gradient terms are modified in order to

preserve rotational invariance. For convenience, we rewrite this free-energy in full:

$$\begin{aligned}
F_{NA} &= \int d^3x f_{NA}(\psi, \delta\mathbf{n}) = \frac{1}{2} \int d^3x \left\{ A |\psi|^2 + \frac{C}{2} |\psi|^4 \right. \\
&\quad + C_{\parallel} \left| \frac{\partial\psi}{\partial z} \right|^2 + C_{\perp} |(\nabla_{\perp} - i\mathbf{q}_0 \cdot \delta\mathbf{n}_{\perp})\psi|^2 \\
&\quad \left. + K_1 (\nabla \cdot \delta\mathbf{n}_{\perp})^2 + K_2 (\hat{z} \cdot \nabla \times \delta\mathbf{n}_{\perp})^2 + K_3 \left( \frac{\partial}{\partial z} \delta\mathbf{n}_{\perp} \right)^2 \right\}, \quad (3.1)
\end{aligned}$$

where  $\delta\mathbf{n}_{\perp} = (\delta n_x, \delta n_y, 0)$ . We assume that close to the transition,  $A$  is of the form

$$A = \alpha \frac{(T - T^*)}{T^*} \equiv \alpha t, \quad (3.2)$$

where  $\alpha$  is temperature independent. Note that we have not explicitly included the coupling between the smectic order parameter  $\psi$  and nematic order parameter  $S$ , as the field-dependent shifts are very small. In the absence of  $\delta\mathbf{n}$  fluctuations,  $C = 0$  corresponds to the tricritical point, and  $C > 0$  implies a second-order transition.<sup>2</sup> However, when  $\delta\mathbf{n}$  fluctuations are taken into account, nothing special happens at  $C = 0$ : we merely cross over from a mean-field to a fluctuation-driven first-order transition, as shown in Fig. 2.6. In what follows, we assume  $C \geq 0$  and rederive the HLM effect in the presence of an external field.

We consider the effect of a magnetic field  $H$  along the director  $\hat{\mathbf{n}}$  (assumed to lie along the  $z$ -axis). We assume that the field reinforces the nematic ordering ( $\Delta\chi_a > 0$ ) and neglect its much smaller effects on smectic ordering. Then the Landau free energy becomes

$$\begin{aligned}
F_{NA}^H &= F_{NA} - \frac{1}{2} \int d^3x \chi_a (\mathbf{H} \cdot \hat{\mathbf{n}})^2 \\
&\simeq F_{NA} - \frac{1}{2} V \chi_a H^2 + \frac{1}{2} \int d^3x \chi_a H^2 \delta n^2, \quad (3.3)
\end{aligned}$$

using  $n_z^2 = (1 - \delta\mathbf{n}^2)$ , and expanding in  $\delta n^2$ . Here,  $V$  is the sample volume. Thus, the magnetic field makes the nematic director fluctuations “massive” (see Section 1.4.1). Because the field also couples to the nematic order parameter  $S$ , the free-energy-expansion coefficients also have a magnetic-field dependence [35, 81]; however, this is a much weaker effect than the one we consider here.

In the Halperin, Lubensky, and Ma (HLM) formalism,  $\psi$  fluctuations are ignored. This is valid in the strongly “type-1” limit, discussed in Section 2.1.8). Following HLM, we write

$$e^{-F(\psi)/k_B T} = \int \mathcal{D}\{\delta\mathbf{n}_{\perp}\} e^{\frac{-F_{NA}(\psi, \delta\mathbf{n}_{\perp})}{k_B T}}. \quad (3.4)$$

<sup>2</sup>This tricritical point, induced by  $\delta S$ - $\psi$  fluctuations, is known as the Landau tricritical point (LTP).

Differentiating with respect to  $|\psi|$  gives

$$\frac{df}{d|\psi|} = A|\psi| + C|\psi|^3 + C_{\perp}q_0^2|\psi|\langle\delta\mathbf{n}_{\perp}^2\rangle. \quad (3.5)$$

The director fluctuations  $\langle\delta\mathbf{n}_{\perp}^2\rangle$  can be evaluated using the equipartition theorem in a calculation similar to that in Section 1.4.1:

$$\langle\delta\mathbf{n}_{\perp}^2\rangle = \sum_{\alpha=1}^2 \int \frac{k_B T}{C_{\perp}q_0^2\psi^2 + K_3q_{\parallel}^2 + K_{\alpha}q_{\perp}^2 + \chi_{\alpha}H^2} \frac{d^3q}{(2\pi)^3} \quad (3.6)$$

$$= \frac{k_B T}{\pi} \frac{(C_{\perp}q_0^2\psi^2 + \chi_{\alpha}H^2)^{1/2}}{4K_3^{1/2}} \left( \frac{1}{K_1} + \frac{1}{K_2} \right) \quad (3.7)$$

$$= \frac{k_B T C_{\perp}^{1/2} q_0}{\pi 4K_3^{1/2}} \left( \frac{1}{K_1} + \frac{1}{K_2} \right) (\psi^2 + a_H^2 H^2)^{1/2}, \quad (3.8)$$

where

$$a_H = \sqrt{\frac{\chi_{\alpha}}{C_{\perp}q_0^2}}. \quad (3.9)$$

Putting this back in Eq. 3.5, we obtain

$$\frac{df}{d|\psi|} = \bar{A}|\psi| + C|\psi|^3 - B|\psi|\sqrt{(|\psi|^2 + a_H^2 H^2)}, \quad (3.10)$$

where

$$B = \frac{k_B T C_{\perp}^{3/2} q_0^3}{\pi 4K_3^{1/2}} \left( \frac{1}{K_1} + \frac{1}{K_2} \right), \quad (3.11)$$

and  $\bar{A}$  corresponds to a shift of  $A$ . Note that in this calculation, the only effect of  $K_1 \neq K_2 \neq K_3$  is to replace

$$\frac{1}{K_3^{1/2}} \rightarrow \frac{1}{2K_3^{1/2}} \left( \frac{1}{K_1} + \frac{1}{K_2} \right) \quad (3.12)$$

in the expression for  $B$ . The effective Landau free energy density for  $\psi$  is then given by

$$f_{NA}(\psi) = \frac{\bar{A}}{2} |\psi|^2 + \frac{C}{4} |\psi|^4 - \frac{B}{3} [|\psi|^2 + a_H^2 H^2]^{\frac{3}{2}}. \quad (3.13)$$

Qualitatively, one sees that as  $H \rightarrow 0$  there is a negative  $|\psi|^3$  term, indicating a first-order transition. This is the basic Halperin-Lubensky-Ma effect; the negative cubic term ensures that the transition is always weakly first order, when the assumptions underlying this calculation are valid.

As  $H \rightarrow \infty$ , the last term in Eq. 3.13 gives corrections only to  $|\psi|^2$  and  $|\psi|^4$ , implying a second-order transition. We can express the condition for the crossover from the small  $H$

to large  $H$  in the form of a physical criterion. There are two relevant length scales in this problem. One is the penetration length, defined in Section 2.1.8. At the level of mean-field theory and in the one-constant approximation  $K_1 = K_2 = K_3 = K$ , we can write

$$\lambda = \left( \frac{K}{C_{\perp,\parallel}} \right)^{1/2} \frac{1}{q_0 |\psi_0|}. \quad (3.14)$$

When a field is added, we introduce a new length, the magnetic coherence length  $\xi(H)$ , which measures the distance over which elastic deformations decay in the nematic phase. One finds [2]

$$\xi(H) = \left( \frac{K}{\chi_a} \right)^{1/2} \frac{1}{H}. \quad (3.15)$$

At zero field, if the transition is first order, we can imagine smectic droplets in the nematic phase at the coexistence temperature. Bulk twist and bend excitations penetrate a distance  $\lambda$  into the smectic droplets. When  $H$  is turned on, as long as  $\xi(H)$  is much larger than  $\lambda$ , the nematic-smectic interface is not much affected. But when  $\xi(H)$  is much smaller than  $\lambda$ , nematic fluctuations are suppressed in both the nematic and smectic phases. They then play no role at the transition, which becomes second-order XY. Thus, a rough estimate of magnetic field  $H_c$  needed to reach the tricritical point can be obtained by setting  $\xi(H_c) = \lambda$ . In reality, the different values of  $K_1$ ,  $K_2$ , and  $K_3$  do not change the qualitative argument. In the case where  $\psi$  fluctuations are important, the HLM calculation is not valid; however, the physical criterion based on the relative magnitudes of the magnetic coherence length and *one of the penetration lengths* (in the anisotropic case) is likely to still be valid.

Returning now to our analysis of the field effect on the HLM first-order transition, we expect a tricritical point at

$$H_c \simeq \psi_0/a_H \simeq \frac{1}{a_H} \frac{B}{C}. \quad (3.16)$$

With this in mind, we define the rescaled (dimensionless) variables

$$\begin{aligned} |\psi'| &= \frac{C}{B} |\psi|, \quad A' = \frac{C}{B^2} \bar{A}, \\ H' &= \frac{C a_H}{B} H, \\ f'_{NA} &= \frac{C^3}{B^4} f_{NA}. \end{aligned} \quad (3.17)$$

In terms of these rescaled variables,

$$f' = \frac{A'}{2} |\psi'|^2 + \frac{1}{4} |\psi'|^4 - \frac{1}{3} \sqrt{(|\psi'|^2 + H'^2)^3}. \quad (3.18)$$

For small  $H'$ , we expect the transition to be first order, characterised by three distinct temperatures  $T^{**}$ ,  $T_{NA}$  and  $T^*$  (or equivalently,  $A'^{**}$ ,  $A'_{NA}$ , and  $A'^*$ ) representing the smectic spinodal, the coexistence point and the nematic spinodal. Here,  $T^{**} > T_{NA} > T^*$ . Above  $T^{**}$ , only the nematic phase is stable; below  $T^*$ , only the smectic is stable. One or the other phase is metastable in between. Since almost any experimental technique such as the specific heat, X-ray scattering, light scattering or Fréedericks transition measurements discussed in Section 2.2) can yield measurements of  $T^*$  and  $T_{NA}$ , we characterise the strength of the discontinuity at the transition by

$$t_0(H) \equiv \frac{T_{NA}(H) - T^*(H)}{T^*(H)}. \quad (3.19)$$

If the transition is second order,  $T^{**} = T_{NA} = T^*$  and  $t_0 = 0$ . The value of the order parameter that extremises the Landau free energy obeys, for  $A' < A'^{**}$

$$|\psi'_0|^2 = \frac{1}{2} \left[ 1 - 2A' \pm \sqrt{(1 - 4A' + 4H'^2)} \right]. \quad (3.20)$$

The nematic phase  $\psi = 0$  is also a solution for  $A' \geq A'^*$ . The spinodal temperature  $T^*$  is determined by

$$\left( \frac{d^2 F}{d\psi^2} \right)_{\psi=0} = 0. \quad (3.21)$$

Using the rescaled variables, one finds the spinodal point to be at  $A'^* = |H'|$ , meaning that the spinodal temperature  $T^*$  shifts *linearly* in  $|H|$ . For  $H' > \frac{1}{2}$ , nontrivial solutions to Eq. (3.20) exist only for  $A' < A'^*$  implying that the transition is second order. The tricritical point is located at  $H'_c = \frac{1}{2}$ . Our earlier informal argument giving  $\lambda_{H=0} = \xi_{H_c}$  corresponds to  $H'_c = \frac{2}{3}$ . At the NA coexistence temperature,  $A = A_{NA}$ , we have

$$f(|\psi_0|) = f(0), \quad (3.22)$$

where  $|\psi'_0|$  is given by the positive root in Eq. (3.20). This implies

$$\frac{A'_{NA}}{2} |\psi'_0|^2 + \frac{|\psi'_0|^4}{4} - \frac{1}{3} [|\psi'_0|^2 + H'^2]^{\frac{3}{2}} = -\frac{H'^3}{3}. \quad (3.23)$$

Eqs. (3.20) and (3.23) can be solved, giving us at the coexistence point

$$\begin{aligned} |\psi'_0|^2 &= \frac{2+2\sqrt{1-27H'^2(1-2H')}}{9} && \text{for } 0 < H' < \frac{1}{3} \\ &= \frac{2-2\sqrt{1-27H'^2(1-2H')}}{9} && \text{for } \frac{1}{3} < H' < \frac{1}{2}. \end{aligned} \quad (3.24)$$

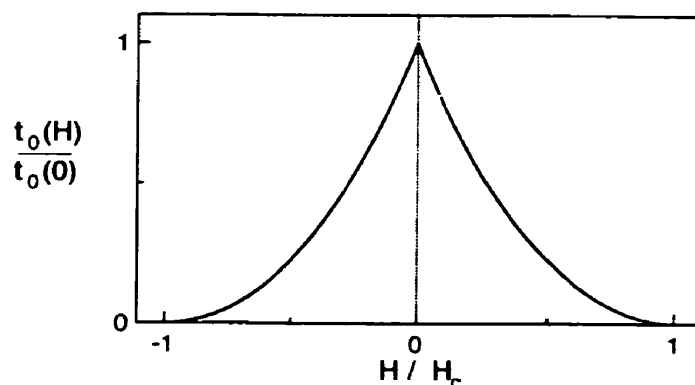


Figure 3.1: Plot of the reduced temperature  $t_0(H) = \frac{T_{NA} - T^*}{T_{NA}}$  as a function of the scaled magnetic field  $H$ . Note the cusp at  $H = 0$ .

Despite appearances,  $\psi_0(H)$  is analytic at  $H' = 1/3$ . (See Fig. 3.2.) The coexistence temperature  $r_{NA}$  satisfies

$$A'_{NA} = -|\psi'_0|^2 + \sqrt{|\psi'_0|^2 + H'^2}. \quad (3.25)$$

Because the spinodal temperature  $T^*$  changes linearly in  $|H|$ , there is a cusp at  $H = 0$  in the function  $t_0(H)$ . (See Fig. 3.1.) A similar linear  $|H|$  dependence also shows up in the nematic phase, far from the NA transition, when one considers the effect of a magnetic field on the birefringence [2, 73].<sup>3</sup> The physics here is essentially the same; it is the long-wavelength director fluctuations that give rise to non-analytic  $|H|$  dependence. The behavior of  $t_0(H)$  near zero field is the non-analytic “signature” of the field-driven HLM effect in the same way that a  $|\psi|^3$  term is the signature of the zero-field HLM effect. Recall that only  $H^2$  figures in the original free energy.

To estimate the magnitude of magnetic field required to drive the transition second order, we consider the material 8CB, where the NA transition appears to be in the HLM fluctuation-driven first-order regime (see Chapter 6). It is useful to express  $H_c$  in terms of the measured value of  $t_0$  at zero field. In the HLM formalism,

$$t_0 = \frac{2B^2}{9\alpha C}, \quad (3.26)$$

<sup>3</sup>This was discussed in Section 2.2.9.

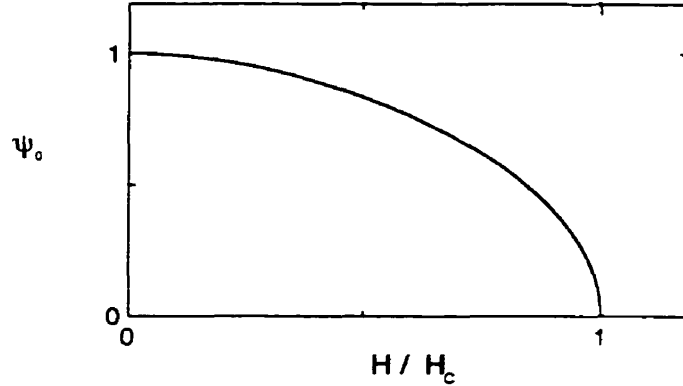


Figure 3.2: The (scaled) smectic order parameter  $\psi_0$  at the transition as a function of  $H$ .

and we have

$$H_c = \left[ \frac{9}{8} \frac{\alpha}{C} \frac{C_{\perp} q_0^2}{\chi_a} \right]^{1/2} \sqrt{t_0} \equiv H_0 \sqrt{t_0}. \quad (3.27)$$

Using  $C_{\perp} = 2 \times 10^{-7}$  dynes,  $q_0 = 2 \times 10^7 \text{ cm}^{-1}$ ,  $\chi_a = 10^{-7}$  c.g.s.,  $\alpha/C \approx 1$ , we estimate  $H_0 \approx 3500$  T, which is the field required to quench fluctuations at molecular scales. Using  $t_0 = 6 \times 10^{-6}$  [82], we obtain the critical field  $H_c \approx 10$  Teslas. For an electric field, the critical electric field is roughly  $1 \text{ V}/\mu\text{m}$ .<sup>4</sup>

These figures are encouragingly low, but one should be cautious since smectic fluctuations, which we have ignored, are important for such weak first-order transitions. The calculation of the critical magnetic field is on firmer ground in the vicinity of the Landau tricritical point ( $u = 0$ ), where the neglect of  $\psi$  fluctuations is more valid. Close to the tricritical point, we retain the  $E \frac{|\psi|^6}{6}$  term in the Hamiltonian. Then the critical field for a second-order transition is

$$\frac{1}{a_H} \left( \frac{B}{E} \right)^{1/3}. \quad (3.28)$$

The expression for  $H_c$  in this case is

$$H_c = \left[ \left( \frac{4\sqrt[3]{2}\alpha}{E} \right)^{1/2} \frac{C_{\perp} q_0^2}{\chi_a} \right]^{1/2} t_0^{1/4} \quad (3.29)$$

In the 8CB-10CB system studied by several groups[46, 69], the LTP occurs at a mole fraction of roughly 40% 10CB in 8CB. In this system, we have measured  $t_0$  to be roughly  $10^{-4}$  (see

<sup>4</sup>In comparison, the field effects to suppress the  $\delta S$ - $\psi$  coupling, discussed in Sections 2.1.7 and 2.2.9 are much weaker: there, the critical fields required to drive the transitions second order are  $\approx 300$  T or  $30 \text{ V}/\mu\text{m}$ .

Chapter 6). Unfortunately, the  $t_0^{1/4}$  dependence then results in a much higher critical field, on the order of 300 T ( or roughly 30 V/ $\mu\text{m}$ ).

Lelidis and Durand have extensively studied the effects of large electric fields on the NA transition [77, 54]. In his Ph.D. thesis, Lelidis looked for evidence of an electric field-induced tricritical point at the NA transition of 8CB. The experiments, which measure  $S$ , give some evidence for a tricritical point at an external electric field somewhere between 5 and 20 V/ $\mu\text{m}$ . Unfortunately the temperature resolution was 25 mK. Since the zero-field discontinuity is only 4 mK, this does not rule out a much smaller critical field for 8CB, and better temperature resolution will be needed to confirm these results.

The HLM effect for the NA transition leads to an unusual, non-analytic form for the effective smectic free energy in the presence of an external field. In particular, it predicts that the field required to drive a first-order transition mediated by  $\delta n$ - $\psi$  coupling is significantly smaller than that required to suppress the  $\delta S$ - $\psi$  coupling mechanism. This is a happy situation experimentally: not only is the critical magnetic field  $H_c$  predicted to be small ( $\approx 10$  T), but the non-analytic cusp close to  $H = 0$  is in itself a signature of the HLM mechanism. Thus, precise experiments on the field dependence are an extremely promising way to attempt to understand the physics of the NA transition close to the LTP. This is explored experimentally in the following chapters.

## Chapter 4

# EXPERIMENTAL APPARATUS AND TECHNIQUES

*A description of the optics and temperature-control system that was designed specifically for this experiment, and a compendium of the sample-preparation and other experimental methods used.*

### 4.1 The Design of a Real-Space Technique

#### 4.1.1 Motivation for a study in real-space.

When one looks at a nematic liquid crystal through crossed-polarisers in an optical microscope, one notices local light-intensity fluctuations that resemble the noise one sees on a television screen, with both spatial and temporal variations. In the smectic-A phase, these fluctuations are not seen. This difference arises because the long-wavelength orientational fluctuations in the nematic are soft modes. In normal isotropic liquids, thermal fluctuations can induce fluctuations of the dielectric constant tensor  $\bar{\epsilon}$ , at small length-scales (large  $k$ , where  $k \equiv 2\pi/\lambda$ ,  $\lambda$  being the wavelength of the spatial fluctuations); however, long-wavelength (small  $k$ ) modulations of  $\bar{\epsilon}$  in the smectic would imply a uniform dilatation that requires a large elastic energy. The large- $k$  fluctuations of the dielectric constant in the nematic and smectic-A phase are not too different from each other. However, in the nematic, fluctuations in  $\bar{\epsilon}$  can be induced merely by rotation of the optical axis, which for  $k \rightarrow 0$  costs

very little energy. In the smectic phase, twist and bend distortions are expelled, and only splay distortions, which correspond to layer bending (see Fig. 1.3), are allowed. Thus, these long wavelength fluctuations, which are absent in the isotropic phase and suppressed in the smectic-A phase, are extremely strong in the nematic phase.

Following this logic, one should look at long wavelengths ( $k \rightarrow 0$ ) to probe most sensitively the transition from nematic to smectic-A. One can do this in reciprocal space, via small-angle light scattering, or in real-space via microscopy. Each way has its own advantages: light-scattering techniques are well-established, and the theoretical machinery relating the experimentally measured signal to theoretically calculated correlation functions already exists. The advantage of real-space microscopy is that it gives a spatially resolved signal, with points on the image that are separated by more than a correlation length being essentially independent observations. This allows a careful spatial characterisation of the sample, not usually done in scattering. Close to the phase transition, any temperature gradients across the sample result in gradients in intensity fluctuations. Averaging over them will inevitably reduce the temperature resolution. In light scattering, the scattering volume is often chosen small for these reasons. In real space, however, we can characterise the fluctuation gradient that arises from the thermal gradient by calibrating it against changes in temperature and thus easily improve the effective temperature resolution by dividing the image into several isothermal strips.

Moreover, since we are more sensitive to long-wavelength fluctuations in the nematic, microscopy affords the rare luxury wherein one has higher sensitivity at lower magnification. Light-scattering, in contrast, gets harder as one goes toward  $k \rightarrow 0$ . In crossed-polariser microscopy, all the light that passes through the sample unaltered is cut off by the analyser whose axis is perpendicular to the polariser. Thus, when a sample in the isotropic phase is placed between crossed polarisers, plane-polarised light passes through the sample with its polarisation state unchanged and is thus blocked by the analyser. When the sample is in the nematic or the smectic-A phase, both of which are birefringent and optically uniaxial, the sample acts, to a first approximation, as a waveplate, and the transmitted light intensity is simply related to the incident light intensity and the angle  $\theta$  made by the sample and the polariser,

$$I = \frac{I_0}{4} \sin^2 2\theta \sin^2 \Gamma, \quad (4.1)$$

where  $\Gamma = \frac{2\pi}{\lambda}(n_e - n_o)$ ,  $n_e$  and  $n_o$  being the ordinary and extraordinary refractive indices. The above neglects the fluctuations of the nematic optic axis, which causes this intensity to fluctuate spatially and temporally. It is these intensity fluctuations that we use as a measure of the director fluctuations in the nematic.

The real-space technique designed during this thesis (heretofore called “intensity fluctuation microscopy”) can address two questions:

- The first is the order of the transition. Since the intensity fluctuations are related directly to the orientational order, one can use it to look for a discontinuity at the phase transition.
- Second, the intensity fluctuations can be related to the elastic constants in the nematic, and one can therefore also measure the divergence of the correlation lengths on approaching the transition.

The details of the apparatus designed in developing the intensity fluctuation microscopy technique are described in this chapter. The characterisation of the technique itself is also discussed in detail in the Chapter 5.

#### 4.1.2 Quantitative Microscopy

It is useful, at the outset, to say a few words about the basic sample geometry, as it will be referred to implicitly and explicitly throughout this chapter (see Fig. 4.1). The liquid crystal is sandwiched between two glass substrates, and the optic axis of the liquid crystal in the experiments in this thesis is always in the plane parallel to the bounding substrates. The substrates, shown in Fig. 4.1(c) and Fig. 4.2 lie in the plane perpendicular to the direction of the light path, shown in Fig. 4.2. The liquid-crystal sample has two large dimensions  $L \approx 1.5$  cm (see Fig. 4.1(b)) in the plane parallel to the substrate, and one smaller dimension  $d$  (see Fig. 4.1(c)) that may be set from 1 to 100  $\mu\text{m}$  in the dimension perpendicular to the substrate. This dimension is referred to as the thickness dimension. This axis also coincides with the axis of the optical path. Thus, in our experiment, we are sensitive to director rotations in the plane (i.e., the plane parallel to the substrate), but much less so in the dimension perpendicular to the substrate.

The original idea to look at intensity fluctuations as a way of differentiating the nematic phase from the smectic-A phase grew out of an experiment intended to study equilibrium

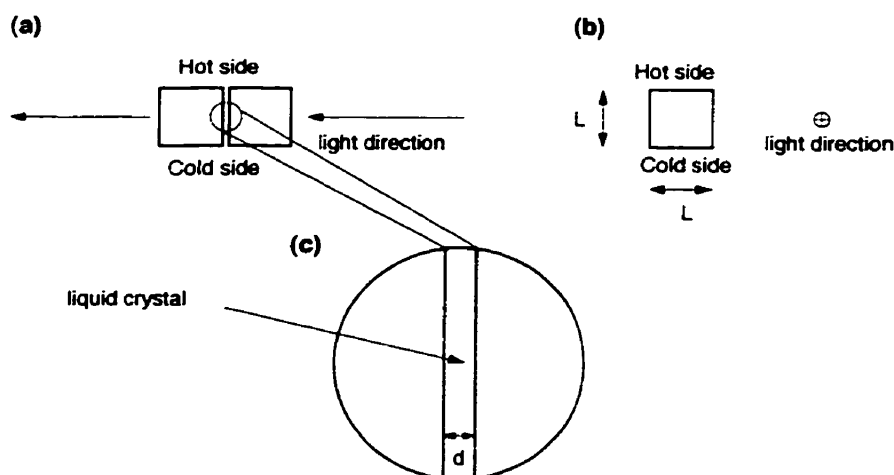


Figure 4.1: Sample geometry. (a) Side view: light direction is from left to right. (b) Front view: light direction is into the paper. (c) Expanded region of (a) in the liquid crystal gap between the glass substrates.

crystal shapes. Our first set-up involved placing the sample inside a copper cell in a commercial hot stage [83], mounted on an transmission optical microscope [84] between crossed polarisers. Since the top plate of the sample was not in contact with the oven, there was a significant temperature gradient across the thickness of the sample. There was a ( $\approx 0.1^\circ\text{C}$ ) temperature gradient, too, in the plane of the substrate as well (corresponding to tens of mK across the field of view); this gradient was uncontrolled but could be calibrated after the fact. Whereas the temperature gradient in the thickness direction is an inherent limitation to resolution, we were able to use the in-plane temperature gradient to our advantage (see Section 5.2). However it was, in practice, delicate to obtain a suitable gradient on the commercial hot-stage and we designed a new sample cell (see Fig. 4.2), which would not only have better temperature stability than the commercial hot stage, but would also have a symmetric design to minimise stray gradients.<sup>1</sup>

The physical dimensions of this hot-stage were  $20\text{ cm} \times 10\text{ cm} \times 8\text{ cm}$ ; it was designed to fit in between the poles (8.5 cm apart) of an electromagnet<sup>2</sup> with a magnetic field ranging

<sup>1</sup>An early conceptual design of the optics and temperature control arose out of an afternoon discussion with David Cannell. Also invaluable during the design stage was the Ph.D. thesis of Art Bailey [85].

<sup>2</sup>I would like to thank Professor B. Heinrich and his research group for generously allowing me access to their magnet.

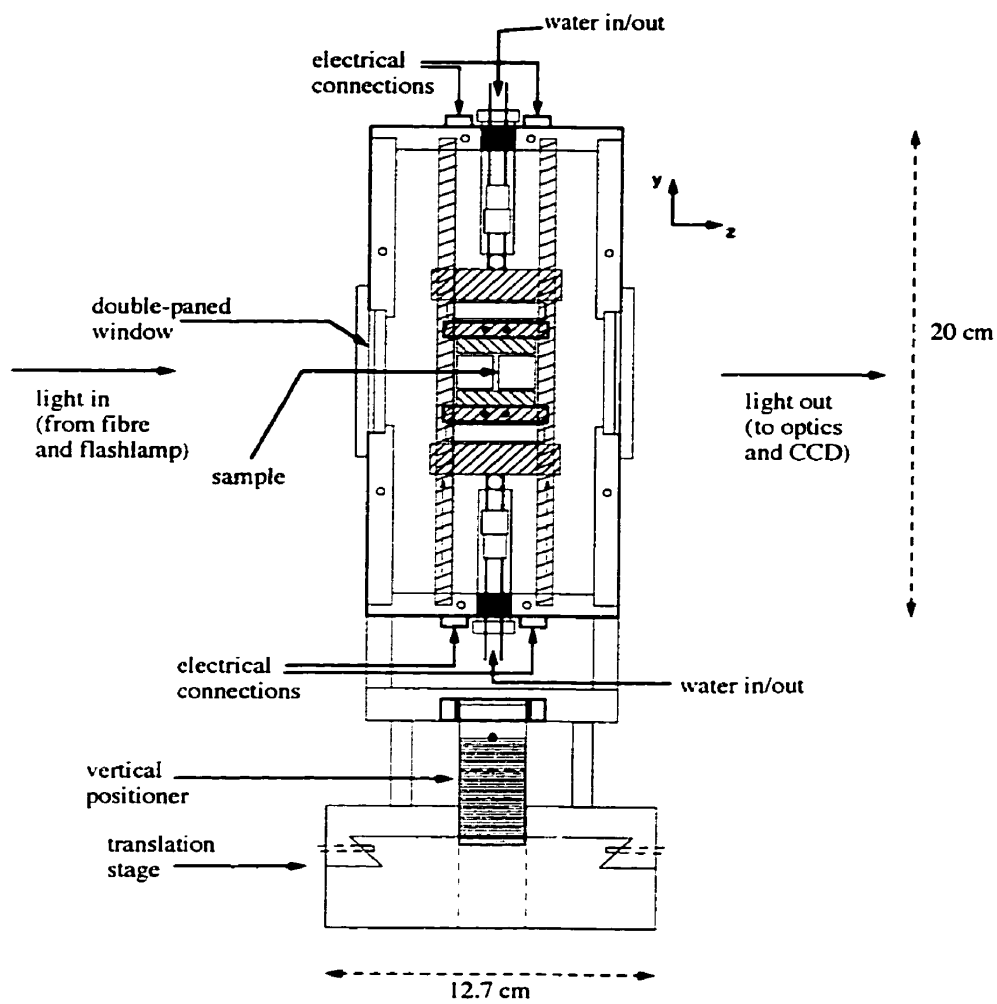


Figure 4.2: Schematic overview of the design of the temperature gradient oven. The imposed gradient is vertical in this diagram.

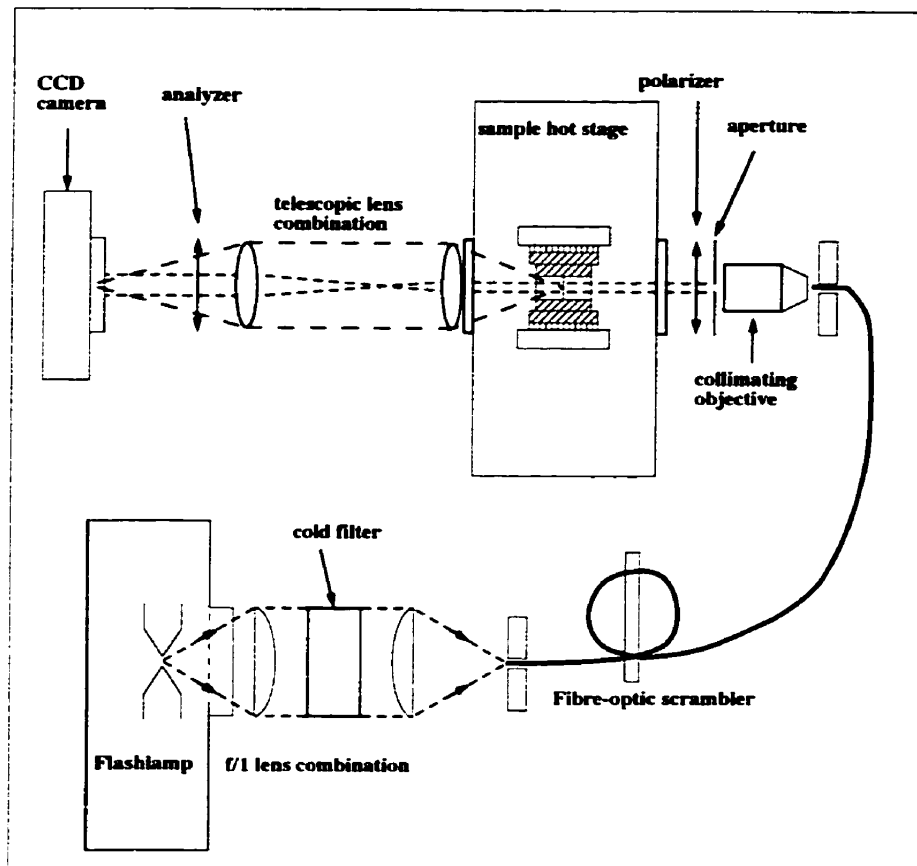


Figure 4.3: Schematic of the optical system.

from 0-1.5 T. The optics were designed around the constraint that the outer window of the hot stage be 5 cm from the centre of the sample, thus requiring a working distance greater than 5 cm. As a result, a conventional microscope could not be used; the optical set-up was basically a home-built “ultra-long-working-distance” microscope, set up horizontally on an optical rail.

## 4.2 The Optical System

The optical system consists of the light source, the polariser, the sample-cell, the imaging lenses, the analyser, and the CCD camera (see Fig. 4.3).

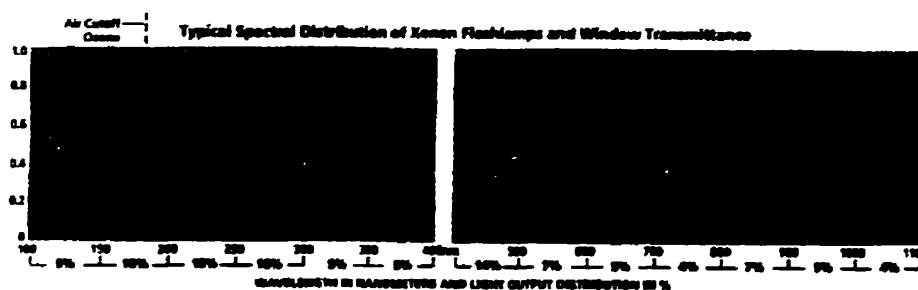


Figure 4.4: Spectral output of the flashlamp. (Ours had a borosilicate window.) [87]

### 4.2.1 Optics

#### The Light Source

The “light source” of the optical system (see Fig. 4.3) consists of a flashlamp source, a cold filter, a fibre-optic scrambler, and a collimating lens.

The flashlamp source [86] has a flash duration  $\approx 10 \mu\text{s}$ ,<sup>3</sup> with a maximum flash energy of 0.5 J, subject to a maximum continuous power of 20 W. The light comes from a 1.5 mm-long arc.<sup>4</sup> The arc lamp provides a high brightness over a very short time, which is exactly what is needed for imaging fluctuations. However, the intensity distribution is highly non-uniform over the extent of the arc. The spectral distribution of light from the flashlamp is shown in Fig. 4.4.

One can make the illumination more uniform with a “light-scrambler.” It is useful to incorporate this into the design of the light source because the ideal light source is completely featureless, while the flashlamp itself has a very non-uniform spatial distribution of intensity as the light emanates from a spark between two electrodes. The light-scrambler, made after the design of Ellis<sup>5</sup> [89] uses a 1-mm-core plastic optical fibre bent in a loop of diameter  $\approx 15$  cm. The large core diameter was chosen to match the arc length of the flash lamp. The light, travelling through the fibre by repeated total internal reflections has its modes azimuthally scrambled when it traverses a tight loop. Higher-order modes leak out more easily, so that the bent fibre roughly acts as a low-pass filter. The one-loop scrambler

<sup>3</sup>The optical pulse duration is defined to be twice the time between the peak and 1/3 peak.

<sup>4</sup>As the electrodes wear through use, the arc gets longer.

<sup>5</sup>see also Ref. [88], footnote on p. 127

produces a light source at the other end of the fibre that varies radially, but is azimuthally uniform. The radial variation of intensity is  $\approx 15\%$ , while the azimuthal variation is  $\approx 3\%$ .

The cold filter is made from two cold mirrors (which transmit in the infrared and reflect the "cold" light) that are  $3\text{ cm} \times 5\text{ cm}$  pieces cut from a larger plate [90]. The cold filter reduces perturbations to the sample temperature caused by the light flashes. Only 5% of the "hot light" is reflected from each mirror; the rest passes through the mirror and is thus conveniently excluded from the visible part of the beam. There is also an ultraviolet component to the beam which is largely absorbed by the glass in all the lenses and windows in the optical path. The two mirrors are placed at a  $45^\circ$  angle with respect to the light direction. The light reflects at right angles off the first mirror and again off the second mirror before entering the collimating lens. Thus, only 0.25% of the heat carried by the beam is transmitted past the cold filter. (It was found that the heating effect, even without the cold filter, was not significant. Therefore, it is not used in situations where the overall transmitted light intensity is small.)

The flashlamp is optically coupled to the fibre scrambler via two 15 mm focal length  $f/1$  planoconvex lenses.<sup>6</sup> The first one collimates the light from the flashlamp, while the second one focuses the collimated beam back onto the optical fibre.

A 10X,  $N.A. = 0.3$  microscope objective [84] is used in reverse to collimate the light emanating from the 1 mm optical fibre, sending approximately parallel light through the sample.

---

<sup>6</sup>The f-number is defined as

$$f_{number} = f/D, \quad (4.2)$$

where  $f$  is the lens focal length, and  $D$  the lens aperture. The numerical aperture  $N.A.$  is defined as

$$N.A. = n \sin \theta, \quad (4.3)$$

where  $\theta$  is the half-angle subtended at the aperture of the objective by the focal point, and  $n$  is the refractive index of the medium of transmission. In the small-angle approximation,

$$N.A. \approx D/2f = 1/2f_{number}. \quad (4.4)$$

### Inside the sample holder

The sample cell itself has 4 pieces of anti-reflection coated glass; i.e. two pairs of double-paned windows (to minimise heat loss) on either side of the sample. The liquid crystal sample is a thin sandwich between two 15 mm high  $\times$  15 mm wide  $\times$  12.7 mm thick glass cubes [91]. The cubes were cut from  $\frac{1}{2}$ -inch  $\lambda/8$  optical flats; thus two opposite surfaces were  $\lambda/8$  optical quality, two others were optically clear, while the last pair of surfaces was machined flat. These cubes were polished in pairs in order that the dimensions of the two cubes in a pair be matched to better than 0.05 mm. Throughout the light source and sample, the numerical aperture of the optics is matched to be  $N.A. \gtrsim 0.25$  where  $n = 1$  for air.

### The Imaging System

On the output side, there are two achromatic lenses arranged in a telescopic configuration, with the spacing between the lenses being the sum of their focal lengths. The lens closest to the sample was either a 60 mm focal length (f.l.) or a 75 mm f.l. lens. The second lens was chosen from a variety of focal lengths ranging from 125 mm f.l. to 300 mm f.l. to vary the magnification from  $2\times$  to  $5\times$ . At a magnification of  $5\times$ , the resolution is given by

$$R = \frac{\lambda}{2N.A.} \approx 1 \mu\text{m}. \quad (4.5)$$

From the Nyquist criterion (see Ref. [88]), one needs two pixels spanning any length scale that one wishes to resolve. At this magnification, the extent of the region in the sample that was projected onto the  $6.8 \mu\text{m}$  dimension of a pixel, was  $1.36 \mu\text{m}$ , a bit short of the  $2 \mu\text{m}$  required by the sampling theorem. At the lower magnification, the Nyquist criterion was satisfied: in comparing magnifications, no effects of aliasing were observed at higher magnification.

The telescopic configuration has the advantage that the parallel light incident on the sample containing the information about the source is unfocussed at the CCD chip. A similar trick, known as Köhler illumination, is used in bright-field microscopy [88].

The camera is a 12-bit digital CCD [92], with  $1317 \times 1035$  pixels, each of which are  $6.8 \mu\text{m} \times 6.8 \mu\text{m}$ , corresponding to a chip area of  $9 \text{ mm} \times 7 \text{ mm}$  with no dead space between the pixels. Because the fluctuations we measure are typically only 1% of the mean intensity, the 12-bit grey-scale resolution was important. It provided 30 grey levels over the range

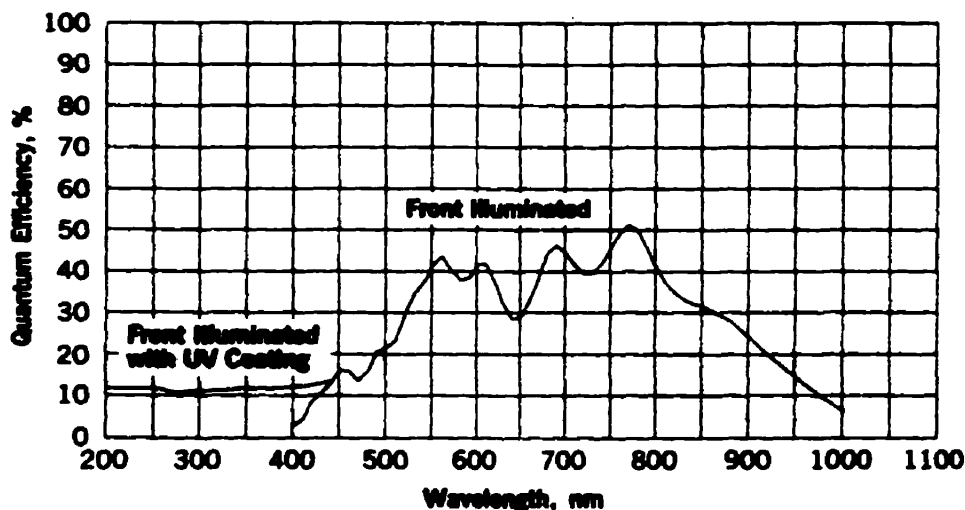


Figure 4.5: Spectral response of the CCD (ours had no UV coating.)

of fluctuations, while on an 8-bit camera the full range was only two grey levels. A more detailed calibration of the camera is discussed in Chapter 5.

Apertures on either side of the sample stage controlled the cone of angles over which light was accepted into the sample, and the cone of angles over which light was accepted into the telescope lens system. When the apertures were stopped down, the light was approximately parallel (angular spread of the beam envelope  $\simeq 0.005$  rad). When the apertures were wide open (angular deviation of the beam envelope  $\simeq 0.05$  rad), the sample was flooded with light. The experiment was conducted at intermediate apertures which reflected a compromise between the amount and the parallelism of light. Note, though, that using non-parallel light makes theoretical analysis of the imaging process harder.

An alternate arrangement was to stop down the aperture and add a green interference filter in order to create quasi-monochromatic light. Both the aperture and the filter reduce the light intensity, but binning the images increases the light level per pixel. The choice of filter is based on matching the spectral output of the flashlamp (see Fig. 4.4) and the spectral response of the CCD chip (see Fig. 4.5) in the visible part of the spectrum. The wavelength 550 nm is not a maximum for either spectral curve, but is, in fact, close to the maximum value for the *product* of the two curves. Two-by-two binning of pixels on the CCD chip decreased the number of pixels in the image by a factor of four, concurrently increasing

the pixel size and thus the light level by the same factor. This arrangement allowed us to bypass the problems associated with off-parallel light rays.

The final element of the imaging system is the computer [93] and the image-processing software [94, 95]. Two images were captured on screen, and the data analysis (image subtraction, normalisation, etc.) was done in single-precision arithmetic [95].

### 4.2.2 Optical Adjustments

Positioning the lenses is an important step in a system where the light originates from an extended source. The method of positioning involved three steps: alignment and focussing of the beam, positioning of the camera with respect to the beam with no sample or receiving lenses, and alignment of the sample and receiving lenses.

The “output” end of the optical fibre, the collimating objective, the sample, and the imaging system were all assembled on an optical rail [96] making all distances adjustable. This rail was horizontal so that the entire assembly could be fit between the poles of the electromagnet. (Note, too, that vertical orientation of this rail was not feasible. Because the hold lock was inadequate, the optical mounting plates tend to slide gradually.)

The collimated beam was first aligned vertically with a sliding, vertically mounted ruler. The objective was positioned such that the beam centre would remain unchanged as the ruler was slid from up close to about 2 m away (the extent of the rail). Next, the CCD camera was positioned so that the beam was centred on the camera. Once this was done, the beam was imaged to look at the spatial distribution of the light intensity. Since it is possible that the fibre direction and the collimating objective are *compensatingly misaligned*, this check is essential: only if they are aligned will the centre of the beam envelope correspond to the centre of the radial spatial variation of the beam intensity. The camera was then moved forward and back across the length of the rail as a further check.

The telescope lens combination was then put in, *one at a time*. First the lens close to the sample was positioned for parallelism of the beam, and the orientation adjusted to centre the intensity distribution of the image on the computer screen. The beam in this case was diverging. Then the second lens was positioned. This time, the beam exiting the lens was collimated when the distance between the two lenses was the sum of their focal lengths. The focussing was fairly tedious, as the camera, having a 1 MHz pixel-read-out rate, updated

images at only 1 – 5 Hz. The update rate for a full frame ( $1317 \times 1024$  pixels) is roughly one second. For smaller image sizes, the update rate should scale inversely with the image size; however the update time for a  $100 \times 100$  pixel area is in fact no faster than 0.2 second. This is most likely a limitation of the camera driver software.

Finally, the sample stage was put in, without the sample in it. Here, attention was paid to the orientation of the windows with respect to the beam direction. Manual adjustments were made only if the intensity distribution in the field of view changed noticeably. Since the window panes are 3 mm thick, there was no appreciable deviation of the beam due to slight misalignment. However, the orientation of the sample itself, whose overall thickness was 25 mm, was more crucial and was done again by monitoring the intensity distribution while tweaking the in-plane orientation of the sample.

### 4.2.3 Depth of Field

The depth of field is given by a combination of two terms, arising from geometric and wave optics, respectively. The total depth of field (see Ref. [88], p. 48) is given by:

$$d_{tot} = \frac{\lambda_0 n}{N.A.^2} + \frac{n}{M \cdot N.A.} e, \quad (4.6)$$

where  $N.A.$  is the numerical aperture of the imaging lens,  $\lambda_0$  the light wavelength,  $n$  the refractive index of the medium of light transmission (air in this case),  $M$  the magnification of the optical system, and  $e$  the dimension of the imaging detector. For the optical imaging system in this experiment

$$M = 5$$

$$e = 6.8 \mu\text{m}$$

$$N.A. = 0.25$$

$$\lambda \approx 0.5 \mu\text{m}$$

The depth of field  $d_{tot}$  as a function of  $N.A.$ , plotted in Fig. 4.6 illustrates the relative contribution of the geometric and wave optics terms. For a numerical aperture of  $N.A. = 0.25$ , the value of  $d_{tot}$  is seen to be roughly  $20 \mu\text{m}$ .

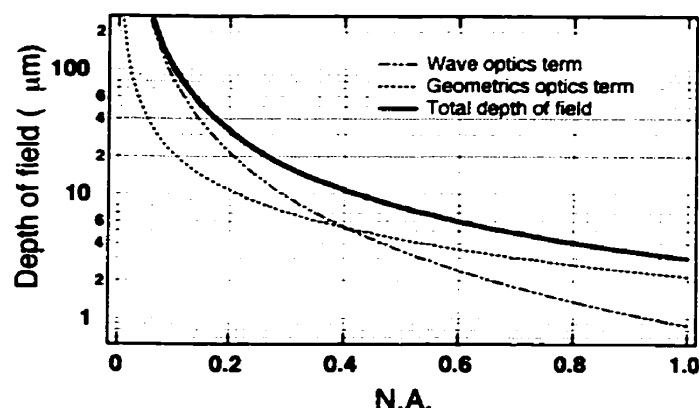


Figure 4.6: The depth of field has a wave-optics contribution and a geometric-optics contribution. The depth of field for the N.A. = 0.25 optics in this experiment is  $\approx 20 \mu\text{m}$ .

### 4.3 The Sample Hot Stage — Elements and Design

The sample cell hot stage (shown in Fig. 4.2) was designed around the requirement of a uniform, controlled temperature gradient. To ensure this, the time constants for heat transfer in the vertical direction should be larger than that for heat exchange with the surrounding air. Moreover, to independently control the top and bottom of the sample, the time constant of heat transfer through the sample should be much longer than the time between updates in the temperature control.

The thermal diffusion coefficients in Table 4.1 give a rough idea of equilibration times in different materials. For example, the copper piece in contact with the sample cell, is roughly 0.5 cm in extent. We can estimate equilibration times via dimensional analysis and the diffusion equation:

$$\tau_{\text{copper}} \approx \frac{L^2}{D} = \frac{1/4 \text{ cm}^2}{1 \text{ cm}^2/\text{sec}} = \frac{1}{4} \text{ sec.} \quad (4.7)$$

One thus needs to update the voltage in the thermoelectric heater/cooler (“Peltier” element; see following section for description) only on times on the order of seconds, and the control can easily be done in software.

In the glass, however, the time constants are much longer:

$$\tau_{\text{glass}} \approx \frac{1 \text{ cm}^2}{3.5 \times 10^{-3} \text{ cm}^2/\text{sec}} = 300 \text{ sec.} = 5 \text{ min.} \quad (4.8)$$

This ensures that the liquid crystal, a thin 20 – 100 μm layer sandwiched between thick

	Thermal Conductivity $\kappa$ (watt/cm K)	Specific Heat $C_p$ (J/g K)	Mass Density $\rho$ (g/cm <sup>3</sup> )	Thermal Diffusion Coefficient $D_q = \kappa/C_p\rho$ (cm <sup>2</sup> /s)
<i>Silver</i>	4.2	0.24	10.50	1.67
<i>Copper</i>	3.9	0.39	8.96	1.11
<i>Aluminium</i>	2.0	0.9	2.70	0.82
<i>Brass</i>	0.9	0.38	8.48	0.28
<i>Glass</i>	$7.1 \times 10^{-3}$	0.8	2.51	$3.5 \times 10^{-3}$
<i>Ice</i>	$2.2 \times 10^{-2}$	2.22	0.92	0.01
<i>PVC</i>	$1.67 \times 10^{-3}$	1.2	1.4	$1.0 \times 10^{-3}$
<i>8CB</i>	$1.5 \times 10^{-3}$	2.5	0.98	$0.6 \times 10^{-3}$
<i>Ethanol</i>	$1.7 \times 10^{-3}$	2.43	0.79	$0.9 \times 10^{-3}$
<i>Water</i>	$6.0 \times 10^{-3}$	4.19	1.0	$1.4 \times 10^{-3}$
<i>Foam</i>	$2.4 \times 10^{-4}$	—	—	—
<i>(Still)Air</i>	$2.3 \times 10^{-4}$	1.04	$1.2 \times 10^{-3}$	0.18

Table 4.1: Thermal constants for some common non-magnetic materials (from ref. [97, 98, 99])

glass blocks, will drift in temperature very slowly. The temperature thus does not change appreciably during the course of the measurements, which take a few seconds.

The system was made completely from non-magnetic materials, so that it could be placed in an electromagnet. The top and bottom sides of the sample were independently temperature controlled, in order to create a controllable temperature gradient in the vertical direction (see Fig. 4.7). The sample cell was designed to have left-right and back-front symmetry, and at least nominally, up-down symmetry, as well. The up-down symmetry was only nominal because the temperature of the top and bottom of the sample differed with respect to the ambient temperatures.<sup>7</sup> The sample was isolated from the walls of the cell by polyurethane foam and by air. The foam has a thermal conductivity only marginally greater than that of still air, but since it suppresses convection, it is in fact superior to air as an insulator. The walls were made of PVC, which has a low thermal conductivity yet is

<sup>7</sup>They were, on the other hand, symmetric with respect to the observation temperature.

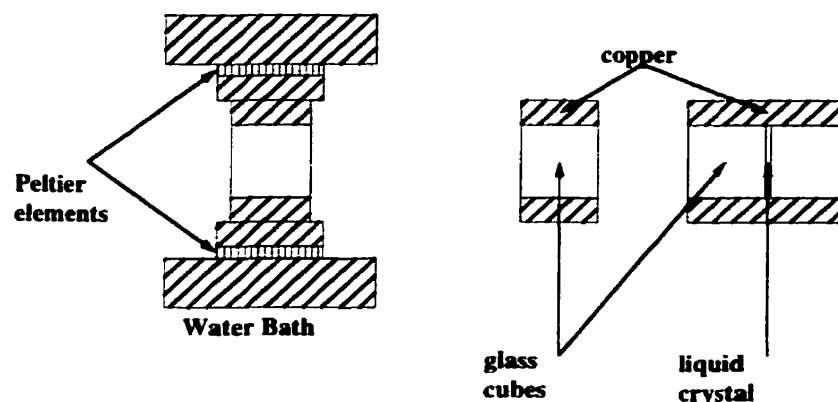


Figure 4.7: Schematic of gradient hot stage.

fairly rigid and is easy to machine. The windows were the greatest source of heat loss. As a result, we used double-paned windows with an air gap of about 0.5 cm between them to reduce heat loss due to conduction. However, an important source of heat loss is radiation (on the order of 50%). The windows were, however, chosen to be much larger than the sample extent to minimise temperature non-uniformity across the sample, which was the primary concern.

## 4.4 Temperature Control

### 4.4.1 Hardware

The temperature of the copper blocks at the top and bottom of the sample was controlled coarsely by two water-cooled copper blocks. The cooling water was controlled independently by two water heaters [100], each of which with a nominal temperature stability of 10 mK.

### The Elements

The temperature control loop hardware has the following elements:

1. Temperature probes were platinum RTDs. The temperature resolution of the sensor is determined by three factors: the slope of the resistance-temperature curve at the point of operation, the noise in the sensing element, and the noise in the electronics. Thermistors have a steeper resistance-temperature relation than RTDs and are hence

more more sensitive. For a given temperature, it is easy to find a thermistor that gives a sub-milliKelvin temperature resolution. However, all the thermistors we tried had a significant magnetoresistance. Therefore, for magnetic field measurements, we had to use platinum resistors instead. RTDs that had a nominal resistance of  $2000\ \Omega$  at  $0^\circ\text{C}$  were used [101]. The more common  $100\ \Omega$  RTDs have the same temperature-coefficient ( $\approx 0.4\%/^\circ\text{C}$ ). However, since the base resistance is 20 times higher, the resistance change per degree was  $\sim 8\ \Omega$ , as opposed to  $\sim 0.4\ \Omega$ , allowing easier measurement by our multimeter. The RTDs were embedded in a copper block between the glass cubes and the Peltier element. For fine temperature control, the sample was separated thermally from each water-heated copper block by a Peltier element [102], the current to which was which was controlled in a feedback loop described below in Section 4.4.2.

2. The measurement resolution was enhanced by measuring not the bare resistance of the RTD itself, but the voltage from a DC Wheatstone bridge that was nearly balanced. The power supply for each Wheatstone bridge circuit was a 1.55 V silver-oxide battery [103], chosen for stability over a regulated power supply.<sup>8</sup> Thus we measured small voltage (resistance) deviations from zero rather than the base resistance. Using a bridge  $1^\circ\text{C}$  from its balance point rather than the RTD directly increased the sensitivity from  $0.4\ \%/^\circ\text{C}$  to  $67\ \%/^\circ\text{C}$ . The other resistance arms used  $R = 2000\ \Omega$ .
3. The A-D conversion was done by two Keithley 2001 multimeters [104] with 7.5 digit resolution. I originally used a single Keithley with a multiplex scanner to switch between the inputs, but transient noise during the switching affected the control.
4. The Keithley multimeters and the D-A on a lock-in amplifier[105] were controlled in software via a GPIB interface card [106] in a Macintosh IIfx computer. Readings were taken and the digital output signal for each control loop updated approximately once every two seconds.
5. Four D-A converters. We used the four 16-bit D-A converters that are part of a lock-in amplifier.<sup>9</sup> These have a full-scale maximum of 10 V and a resolution of 1 mV. Note that it was essential not to use the time-proportioning, on-off outputs found in cheaper

---

<sup>8</sup>The design draws heavily from a similar one in the Ph.D. thesis of Art Bailey [85].

<sup>9</sup>These D-A converters were handy in the lab; we did not actually use the lock-in functions themselves.

commercial PID controllers. The noise that on-off swings make on a 2 sec time scale is  $\gtrsim 10$  mK. In our set-up, the resolution of the D-A convertors was 1 mV. The output of 2 channels of the D-A was fed to a simple voltage divider circuit that stepped down the voltage by a factor of 80 or 400, corresponding respectively to a coarse or fine setting, selectable by turning a relay on or off.

6. These voltage outputs then went into the analog programming card of a 15V (maximum voltage), 4 A (maximum current) dual power supply [107], and each channel thus supplied a current to a thermoelectric (Peltier) element. Varying the input to the power supply from 0 V to 10 V varied the output of the power supply from 0 A to 4 A.
7. The Peltier element is a thermoelectric heater/cooler. It has a quick response to changes in the driving current, and the direction of the heat flow switches with the direction of the current. The Peltiers were, however, not used symmetrically about zero, but around a small value offset up or down from zero. This slows the response time but avoids any switching noise due to reversal of the driving current.

### The Temperature Characteristics of the Hardware

Several elements influence the temperature characteristics of the hardware. The output-current sensitivity and range was set by the D-A converter, the voltage divider and the power supply. The maximum current supplied by the power supply was set by the 10 V maximum voltage of the D-A converter and the coarse setting of the voltage divider—it corresponded to a maximum output current of 50 mA. As a result of this small value, the system responded slowly to large temperature changes.<sup>10</sup> The resolution of the output current was set by the 1 mV resolution of the D-A converter and the fine setting of the voltage divider, yielding an output current sensitivity of 1  $\mu$ A.

The temperature sensitivity was set by the RTD, Wheatstone bridge and multimeter. The 2000  $\Omega$  platinum RTD has a temperature coefficient of

$$k_T = 0.00385 * 2000\Omega / ^\circ C = 7.7 \Omega / ^\circ C. \quad (4.9)$$

---

<sup>10</sup>Most measurements were made over a relatively small temperature range; increasing the range, although possible, was not necessary.

Wire-wound resistors were used in the Wheatstone bridge, as they have lower noise than ceramic resistors. The temperature coefficient of the precision wire-wound resistors [108] was 5 ppm, i.e.  $10 \text{ m}\Omega / ^\circ\text{C}$ . A temperature stability better than  $0.1^\circ\text{C}$ , was achieved simply by placing the circuit in a large styrofoam box insulated on the inside with foam. This translates to a better-than-1 m $\Omega$  stability of the bridge resistors.<sup>11</sup> A 1 m $\Omega$  resistance stability translates to a temperature stability

$$\begin{aligned} T_{stab} &= \frac{1 \text{ m}\Omega}{k_T} \\ &= 0.13\text{mK} \end{aligned} \tag{4.10}$$

Other contributions to noise in the temperature control include electronic noise and read-noise in the multimeters. The electronic noise in the bridge circuit was primarily due to electromagnetic interference. Shielding the circuit by placing it in a metal box and grounding the box removed most of this noise. Read noise will always be an intrinsic problem, and one has to trade off between speed of reading and the noise in the reading. It turned out that averaging the voltmeter readings over 10 cycles of mains frequency was adequate for our purposes.

#### 4.4.2 Software

##### PID control

The control algorithm receives an input signal that is proportional to the signal from the temperature probe, calculates the error signal by subtracting the measured signal from the target value, and then calculates the value of current to supply to the heater/cooler to maintain or reach the target value. The algorithm typically used to achieve this is known as the PID algorithm (see Ref. [109], p. 280), and the controller a PID (or three-term) controller.

The proportional term produces a control signal  $u(t)$  that is proportional to the error signal  $e(t) = T_{set} - T(t)$ , where  $T_{set}$  is the desired temperature or set point and  $T(t)$  is the

---

<sup>11</sup>In general, a more elegant way to control the temperature of the resistance bridges is to place it inside the sample whose temperature is being controlled. The concern in this experiment was that the changing current through the circuit as temperature changes would interact with the applied external magnetic field.

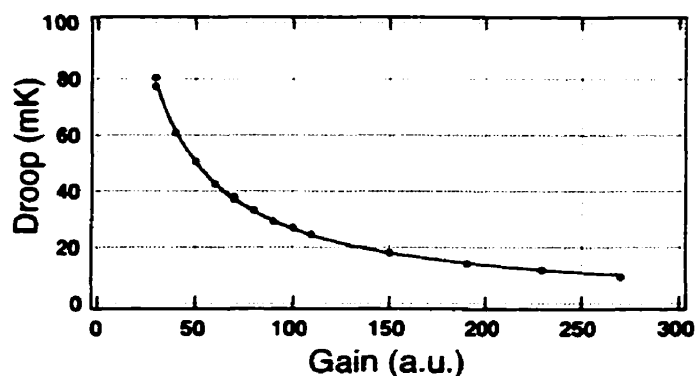


Figure 4.8: Measurement of proportional droop in the temperature control system (see Fig. 4.9) described in 4.4.1.

actual temperature at time  $t$ . The control signal is then

$$u(t) = P e(t), \quad (4.11)$$

where  $P$  is the proportional gain. A proportional ( $P$ ) temperature-controller settles to a steady-state operating temperature that is off from the target temperature by a value that is a function of the gain; this is known as “proportional” droop (see Fig. 4.8). A high gain minimises droop, but it also makes the controller less stable; for high-enough gain the system oscillates.<sup>12</sup> The integral term sums the error signal up to a cutoff. That is

$$u(t) = I \int_{t-\tau}^t e(t) dt, \quad (4.13)$$

where  $I$  is the integral gain. In a PID controller, its purpose is to make the long-term output equal to the set point and avoid the “proportional” droop. Although this term successfully eliminates steady-state error, it does so at the expense of stability. This stability can be

<sup>12</sup>The droop is related to the gain simply, because the steady-state error signal corresponds to a steady state final temperature  $kT = P e_{\text{steady-state}}$ . Expressing this in terms of the error signal and the (fixed) target temperature  $T_{\text{set}}$ , one expects that the steady-state error signal for a given gain follows

$$e_{\text{steady-state}} = T_{\text{set}} / (1 + P/k) \quad (4.12)$$

The droop in Fig. 4.8 is measured in  $\mu\text{V}$  and converted to mK by calibrating the bridge voltage against an RTD. As shown, the droop does indeed fit the functional form  $a/(b + P)$ , with  $a = 2810 \pm 40\text{mK}$  and  $b = 5.7 \pm 0.6$ . Thus, in this case, the target temperature was roughly  $2.8^\circ\text{C}$  above that set by the water baths.

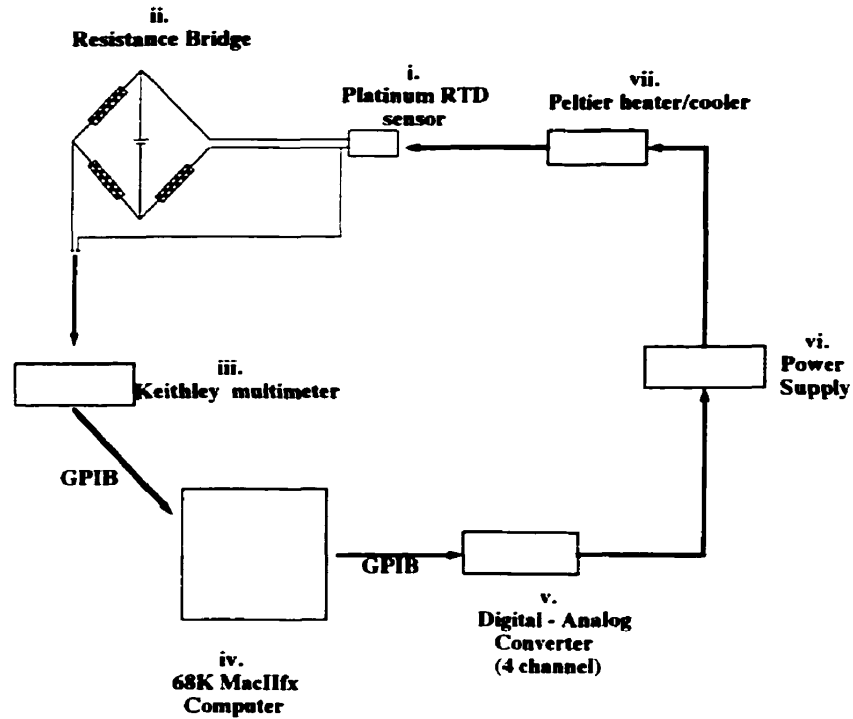


Figure 4.9: Schematic of temperature control system.

improved by reducing the gain, at the expense of response speed. If the response is too slow, then the differential term can be added; it speeds up the response to a sudden change in error signal (again at the expense of stability, this time to high-frequency fluctuations).

$$u(t) = D \frac{de(t)}{dt}, \quad (4.14)$$

where  $D$  is the derivative gain.

Both the integral and derivative terms have characteristic time-scales defined, respectively, by

$$\begin{aligned} \tau_I &= \frac{P}{I} \\ \tau_D &= \frac{D}{P} \end{aligned} \quad (4.15)$$

### Tuning the Algorithm

First, one tunes a  $P$  controller until the onset of continuous oscillations. The critical gain  $P_c$  and the period of the oscillations  $\tau$  determine the settings for PID control. A simple scheme, known as the Ziegler-Nichols scheme (see Ref. [109]) is useful for coarse tuning of the PID controller. According to this scheme, one simply sets:

$$\begin{aligned} P &= 0.6P_c \\ \tau_I &= 0.5\tau \\ \tau_D &= 0.125\tau. \end{aligned} \tag{4.16}$$

Given this as a starting point, the proportional gain can then be varied to suit the requirements of the system: in our case, the settings with the Ziegler-Nichols scheme were unstable (perhaps because the two temperature controllers in the system were coupled), and the proportional gain was thus lowered. Typical parameter values were  $P_c = 60$ ,  $P = 20$ ,  $\tau = 30$  sec,  $\tau_I = 0.5\tau$ , and  $\tau_D = 0.125\tau$ . In practice, the system had more than one time constant. There was a slower time constant ( $\approx 6$  minutes) associated with the coupling of the two temperature controllers; this was a small perturbation and treated as such.

#### 4.4.3 A Summary of the Temperature Control System

The primary aim of the technique developed in this thesis is to image an NA interface, with the best possible resolution. Although this entails a combination of optical and temperature resolution, the limiting factor in fact comes from temperature-related effects.

#### The Temperature Control Achieved

A time-series of the temperature control for the top heater is shown in Fig. 4.10. The temperature control achieved by this system had a typical peak-to-peak value of 0.2 mK and a r.m.s value of 0.1 mK over 10 minutes. The important point, however, is that the sample blocks act as a low-pass filter for the short-term oscillations, and the actual NA interface is stable to within one pixel. As a result it was not necessary to remove the short-term oscillations in the time-series. The starting temperature in this time-series is fairly close to the target temperature. When the starting temperature is a few degrees away, the controller takes a fairly long time to reach the target temperature. As a result, the control

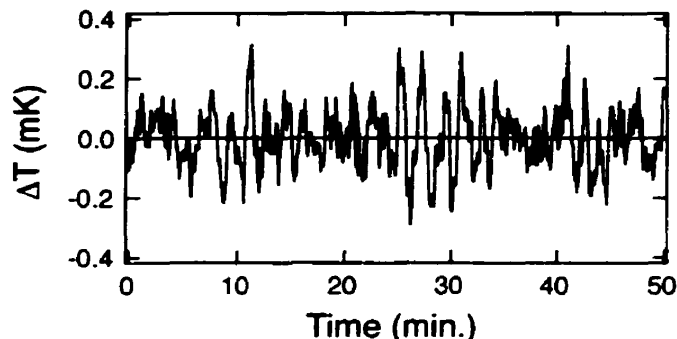


Figure 4.10: Time-series of temperature (calculated from conversion and calibration of the bridge voltage) of top channel of the temperature-control system.

algorithm was typically operated in proportional mode for a transient time, which brought the temperature close to the target value, before switching to PID mode.

#### 4.4.4 Applied Temperature Gradient

The applied temperature difference was varied from  $0.1^{\circ}\text{C}$  to  $1.0^{\circ}\text{C}$  across the top and bottom of the sample (i.e., over 15 mm). This implies a gradient across the field of view (of extent  $\sim 1.5$  mm) from 10 mK to 0.1 mK / pixel.

#### 4.4.5 Unwanted Temperature Gradients

Despite the symmetric design of the system, we found that there were residual uncontrolled temperature gradients. These gradients, in the plane perpendicular to the intended gradient (the vertical direction in Fig. 4.7), are easy to detect. One horizontal direction (the one that is in the plane of the paper in Fig. 4.7) results in a tilt of the interface, while the other (the one that is out of the plane of the paper in Fig. 4.7) is in the thickness direction and smears out the interface, giving poor contrast between the nematic and smectic-A phases.<sup>13</sup> As discussed in the beginning of this chapter, we can resolve spatially variations in the plane of the substrate, but we average over variations in the thickness direction. Thus, a temperature gradient along this direction directly degrades experimental resolution. The primary limit to interface resolution is due to unwanted temperature gradients across the

<sup>13</sup>Residual interface tilt is determined and accounted for in the fitting, by convolving a power law with a linear gradient—see Chapter 6.

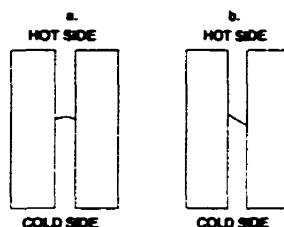


Figure 4.11: Two causes of interface smearing: (a) meniscus at glass surface and (b) lateral temperature gradient.

sample thickness. In principle, there can also be meniscus effects. These two effects are schematically illustrated in Fig. 4.11.

As discussed in Section 4.3, the largest source of heat loss was through the windows. Because the centre of the sample was separated from the copper blocks by 1 cm of glass, there was a noticeable effect of the environment on the temperature at the edge of the sample. This was clearly seen in the shape of the interface, which typically was flat in the centre but curved at the edge. Note that heat loss itself is not a serious concern; asymmetries in heat transfer are. There are two types of asymmetry that could cause these uncontrolled gradients:

1. Relatively large asymmetries in thermal conduction, arising from mechanical contact problems between any two of the several surfaces comprising the sample sandwich. By tightening on adjusting screws and using a bright lamp, obvious gaps in the contacts were eliminated.
2. Smaller asymmetries, which can be amplified by unwanted, but not completely avoidable thermal convection. To minimise convection, the inner walls of the hot-stage were lined with  $\frac{1}{2}$ -inch thick polyurethane foam.

## 4.5 Sample Preparation

The design of the sample hot stage, described above, was such that we would have control over the direction of the temperature gradient. The liquid crystal itself is sandwiched, either between glass cubes (see Section 4.2.1) or between glass slides. The glass cubes are preferable (but expensive) since we can then make thermal contact to the sides of the cubes.

The cubes were  $15\text{ mm} \times 15\text{ mm} \times 12.7\text{ mm}$  in dimension and had a surface flatness better than  $\lambda/8$ . The two cubes were glued together without spacers; the spacing was controlled and the pieces glued with the apparatus described in 4.5.3.

#### 4.5.1 Glass cleaning

The glass-cleaning process is essential for ensuring that the surface anchoring be of good quality. The glass is placed in a quartz crucible whose non-cylindrical shape is an advantage as it minimises the contact between the glass and the containing vessel. Since a pair of cubes (or slides) is needed to make a sample, and since the person preparing the sample coincidentally has two hands, the rinsing is done in pairs. All the rinsing is done in a plastic wash basin so that accidental dropping of the glass cube does not result in broken glass. The cubes are first rinsed in flowing cold tap water (the ions in tap water will dissolve some mineral impurities) for about 5 minutes. Then the glass crucibles are filled with soapy water. The soap used is 2% (by volume) Micro solution in tap water [110]. The crucibles are placed in an ultrasonic bath [111] at  $60^\circ\text{C}$  for 30 minutes. Then the cubes are rinsed thoroughly in distilled water; to be precise, 80 times each in flowing distilled water. (the choice of the number 80 was not completely arbitrary — it was roughly the time it took for the holding basin to overflow). Then they are rinsed in distilled, deionised water 20 times each. The entire process of rinsing with distilled and distilled, deionised water is done wearing latex gloves, so that by the end of the process, the gloves too have been thoroughly washed. (This is important as a later step involves holding the cubes by hand).

A qualitative check at this stage is whether the water completely wets the glass. If upon lifting the cubes/plates, from water, the film de-wets in less than 5 seconds, then the glass is not clean enough and needs a repeat of the soap-and-water cleaning.

Next, the crucibles are tilted to drain the water, and the water from the meniscus formed between the glass surfaces is wicked by capillary action using Kimwipes tissue [112]. Care is taken not to actually touch the glass with the tissue. Next, holding the cube by the edge, the remaining water is blown off with ionised [113] extra-dry nitrogen gas. The ions neutralise static surface charge, allowing dust to be blown away. The glass cubes are then placed in an oven at  $\approx 100^\circ\text{C}$  for roughly 15 to 30 minutes to dry. Any hitch in this process, of course, means starting over.

### 4.5.2 Surface Treatment of the Glass Cubes or Slides

The orientational order in the nematic phase spontaneously breaks the symmetry of the isotropic phase; in practice, the direction picked is set by the boundary conditions. By carefully producing very homogeneous boundary conditions, one can prepare uniformly oriented domains, the liquid-crystalline equivalent of a single crystal. The alignment required in the experiments done in this thesis required unidirectional planar alignment. Two methods were used to obtain planar alignment, both successful but each with its own advantages.

#### SiO Evaporation

The preferred method is based on the shadowing instability caused by oblique-angle deposition [114, 115]. SiO is evaporated onto the glass cube at an incidence angle of  $30^\circ$ . The vacuum evaporator [116] is first pumped down to  $\approx 2 \times 10^{-6}$  torr before evaporating the SiO. The current is slowly increased from 0 to 260 A. After each increase in current, enough time is allowed to allow the pressure to equilibrate before any further increase. All this is done with the shutter closed, shielding the sample. The SiO source [117] is baffled to prevent spitting out of solid SiO, which leads to "pinholes" in the anchoring. The SiO used is obtained in the form of pellets [118], roughly a few mm in extent. The actual deposition is done at a current of 260 A, with the shutter open for 10 seconds. The shadowing instability causes ridges to be formed along the axis formed by the intersection of the incident beam and the glass surface. The conjecture is that liquid crystal molecules prefer to align parallel to the ridges than across them (which would increase the elastic energy) [114]. After evaporation, the SiO coating is annealed by placing the glass in a hot-air convection oven [119] for two hours at  $60^\circ\text{C}$  (this temperature is chosen to be well above the maximum temperature used in the experiment).

#### Rubbed Polyimide Alignment

The other method used was the rubbed-polymer-coating which is used in commercial liquid-crystal cells. The clean glass cubes (or slides) were placed in an apparatus designed to unidirectionally submerge and remove the cube from a beaker filled with a solution of polyimide precursor in the solvent cyclopentanone [120]. The rate of withdrawal is  $\approx 0.2$  mm/sec.

The apparatus was hand operated and geared so as to allow for slow pulling of the cube

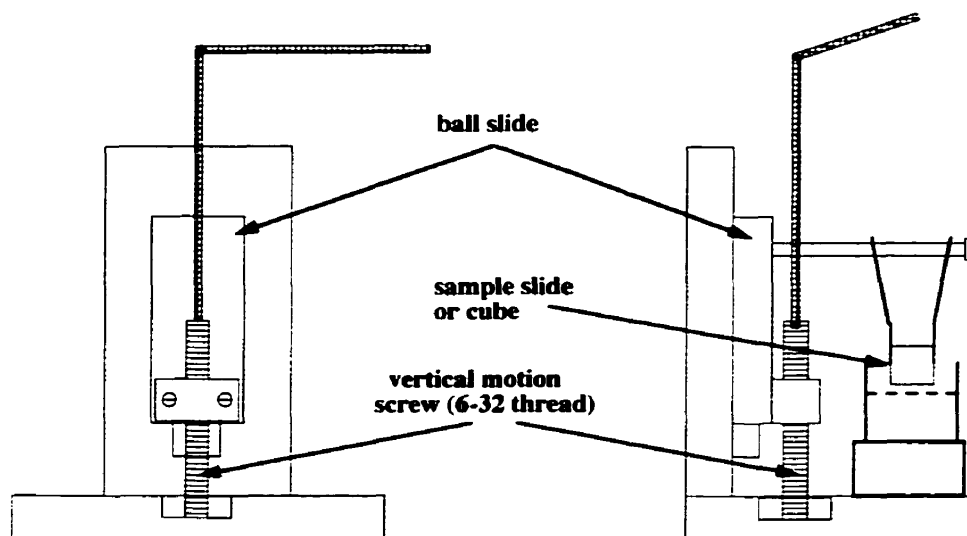


Figure 4.12: Apparatus for unidirectionally dip-coating glass with a polyimide-precursor solution. (a) Front view. (b) Side view showing glass and beaker with polyimide solution.

out of the solvent (see Fig. 4.12). This provided a directionality that improved the anchoring [121] — it was certainly superior to spin-coating the polyimide precursor on. It is likely that the directional flow helps orient the molecules. The glass was then baked at  $220^{\circ}\text{C}$  for two hours. The cubes were then placed in another jig that was designed to position the cubes for unidirectional rubbing in the same direction as the pulling. The rubbing was done with a steel rod inside tygon tubing, covered with a 5mm layer of raw cotton, which in turn was covered by lens tissue doubled by folding once. The rod was mounted on a ball-slide to facilitate a uniform rubbing motion. The force used to rub the glass was not measured. With the 1 mm thick glass slides, good anchoring correlated very well with rubbing that was hard enough to produce a squeaking sound [121] during rubbing.<sup>14</sup> For the thicker glass cubes, this sound was not heard (as it probably comes from the vibrations of the thin slide), but a rubbing force that was hard enough to produce a squeaking sound in the 1 mm thick glass slides also produced a good anchoring in the glass cubes. Any remnants of cotton or dust on the cubes were blown away with ionised nitrogen.

<sup>14</sup>A rough estimate of the force per unit area is 100 KPa. However, the squeaking sound is likely a more valuable indicator than any quantitative estimates. It is typical that the correct rubbing technique involves much trial-and-error to find. See Ref. [122] for a review on anchoring and anchoring techniques.

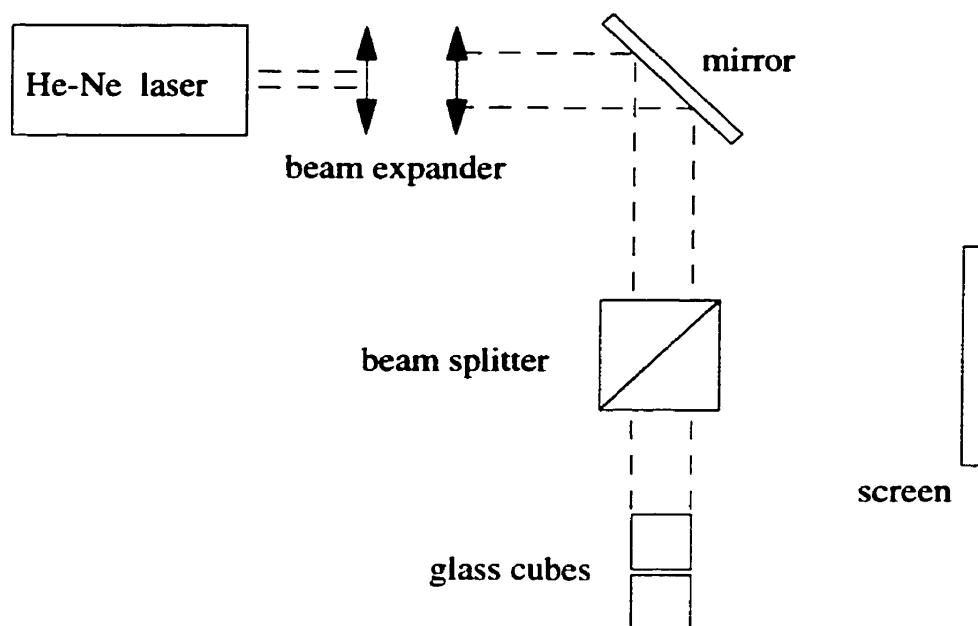


Figure 4.13: Interferometric set-up to measure and correct thickness gradients, to  $0.5 \mu\text{m}$  over 1 cm. It was also able to set the thickness to with  $\pm 2 \mu\text{m}$  absolute.

### Comparison of Methods

The quality of the rubbed-polymer alignment was good; however, there were scratches in random directions that were unavoidable from the rubbing process. However there were far fewer scratches near the centre of the sample, where the rubbing velocity would be the most uniform.

In contrast, the SiO anchoring was almost completely featureless. However, the anchoring strength was smaller than that for polyimide, and the anchoring degraded gradually, but irreversibly every time the sample was cooled to a couple of degrees below the NA transition.

All the data taken with samples prepared with rubbed-polymer-coating anchoring was done during the period in which the SFU physics-department vacuum-evaporator was out of service.

### 4.5.3 Thickness adjustment and measurement

In polarized microscopy in an anisotropic medium, the path-length mismatch between ordinary and extraordinary rays depends linearly on the thickness of the sample. If one requires a homogeneous sample, then the thickness gradient across the sample should be small, preferably on the order of the wavelength of light, or better. To control this thickness, we mounted the two cubes independently. The top cube was mounted on the shaft of a microscope's vertical-adjustment stage, where the vertical motion (and hence the sample thickness could be controlled to within  $1\ \mu\text{m}$ . The bottom cube was mounted on a five-axis stage (made by joining two translation stages, a rotation stage, and a two-axis tilt positioner) that allowed variation of all the remaining degrees of freedom. This was necessary because the two cubes not only had to be parallel to each other, the sides had to match up as well so as to make good thermal contact with the copper blocks that thermally coupled the sample to the heaters. We used a laser interferometer (see Fig. 4.13) to monitor the gradient in thickness as shown. The light was spatially filtered and then collimated into a beam about 2 cm in diameter. The light was directed normal to one of the surfaces, and the other surface was adjusted to minimize the number of fringes in the interference pattern. The beam-splitter surfaces were oriented so that none of its surfaces was exactly perpendicular or parallel to the sample cube surfaces; hence its reflected beams did not coincide with the sample cubes. Note that there are actually 4 reflecting surfaces—the parallelism of the opposite surfaces of the cubes was good enough (better than  $\lambda/2$ ) that there is only 1 set of fringes corresponding to the relative parallelism of the two cubes. A typical sample had an average thickness of  $30\ \mu\text{m}$  and a linear variation of about  $0.5\ \mu\text{m}$  over a one- $\text{cm}^2$  surface.

### 4.5.4 Polishing of the Copper Surfaces

The surfaces of the copper blocks in the sample-cell sandwich was machined flat and then polished flat using wet "800 A" diamond-grit sand paper that was mounted on a piece of float glass. The main concern at this stage was to avoid introducing any large-scale waviness; a secondary concern was surface smoothness.

#### 4.5.5 Glue

The glass cubes were glued in place with a viscous, UV-curing adhesive [123]. The thickness adjustment was monitored during the curing process in order to ensure homogeneity after the glue hardened. Two opposite surfaces were then glued to copper blocks, with a less-viscous adhesive [124]. Great care was taken to avoid air bubbles between the contact surfaces, so as to ensure uniformity of thermal contact.

#### 4.5.6 Liquid crystal purification and filling

The liquid crystal materials used (8CB and its mixtures with 10CB) are commercially available much purer than usually possible for organic materials. Both 8CB and 10CB are chemically very stable with, consequently, well-characterised materials parameters (included in Appendix A. The liquid crystal was de-gassed with a mechanical pump at  $\approx 50^\circ\text{C}$  and  $\approx 100$  mTorr for 15 minutes to remove water and other solvents. The samples were filled by capillary action: a small amount of liquid crystal was placed at the edge of the gap and left to fill the gap. The filling was done in the direction of the anchoring and in the isotropic phase in order not to disrupt the anchoring.

### 4.6 Preparation of Liquid Crystal Mixtures

In preparing mixtures of 8CB and 10CB, a portion of 8CB was put in a glass vial. The mass of 8CB transferred was hard to control as it is a viscous smectic liquid crystal at room temperature. After measuring the mass of 8CB added, a calculated amount of 10CB was then added to the same vial. If the required mole fraction was  $x$ , then

$$x = \frac{(\text{mole fraction})_{10}}{(\text{mole fraction})_8 + (\text{mole fraction})_{10}} \quad (4.17)$$

Since the molecular weight of 8CB is 291 and that of 10CB 319, in terms of masses, the mass of 10CB required is determined by

$$m_{10} = \frac{319}{291} \left( \frac{x}{1-x} \right) m_8. \quad (4.18)$$

A teflon stir bar was then put into the vial and the mixture stirred at  $50^\circ\text{C}$  for 30 minutes. This is above the IN transition, so the liquid is isotropic and not very viscous, and therefore

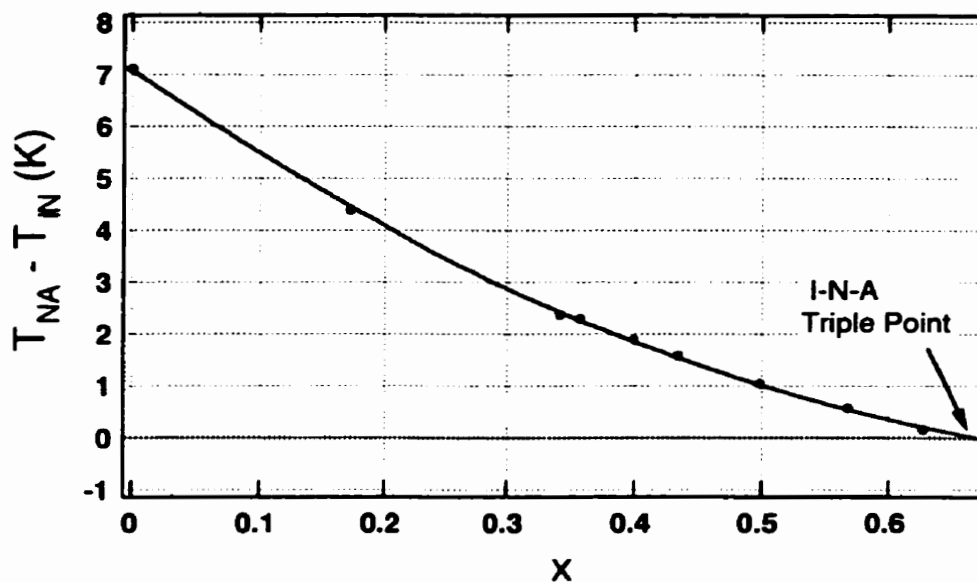


Figure 4.14:  $T_{NA} - T_{NI}$  calculated from the phase diagram in Fig. A.2 as a function of mixture concentration. The dependence is well fit by a second-degree polynomial, which is thereafter used as a calibration curve for mixture preparation. From the fit,  $T_{NA} - T_{NI} = a + bx + cx^2$ , with  $a = 7.07 \pm 0.05$ ,  $b = -16.8 \pm 0.3$ , and  $c = 9.3 \pm 0.5$ . The triple point is at  $0.65 \pm 0.01$ .

mixes readily. The vial was placed inside a doughnut-shaped aluminium block on a hot plate in order to heat the entire vial uniformly. The mixture was then de-gassed as for the pure 8CB.

The binary 8CB-10CB liquid crystal mixture has a nematic range that is a function of the concentration (mole fraction of 10CB in 8CB). The transition temperatures  $T_{NI}$  and  $T_{NA}$  as a function of concentration have been established by Marynissen *et al.* [46] and used in a previous work by Tamblyn *et al.* . For each data point in the phase diagram (Fig. A.2), we can calculate the nematic range  $T_{NA} - T_{NI}$ . This is plotted in Fig. 4.14; the data points are satisfactorily fit by a quadratic polynomial.<sup>15</sup> We used this curve to characterise the prepared mixtures; we measure the nematic range ( $T_{NA} - T_{NI}$ ) and use the mixture calibration curve to arrive at a value for the concentration of the 10CB. This value, and not the value calculated from the masses using Eq. 4.17 (which is usually close)

<sup>15</sup>Note that the fit of  $T_{IN}$  or  $T_{NA}$  vs.  $x$  to a polynomial was not particularly good. The fit to  $T_{IN} - T_{NA}$  vs.  $x$  was far better.

is used; we thus had an independent and reliable measure of the actual concentration of the mixtures.

## 4.7 Summary

We have designed a combined temperature-control system and imaging system that can give us 0.1 mK temperature stability and at the same time allows us to use bright-field microscopy for a sensitive phase-transition experiment. The experimental apparatus and the sample-preparation techniques that we developed were also described in this chapter. Now we are ready to use this system to characterise the technique of intensity fluctuation microscopy, which is the subject of the following chapter.

## Chapter 5

# INTENSITY FLUCTUATION MICROSCOPY: CALIBRATIONS

### 5.1 Characterising the Intensity Fluctuations

#### 5.1.1 Introduction

Traditionally, fluctuations in condensed-matter systems have been probed by scattering methods. But in the last few years, different groups have used real-space imaging to study intensity fluctuations in soft condensed systems [125, 126, 127, 128]. As well, a new method of light-scattering using a CCD camera [129] has been explored. The advent of digital CCD cameras and the rapid increase in image-capture rates ensures that quantitative imaging techniques such as the one developed in this thesis will be used more in the years to come. In this chapter, we describe and characterise our technique and its nontrivial dependence on parameters that are routinely varied during the experiment: shutter speeds, CCD pixel binning, light intensity, the angle of the sample axis with respect to the polarisers, and the thickness of the birefringent sample.

#### 5.1.2 The signal and the noise

Nematic director fluctuations are soft modes, arising from the spontaneous symmetry breaking that takes place when the isotropic liquid condenses into an orientationally ordered nematic. The uniaxial order in the nematic influences macroscopic thermal, optical and



Figure 5.1: A “difference” image showing the NA interface. The images  $I_1$  and  $I_2$  in the difference image are separated by a time interval of 1 sec. to ensure that they are statistically independent. Shown is a  $450 \times 200$  pixel area of the image, corresponding to an area of  $\approx 0.6 \times 0.25$ mm area in a sample of 8CB. The lateral gradient  $dT/dx \approx 1^\circ\text{C}/\text{mm}$ .

elastic properties in the nematic. The fluctuations of the director induces local fluctuations in the anisotropic nematic dielectric tensor,  $\bar{\epsilon}$ . The goal of our technique is to image director fluctuations by placing the sample between crossed polarisers and measuring intensity fluctuations. The light incident on the sample is plane-polarised. The locally fluctuating director gives rise to local fluctuations in the polarisation state of the transmitted light; in turn, when the transmitted light is “analysed” by the second polariser (which is “crossed,” i.e. placed so that its transmission axis is perpendicular with respect to that of the first polariser), what one sees is fluctuations in the light intensity. To make quantitative observations, one records the image via a CCD camera on a computer and analyses the statistics of the light-intensity distribution with image-processing software [130, 94, 95]. There are, however, complications in the imaging process because of intensity fluctuations in CCD microscopy that are intrinsic to the imaging process. As they are unwanted, they are collectively called noise, but they arise from different sources. We discuss in this section the characterisation of the signal and the noise.

### The signal

The data in this thesis is obtained in the form of snapshots of a field of view of the liquid crystal sample, with the focus adjusted to be roughly in the middle of the sample, roughly halfway between the glass plates. Subtracting two successive images gives us a “difference image”

$$\Delta(x, y) = I_1(x, y) - I_2(x, y) \quad (5.1)$$

which is a crude measure of the fluctuations in intensity in the elapsed time (Here  $I_1(x, y)$  and  $I_2(x, y)$  are the two “instantaneous” images.) It turns out to be more convenient to subtract the difference of two “instantaneous” images than to measure the deviation from the average intensity; we will show shortly that it yields the same information. The fluctuations in intensity can also be seen qualitatively in Fig. 5.1, which shows the fluctuations in a liquid-crystal sample between crossed polarisers. The location of the interface is apparent. Provided that the relaxation times in the nematic are smaller than the elapsed time between two images, the intensity at any given point (“pixel”) is uncorrelated in time, i.e. successive snapshots are uncorrelated. We may construct our “ensemble average” over the 1 million pixels in the difference image, rather than averaging over time. One can see that the director fluctuations in the nematic are correlated over a length scale of a few pixels. In this sample, the sample thickness is on the order of  $30 \mu\text{m}$ , while each pixel corresponds to  $\approx 2 \mu\text{m}$ . The nematic correlations are fundamentally infinite ranged; however, the system size sets a natural limit on the correlation length. Thus, because the thickness dimension is very small, the correlation length is set by the sample thickness and is thus on the order of 10 pixels.

Next, we construct a histogram of the distribution of intensity differences. Shown in Fig. 5.2 is a relatively small  $100 \times 100$  square pixel area in the nematic at a temperature close to  $T_{NA}$ . The distribution of intensity differences in the nematic is very well fit by a Gaussian probability distribution. The width of this Gaussian probability distribution is also equivalent to the variance of the distribution and can be characterised by  $\hat{\zeta}$ , which we refer to here as the *raw* variance:

$$\hat{\zeta} = \left\langle \frac{[I_1(x, y) - I_2(x, y)]^2}{2} \right\rangle, \quad (5.2)$$

where  $\langle \rangle$  refers to a spatial average over pixels. The variance defined above is equivalent to the variance of the *deviation* from the average.

$$\langle (\delta I_1(x, y))^2 \rangle \equiv \langle (I_1(x, y) - \overline{I(x, y)})^2 \rangle, \quad (5.3)$$

where  $\overline{I(x, y)}$  is a time average, which in principle, can be constructed by averaging several successive images. The variance of the deviation from the average can, in principle, be related to director-director correlation functions. The advantage of the quantity in Eq. 5.2

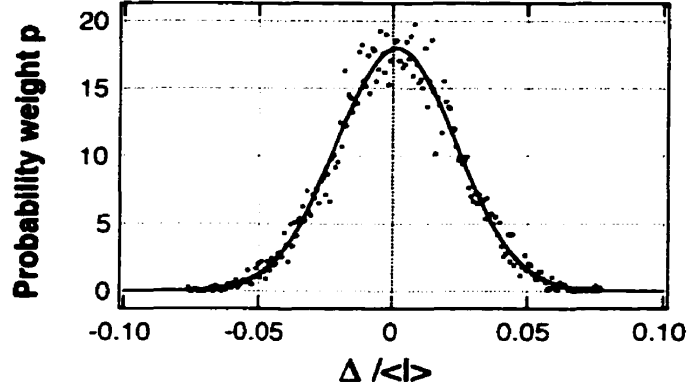


Figure 5.2: Histogram of the intensity distribution of a  $100 \times 100$  square-pixel region at  $T - T_{NA} \approx 0.1K$ .  $\Delta = I_1 - I_2$ , and  $\langle I \rangle$  is the average intensity of an instantaneous image. The probability weight is normalised so as to give the distribution unit area.

is that it can be constructed from just two images, without the need to construct a long-time average. This is invaluable when studying thermodynamic properties at a nematic-smectic-A (NA) interface. It takes roughly 20 seconds to capture 16 independent images, and one is therefore very susceptible to temperature drifts in this time. By capturing just two images, we reduce the temperature drift during the measurements simply by shortening the period of the measurements to roughly two seconds.

Note that, in all that follows,  $\overline{\quad}$  refers to a time average while  $\langle \quad \rangle$  refers to a spatial average. We write

$$\begin{aligned} \hat{\zeta} &\equiv \frac{1}{2} \langle (I_1(x, y) - \overline{I(x, y)} - I_2(x, y) + \overline{I(x, y)})^2 \rangle \\ &= \frac{1}{2} \langle (\delta I_1(x, y) - \delta I_2(x, y))^2 \rangle \end{aligned} \quad (5.4)$$

$$= \frac{1}{2} \left\{ \langle (\delta I_1(x, y))^2 \rangle + \langle (\delta I_2(x, y))^2 \rangle - 2 \langle \delta I_1(x, y) \delta I_2(x, y) \rangle \right\} \quad (5.5)$$

The first and second term in Eq. 5.5 are identical since, statistically, there is no distinction between  $I_1$  and  $I_2$ . Moreover, since the functions  $\delta I_1(x, y)$  and  $\delta I_2(x, y)$  are uncorrelated, the third term is negligibly small. Thus,

$$\hat{\zeta} \equiv \left\langle \frac{(I_1(x, y) - I_2(x, y))^2}{2} \right\rangle = \langle (I_1(x, y) - \overline{I(x, y)})^2 \rangle. \quad (5.6)$$

### The noise

In addition to the intensity fluctuations due to director motion, there are fluctuations produced by the imaging process itself. A fundamental source of noise intrinsic to the CCD chip is termed *dark noise*. Dark noise is created by the existence of an electronic leakage current in the absence of incident light (for example, with the shutter closed). Dark noise is unimportant for bright-field imaging applications but becomes important for extremely low light levels. We ignore it here. Unlike dark noise, which originates in the imaging section, *read noise* originates in the output preamplifier of the CCD. Read noise increases with readout rate. Both read noise and dark noise increase with temperature. (See, for example, Ref. [131].)

The primary source of noise in bright-field imaging is *photoelectronic shot-noise*. This comes from the random counting statistics of photoelectrons generated at each detector (pixel). It is thus uncorrelated from one pixel to the next. Since a typical CCD camera has  $10^5$  to  $10^6$  pixels, one can very easily study the statistics of the shot-noise-generated intensity distribution. See Section 5.1.4, below.

### 5.1.3 Variances in the isotropic, nematic and smectic-A Phases

The isotropic phase has no measurable birefringence: an image of the isotropic phase between crossed polarisers is dark, and not different in intensity from a blank field.<sup>1</sup> In practice, the only way to distinguish a blank field from the isotropic phase is the existence of in-focus dust particles.

Deep in the nematic,  $\hat{\zeta}$  is large. It decreases as the NA transition temperature  $T_{NA}$  is approached. In the smectic-A phase it is much smaller; in fact,  $\hat{\zeta}$  is not noticeably higher than the shot-noise level (see Fig. 5.3). This is a bit surprising at first, because the splay elastic constant in the nematic does not diverge at the NA transition: the smectic bend mode (which corresponds to the splay mode in the nematic) should still contribute to the fluctuations. However, the unidirectional planar anchoring in thin samples tends to suppress

---

<sup>1</sup>Even close to the isotropic-nematic (IN) transition, no signal is observed by our method; in contrast light-scattering measurements reported in the literature find an increase in signal [132, 133]. Because the length scale of the measurement ( $\approx 1\ \mu\text{m}$ ) is much larger than the typical correlation length at the IN transition ( $\approx 10\ \text{nm}$ ), our method is not sensitive to these effects.

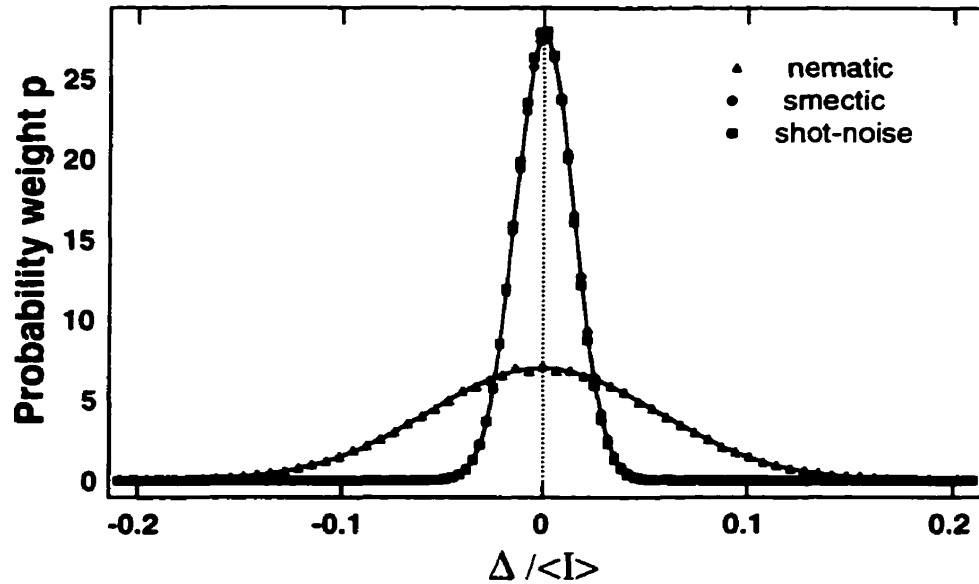


Figure 5.3: Probability distribution functions in the nematic and smectic-A phases, and in a blank field. The lines are gaussian fits. Note that the smectic level is indistinguishable from the shot-noise background measured in the blank-field image. Image is  $640 \times 480$  pixels.

the splay mode; as a result, this technique is more sensitive to the twist and bend modes, especially for thinner samples.

#### 5.1.4 Dependence of $\hat{\zeta}$ on the incident light intensity

In all the calibration data shown so far, the mean intensity was kept constant. It is desirable to understand the functional dependence of the signal and the noise on the average intensity. Once we know this, we can characterise our fluctuations in an intensity-independent way.

The intensity-dependence of the variance of intensity fluctuations is used as a standard test by camera manufacturers to test CCD characteristics [134]. In particular, it gives the zero-light offset of the CCD and the shot-noise inherent in imaging. The electronic amplifier in the CCD camera has a built-in electronic offset, to make low light-level signals more independent of electronic drifts. The shot noise measured by the camera in bright field is a measure of the number of photoelectrons being counted by the CCD and thus allows one to measure the number of electrons per pixel grey level.

When the relation between the angular fluctuations and the intensity fluctuations is

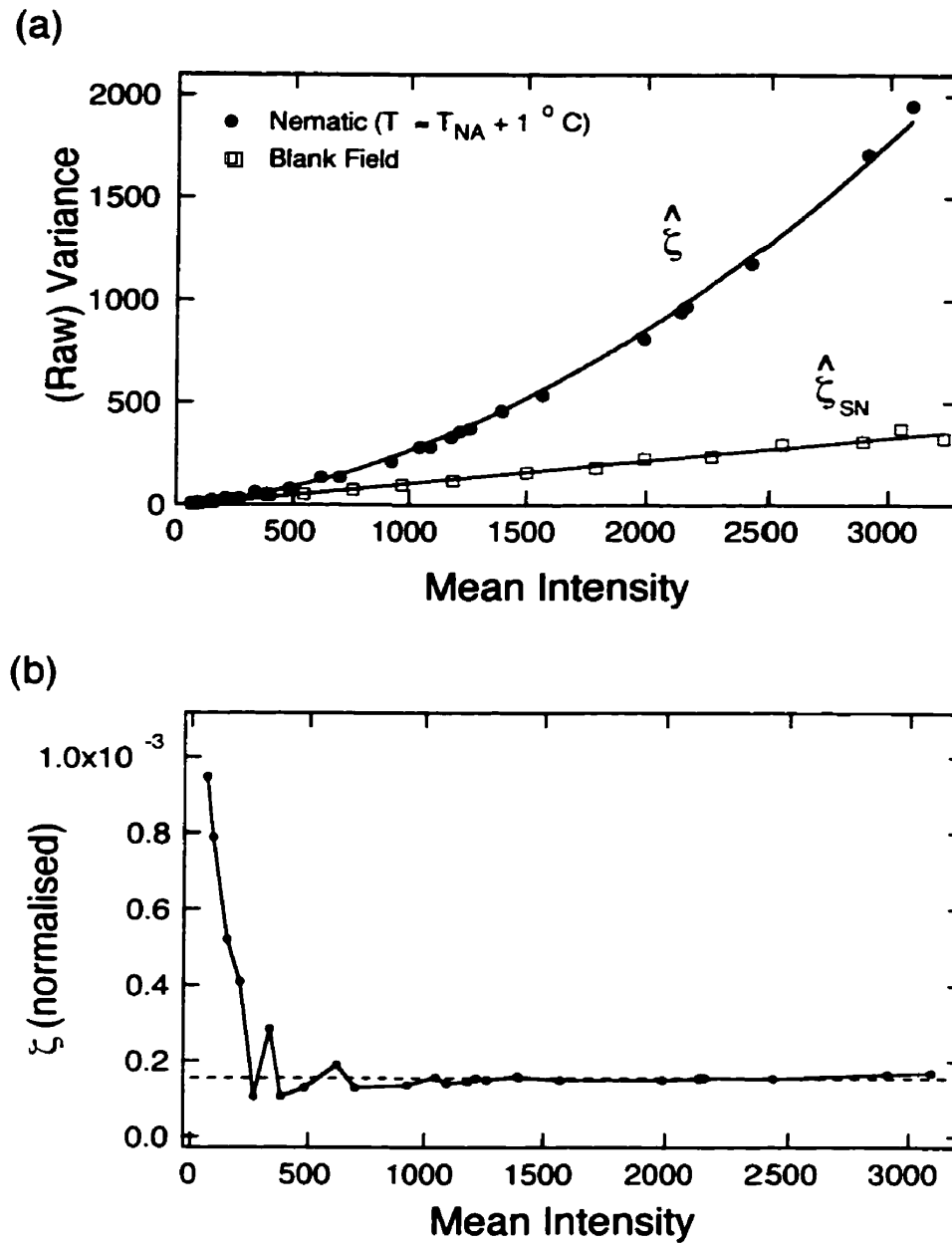


Figure 5.4: (a) The variance of the shot-noise  $\zeta_{SN}^2$  as a function of the mean intensity  $\langle I \rangle$  is linear, with a slope of  $0.111 \pm 0.003$  (this slope is a characteristic of the camera, in this case, a 12-bit digital CCD). The reciprocal of the slope gives the sensitivity,  $9.0 \pm 0.2$  photoelectrons/greylevel. The variance of the signal (top curve in (a)) is quadratic. (b) The normalised variance  $\zeta \equiv (\hat{\zeta} - \zeta_{SN}^2) / (\langle \bar{I} \rangle - I_{offset})^2$  is independent of mean intensity for intermediate and high light levels.

linear, one need not independently measure the incident light intensity as it is related to the average transmitted intensity by a constant scale factor. The average light intensity can be estimated by the average over the two frames captured, for each pixel: i.e.

$$\bar{I}(x, y) = \frac{I_1(x, y) + I_2(x, y)}{2}. \quad (5.7)$$

This average can of course be improved by collecting more images, at the expense of greater susceptibility to temperature drifts. One can use the fact that any illumination variance is long wavelength. Thus, one can construct an average from just two images by further averaging spatially over  $\simeq 10 \times 10$  pixels. This was found to be necessary only when the illumination intensity variation across the field-of-view was larger than 10%. When well-aligned, our optical system gave of 7-10 % intensity variation.

The shot-noise background, being purely a function of intensity, can be calibrated in a blank field with no liquid crystal sample, and the angle between the polariser and analyser varied to vary the transmitted light intensity. In Fig. 5.4, we show the variance of nematic and blank-field data as a function of the average transmitted intensity. The blank-field data in Fig. 5.4(a) is well fit by a straight line with a non-zero intercept for most of the range of intensities. The intercept of the blank-field curve places the zero-light offset at  $63.7 \pm 0.1$  grey levels. Hidden in this offset are the dark noise and read noise; the noise has a stated value of 16.0 electrons/(RMS), which corresponds to 1.8 grey levels.

The signal variance, on the other hand, is fit well by a polynomial to quadratic order. Note that the fit shown is *not* a best fit to 3 free parameters (constant, linear and quadratic coefficients) but a fit with the offset and linear term held at the shot-noise values. This *raw* signal variance has in it a shot-noise contribution as well. Since the signal variance and shot-noise variance are statistically independent, and since both distributions are Gaussian, we must subtract  $\hat{\zeta}_{SN}$  from  $\hat{\zeta}$  to isolate the signal variance. Note that the signal variance increases quadratically, while the shot-noise variance increases linearly with average intensity; hence the signal-to-noise ratio increases linearly with the average light intensity. The normalised variance  $\zeta$

$$\zeta = \frac{\hat{\zeta} - \hat{\zeta}_{SN}}{(\langle \bar{I} \rangle - I_{offset})^2}. \quad (5.8)$$

is then independent of the incident light intensity.<sup>2</sup> In Fig. 5.4(b), a plot of  $\zeta$  vs.  $\langle \bar{I} \rangle$  is

---

<sup>2</sup>This is true to lowest order. Higher-order effects do not respect this normalisation.

shown. It is seen that for a mean intensity above  $\approx 500$  grey levels,  $\zeta$  is independent of the light level. Actual measurements were done with  $\langle \bar{I} \rangle = 1000 - 3000$ .

### 5.1.5 Angle dependence in the nematic phase

In the previous section, we assumed that there was a linear relation between angular fluctuations of the director and the corresponding intensity fluctuations. In the linear approximation, one expects that the angle at which the mean intensity is the largest and smallest should be minima for the fluctuations; the fluctuations should be maximum where the mean intensity variation with angle is linear. A simple model for the behaviour of the fluctuations would be to treat the nematic as a fluctuating waveplate. The only effect of fluctuations, in this case, would be to give rise to in-plane angular variations; out-of-plane fluctuations are higher order and are therefore neglected. In this highly simplified approximation, the fluctuation variance

$$\hat{\zeta} \propto \left[ \frac{d\langle I \rangle}{d\theta} \right]^2 \quad (5.9)$$

where  $\langle I \rangle$  is the mean intensity and  $\theta$  is the angle between the sample optic axis and one of the polarisers. Plotted in Fig. 5.5 are the mean intensity and the raw variance (with the shot-noise subtracted) as a function of the angle  $\theta$ . Since the mean intensity Fig. 5.5(a) fits very well the expected form of

$$\langle I \rangle \propto \sin^2(2\theta), \quad (5.10)$$

one would expect in this linear approximation that

$$\hat{\zeta} \propto \sin^2(4\theta), \quad (5.11)$$

which is symmetric about a maximum at  $\theta = \pi/8 = 22.5^\circ$ , and zero at  $\theta = 0$  and  $\theta = \pi/4 = 45^\circ$ . In practice, however one sees (Fig. 5.5(b)) that it is asymmetric about  $\pi/8$ : in fact, another, *lower frequency* term is needed to fit the data! In 5.1.7, we argue that the lowest-order contributions arise because our optics capture rays over a finite range of angles. Varying the angle between the sample axis and the polariser changes the mean intensity and the intensity-fluctuation width simultaneously. To get a visual picture of the dependence of the normalised fluctuations on angle, we keep the transmitted light intensity fixed by adjusting the intensity of the incident beam. A sequence of intensity distributions

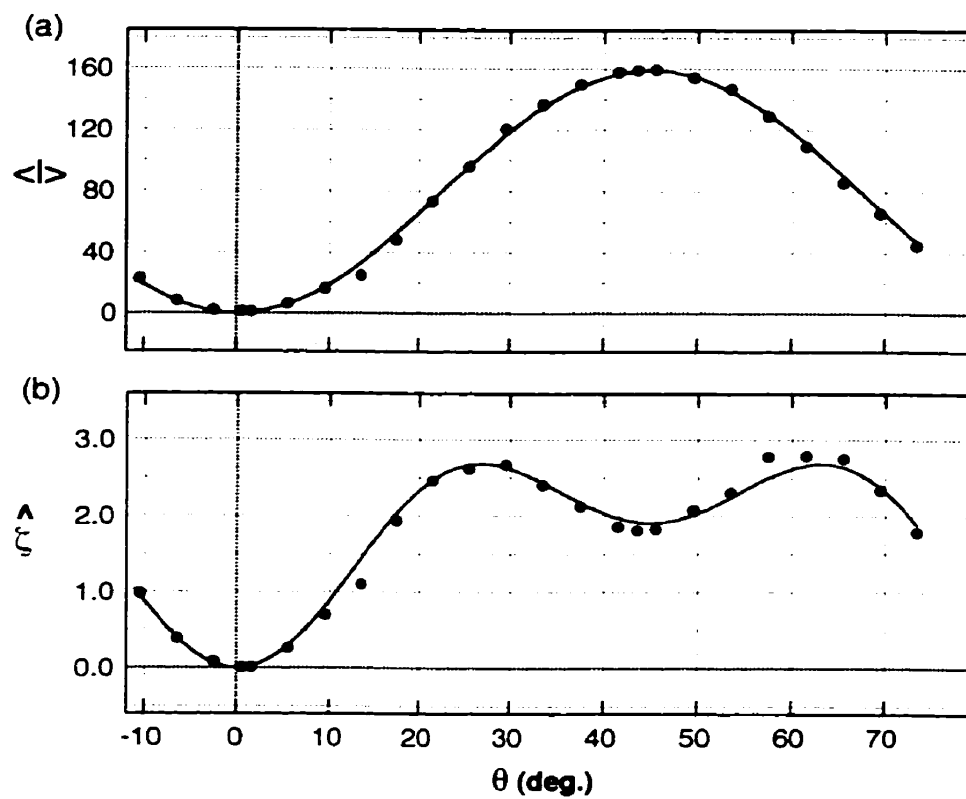


Figure 5.5: Mean intensity and variance as a function of  $\theta$ . (a) Mean Intensity is fit to  $a_1 \sin^2 2\theta$ , with  $a_1 = 158.6 \pm 0.8$ . (b) Raw Variance (shot-noise subtracted) is fit to  $a_2 \sin^2 4\theta + b_2 \sin^2 2\theta$ , with  $a_2 = 1.58 \pm 0.05$  and  $b_2 = 1.91 \pm 0.05$ .

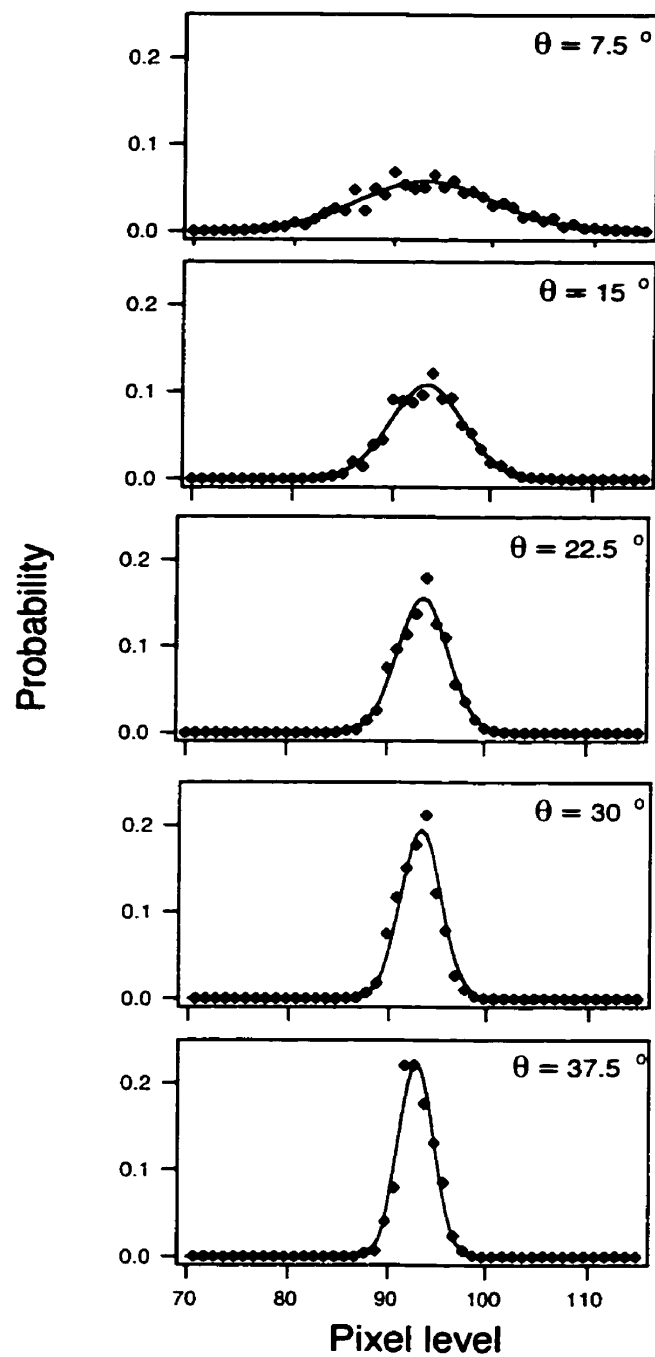


Figure 5.6: Intensity distributions (fit to Gaussians) as a function of  $\theta$ . The light source is adjusted to give constant  $\langle I \rangle$  as  $\theta$  is varied.

for different angles is shown in Fig. 5.6. In this case, the fluctuation width increased monotonically with decreasing angle. Thus the sensitivity to normalised fluctuations increases monotonically with decreasing angle. However, close to  $\theta = 0$ , dark noise and the discreteness of our measurement limit the resolution. Qualitatively, the angle that gives optimal signal-to-noise is close to  $10^\circ$ . However, this advantage is only valid so long as we are using the full dynamic range of the camera. That is, we must always increase the intensity of the light source to keep the transmitted beam intensity just below the amount that saturates the CCD pixels. It turns out that we are light-intensity limited at small angles and thus must operate in any case at larger angles.<sup>3</sup>

In spite of these complicated trade-offs, we encountered an easy solution to the choice of the angle of the sample axis with respect to the polarisers. The angle  $30^\circ$  is a maximum for the (un-normalised) fluctuations, and thus the angle at which the intensity fluctuations are linearly related to the director fluctuations. Since this is also an angle where the sensitivity is reasonable and where we are still light-limited, this is an acceptable solution within the limitations of the experiment.

### 5.1.6 Thickness dependence

So far, we have not worried about effects due to sample thickness. In this section, we first discuss the effects of sample thickness on intensity fluctuations. Next, we discuss their first-order optical effects, which we understand. Finally, we talk about residual, essentially second-order effects, which we only partially understand.

#### Director fluctuations

The sample's glass surfaces provide boundary conditions for the anchoring of the liquid crystals. Fluctuations of the director are strongly suppressed at the surfaces, while they reach their maximum value in the bulk, mid-way between the surfaces. (Fig. 5.7). To be in a regime where boundary effects are not important, one would have to use samples considerably thicker than the depth of field, which we estimated in Section 4.2.3 to be  $d_{tot} \approx 20 \mu\text{m}$ . However, there are other effects to consider and we will come back to the

---

<sup>3</sup>The arc lamp we use is (nearly) the brightest non-laser source available. It would be possible to use a laser source, but their coherence introduces other complications.

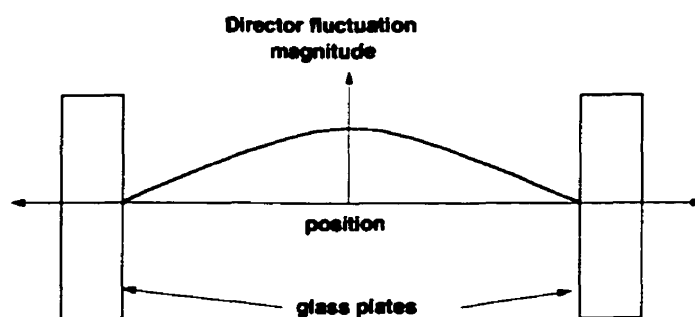


Figure 5.7: A schematic of the fluctuation profile across the thickness of the sample. The signal collected typically integrates over this profile.

issue of sample thickness at the conclusion of this section.

### Optical Effects

The thickness of the liquid crystal sample also introduces two non-ideal optical effects to the data. In Fig. 5.8, a schematic of a wedge sample is shown. The sample was prepared with two wire spacers  $12.5 \mu\text{m}$  and  $50 \mu\text{m}$  thick. With this sample, one can analyse the variance and mean intensity in strips along lines of equal thickness, in effect scanning as a function of thickness.

The mean intensity (Fig. 5.9(a)) oscillated with thickness. Successive maxima are spaced by a distance that corresponds to a thickness variation of  $\Delta d = 4.4 \mu\text{m}$ . This corresponds to an optical path length variation,

$$\delta p = \frac{2\pi \Delta d \Delta n}{\lambda_0} \equiv \pi \quad (5.12)$$

Thus

$$(\Delta n) = \frac{\lambda_0}{4(\Delta l)} = \frac{0.5 \mu\text{m}}{(2)(4.4 \mu\text{m})} \approx 0.12 \quad (5.13)$$

which is the same order of magnitude as the value  $\Delta n \approx 0.14$  expected from independent measurements of the refractive indices in 8CB by Karat *et al.* [135].

Second, there is multiple scattering. In the plot of variance vs. thickness, one notices (Fig. 5.10) that the peak-to-peak oscillation amplitude,  $\Delta \zeta_{\text{peak-peak}}$ , decreases with thickness. This suggests that multiple-scattering effects are important for thicker samples and implies that the sample thickness should be restricted to a value substantially less than  $50 \mu\text{m}$ .

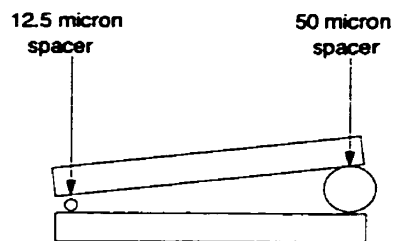


Figure 5.8: A schematic diagram of the wedge sample.

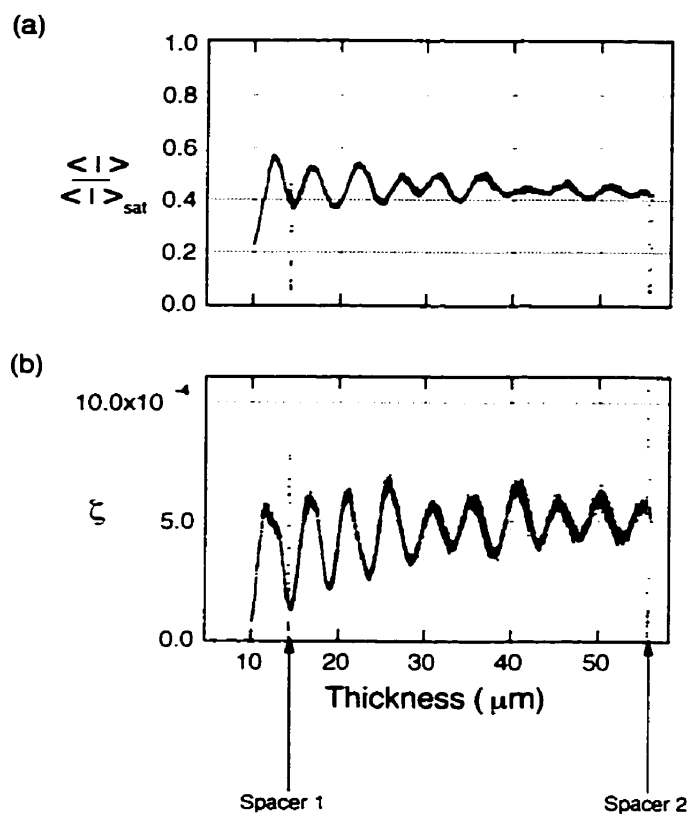


Figure 5.9: The thickness dependence of the mean intensity and the normalised fluctuations in the wedge sample. (a) Mean intensity, normalised to the saturation value of the CCD. (b) Normalised fluctuations.

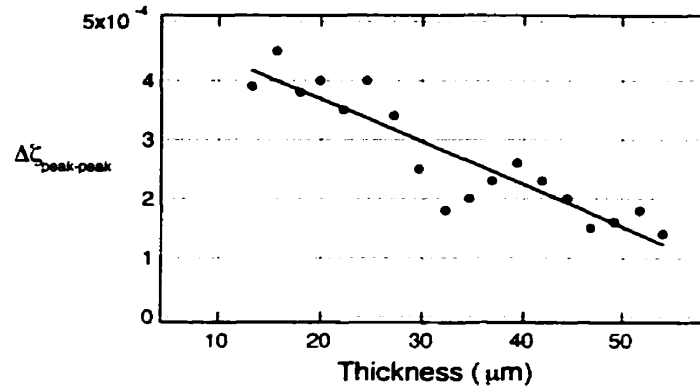


Figure 5.10: The peak-to-peak oscillation in the fluctuations,  $\Delta\zeta_{\text{peak-peak}}$ , gets progressively washed out with increasing thickness.

### Conclusion

There is a curious feature in Fig. 5.9(b). Here,  $\zeta$  is seen to be shifted *out of phase* with respect to the mean intensity  $\langle I \rangle$  in Fig. 5.9(a). This cannot be explained by the naive picture of the nematic as a uniformly fluctuating waveplate. This is discussed in the following section. We now come to the question of choosing an optimal sample-thickness, where there are different considerations:

- Minimisation of surface effects favours sample thicknesses exceeding  $15 \mu\text{m}$ .
- Minimisation of multiple scattering favours sample thicknesses less than  $50 \mu\text{m}$ .
- Unwanted temperature gradients across the sample thickness typically increase for thicker samples.

Most of the samples prepared had a thickness  $d = 30 \mu\text{m}$ . We find, in our determination of phase transition order, that there is no systematic effect of the sample thickness, in the range from  $7.5 \mu\text{m}$  to  $50 \mu\text{m}$ , on the size of the discontinuity (see 6.3). However, in the future, the intensity-fluctuation technique could be used to pin down critical exponents more carefully (which we have not worried too much about in this thesis) and also to measure elastic constants. In both cases, the form of the thickness dependence will have to be understood more quantitatively. A first attempt at gaining such a quantitative understanding has been made recently [136]; this is discussed briefly in the following section.

### 5.1.7 A closer look at intensity fluctuations

#### The ground rules for a more complete theoretical analysis

A more realistic picture of the fluctuations in the nematic must take into account, even at lowest order, the finite thickness of the sample. The fluctuations are then a function of the position  $z$ , where the dimension perpendicular to the glass bounding plates is taken to be along  $\hat{z}$ . In particular, the nematic director is pinned at the boundary and fluctuates most in between the glass plates. One might then be tempted to consider a smooth profile for the nematic director in our calculation of the intensity fluctuations. However, it is not clear that this is valid: since we are in the limit where

$$\ell \gg \lambda, \quad (5.14)$$

where  $\ell$  is the sample thickness, and  $\lambda$  the wavelength of light, the lowest  $q$  variation of the director might not contribute to a variation in the light intensity because of the adiabatic rotation of the polarisation of the light with the director (optic axis). Thus, the dominant contribution to the intensity fluctuations might, in fact, come from intermediate values of  $q$ . Taking into account the thickness dependence in its most general form gives  $\zeta$  a non-trivial  $\ell$  dependence, which, at least qualitatively, accounts for the phase difference between  $\zeta$  and the mean intensity seen in Section 5.1.6.

In principle, one could use intensity fluctuations to make quantitative estimates of the elastic constants. In order to do this, one needs to account for a few different complications:

1. The medium is anisotropic.
2. The index of refraction of the medium differs from that of the medium of incident light or that of the detector.
3. In imaging, as opposed to scattering, one is collecting light from a cone of angles in order to resolve the image.
4. Multiple scattering effects in the medium might be important.

A formalism developed by Mukhopadhyay [136] uses a transfer-matrix approach, designed to deal with a stratified anisotropic medium with a fluctuating dielectric constant. One can then, in principle, evaluate the contributions to the intensity fluctuations, order

by order. In practice, beyond lowest order, the proliferation of terms renders the project of actually making contact with experiment rather difficult. Even at lowest order, allowing for the cone of angles rather than a direct light beam, can lead to non-trivial contributions to  $\zeta$ .<sup>4</sup>

Primarily, one would like to get the specific dependence of  $\zeta$  on the elastic constants. In the one-constant approximation, and keeping terms only to lowest order,  $\zeta \approx K^{-1}$ . A description of the formalism and the results at lowest order have been worked out in part by Mukhopadhyay [136].

We can experimentally explore the question of whether the dominant systematic error is a lowest-order effect or not. To do this, we look at the *temperature dependence* of the angle variation. Higher-order terms would result in a change in shape of the angle dependence, whereas a lowest-order term would not [136]. We find that, in fact, we can collapse all the angle dependences onto one curve by multiplying each curve by a constant factor. This supports our conjecture that the dominant systematic error comes from non-parallel light rays and not from second-order fluctuation effects.

### More on the variance $\zeta$

As one goes further from the phase transition, the fluctuation variance  $\zeta$  changes less rapidly. Here, we find that the normalisation of the fluctuations with respect to the average intensity is not perfect; there are systematic errors that eventually become as large as the critical variation in  $\zeta$ , and restrict the temperature range of our fit to less than 0.1 mK.

One possibility is the incorrect subtraction of shot noise. The nematic fluctuations are spatially correlated, while the variance of the intensity distribution ignores this correlation. An alternate way of characterising the intensity fluctuations is by a spatial autocovariance function, defined by

$$h(r) = \langle \Delta(r) \cdot \Delta(0) \rangle, \quad (5.15)$$

where  $\Delta = I_1 - I_2$ , and  $r$  varies from zero to the system size. In Fig. 5.11, we plot  $h(r)$  vs.  $r$ . The nematic (here at  $T - T_{NA} \approx 5^\circ\text{C}$ ) is spatially correlated up to  $\approx 4 \mu\text{m}$ . The variance that we calculate is simply related to the autocorrelation function:

---

<sup>4</sup>A more general transfer-matrix approach that takes into account the non-collinearity between the wave vector and the Poynting vector has been developed by Galatola [137].

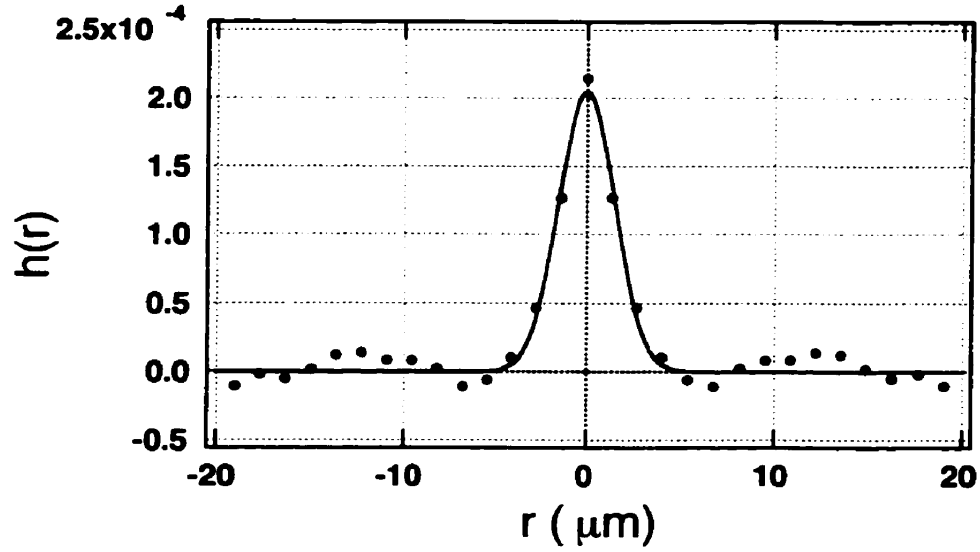


Figure 5.11: A one-dimensional profile of the autocorrelation function  $h(r)$  obtained from a  $256 \times 256$  pixel area. Pure 8CB,  $T - T_{NA} \approx 5^\circ\text{C}$ .

$$\zeta = h(0). \quad (5.16)$$

One could use the spatial correlation of the signal to separate it from the shot-noise. However, in order to get a flat background for larger  $r$ , one needs to average over several images. With our method, although we need to painstakingly calibrate the shot-noise, we can then obtain our signal from just two instantaneous images: this is extremely important in order to minimise temperature drifts.

### 5.1.8 Spatial and temporal averaging in the imaging

The intensities measured in real space via the CCD camera are not true local intensities, in the sense that they have already been averaged significantly over time and space. The spatial averaging is determined the size of each pixel and the magnification. With a pixel size  $\approx 10 \mu\text{m}$  and a magnification of  $5X$ , the resolution obtained of the liquid crystal sample was  $\approx 2 \mu\text{m}$ . Given this experimental spatial scale, the liquid crystal orientational diffusion constant

$$D_\theta \equiv K/\gamma \approx 1 \times 10^{-7} \text{cm}^2/\text{sec}, \quad (5.17)$$

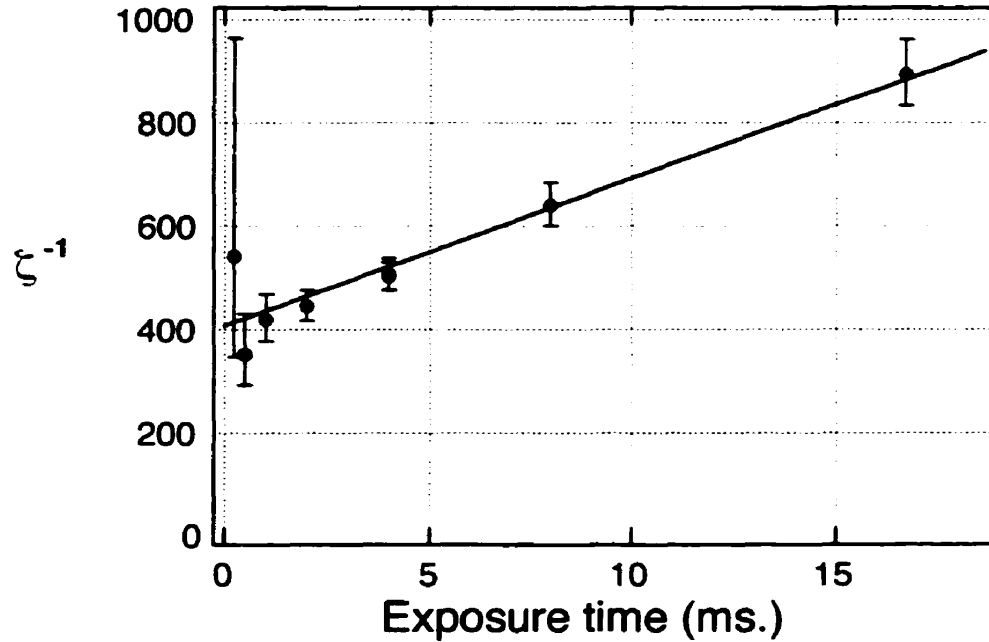


Figure 5.12: Increase in fluctuation sensitivity as the exposure time gets smaller.  $\zeta^{-1}$  scales linearly with the exposure time.

where  $K \approx 1 \times 10^{-6}$  dyn. is a Frank constant and  $\gamma \approx 10 \text{ dyn./}(\text{cm}^2 \text{ sec})$  [138] is a rotational viscosity, defines a time-scale

$$\tau \equiv L^2/D_\theta = \frac{(2 \times 10^{-4} \text{ cm})^2}{1 \times 10^{-7} \text{ cm}^2/\text{sec}} \simeq 100 \text{ msec.} \quad (5.18)$$

Thus the image exposure is always chosen to be smaller than this time scale.<sup>5</sup>

One can see the dependence of the fluctuation signal on the degree of time averaging in Fig. 5.12. One expects the fluctuation magnitude to increase until it gets cut off by the timescale set by our pixel size. Since the intensity fluctuations should essentially be a random walk in time, one expects that for an average of well-separated independent exposures, the quantity  $\zeta^{-1}$  will scale linearly with exposure time. This is easily seen: We denote  $\zeta_1$  as the variance when the “instantaneous” image has been obtained with an exposure of time

<sup>5</sup>Two CCD cameras were used in this thesis: an 8-bit CCD camera [139] was used in the early experiments (here the saturation value is 255 grey levels), while later experiments were done on a 12-bit digital CCD camera (with a saturation value of 4095 grey levels) [92]. In the earlier case, the exposure time was set by an electronic shutter, which could be varied from  $10^{-4}$  sec. to 1/60 sec.

$\tau_1 = \Delta t$ , and  $\zeta_m$ , the variance when the “instantaneous” image has been obtained with an exposure of time  $\tau_m = m\Delta t$ . Then

$$\begin{aligned}\zeta_m &\equiv \left\langle \left( \frac{\sum_{i=1}^m I_i - m\bar{I}}{\bar{I}} \right)^2 \right\rangle \\ &= \frac{\left\langle m \left( \frac{I_1 - \bar{I}}{\bar{I}} \right)^2 \right\rangle}{m^2} \\ &= \frac{\zeta_1}{m}.\end{aligned}\tag{5.19}$$

In the above, we have assumed that the exposure  $\tau_m$  is made up of  $m$  independent exposures (we could thus ignore the cross terms). Thus, one expects  $\zeta \propto \frac{1}{\tau}$ , where  $\tau$  is the total exposure time.

In the experiment shown in Fig. 5.12, however, the increments in the exposure time  $\tau$  are not necessarily independent. The data, however, are still broadly consistent with the above ansatz, but the error bars are quite large in the region where the saturation should occur. The large uncertainty in the first point is due to low light levels. In the case of the digital CCD camera, the light source used was a flashlamp with, approximately, a  $10\ \mu\text{s}$  flash duration, much shorter than the sub-millisecond times of the above test; thus, for such short exposures, one can treat the nematic as being essentially static.

## 5.2 The gradient trick

For temperatures well above  $T_{NA}$ , one can simply measure  $\zeta(T)$ , calculated using the entire image. Since the temperature dependence of the fluctuations is relatively weak when compared to that close to the transition, the value of  $\zeta(T)$  does not vary across the image.<sup>6</sup> Close to  $T_{NA}$ , however, any existing temperature gradients will result in a spread of values for  $\zeta(T)$  that smears out resolution. Instead, we take advantage of this gradient in our experiment to improve our temperature resolution. The method is straightforward:

- We locate  $T_{NA}$  by varying the temperature until we see the NA interface in the field-of-view. The typical gradient applied across the field-of-view is  $0.1^\circ\ \text{C}$ . When the

---

<sup>6</sup>We assume for the moment that any variation across the image comes from temperature. As we shall see below, residual illumination variations can become important far from  $T_{NA}$ .

set-up is well-adjusted, the gradient is linear across the sample and the NA interface appears as a straight line (see Fig. 5.1).

- Varying the temperature by several mK shifts the position of the interface. We thus calibrate the interface position against temperature.
- With this calibration, we translate the spatial dependence of  $\zeta$  into a temperature dependence. We divide our image into strips parallel to the NA boundary, which is typically flat over the field-of-view, which is 2 – 3 mm. Each strip then corresponds to a slightly different temperature.
- Each image that contains an NA interface is *self-calibrating* in that over small times, the gradient remains, in practice, constant while the overall temperature fluctuates slowly. The r.m.s. fluctuations in temperature over long times were roughly 0.1 – 0.5 mK. Over short times (several seconds), the interface moves by less than 0.05 mK. This was in spite of observed short-time oscillations in the RTD output: as we had noted in Section 4.4.3. the sample blocks act as low-pass filters for temperature oscillations. In essence, the interface itself is our best thermometer, and the long-time variations in temperature are not a concern.
- The temperature stability is such that the interface width should be on the order of a pixel. However, the limiting factor on the interface width turns out not to be temperature stability, but an unwanted temperature gradient in the plane perpendicular to the applied temperature gradient. In particular, a temperature gradient in the direction perpendicular to the plane of the sample substrate results in a smearing of the interface. In our experiments this was the real limit to resolving the discontinuity, and varied from 0.5 mK to 2 mK. Future design improvements can, with a little effort, improve on this by at least an order of magnitude

The essence of the gradient trick is that driving a system weakly out of equilibrium is often a sensitive way of measuring equilibrium properties. This is also used in other sensitive techniques at first-order transitions: Cladis *et al.* [16] used a dynamical technique to deduce latent heats too small to measure by traditional high-resolution calorimetry, and Garland *et al.* [66] have used phase shifts in AC calorimetry as a qualitative sign of the existence of a discontinuous jump at the transition.

### 5.3 Summary

In this chapter, we have demonstrated that intensity fluctuations can be well-characterised in a way that allows for easy reproducibility in other microscopy set-ups. We have some indication that the assumption of small fluctuations is correct, and the residual systematic errors arises from an, as yet, unaccounted-for lowest-order effect—this is discussed further in [136]. We have discussed the dependence of fluctuations on the light intensity, the angle of the sample optic axis with respect to the crossed polarisers, the sample thickness dependence, and the dependence on exposure time. We are now ready to study the physical dependence of the nematic fluctuations on temperature as the NA transition is approached from above.

## Chapter 6

# INTENSITY FLUCTUATION MICROSCOPY: RESULTS

### 6.1 Introduction

In previous chapters, we have described our experimental set-up and shown how it may be used to extract a quantitative measure of fluctuations in the nematic phase. Near the NA transition, these fluctuations show critical scaling. In this chapter, we apply the methods developed in the previous chapters to study this scaling, which is at the heart of this thesis.

What are the interesting problems for an experimental physicist at the NA transition? By far the most interesting region in the space of material parameters is the nebulous one that separates the strongly type-1 region from the strongly type-2 region. Here the superconductor analogy is on less solid ground, the question of phase-transition order is still open, and experimental measurements of critical exponents are least definitive. As described in Chapter 3, there is some evidence for a crossover from a first-order phase transition mediated by  $\delta S$ - $\psi$  coupling, to one driven by  $\delta n$ - $\psi$  coupling. As described in Chapter 3, there is one mechanism due to Halperin, Lubensky and Ma (HLM) [14] that would predict such a crossover. However, an unambiguous experimental test of the HLM mechanism would be valuable here as it is yet unknown what role smectic fluctuations play in the phase transition.

In this thesis, we probe the weakly type-1 region in pure 8CB and 8CB-10CB mixtures.

First, we measure the fluctuations as a function of temperature in pure 8CB, a material that exhibits a NA transition that is indistinguishable from second order when studied by traditional high-resolution calorimetry. Dynamical measurements by Cladis *et al.* have suggested that this transition is first order. This material is thus ideal to establish the sensitivity of the new high-resolution technique, intensity-fluctuation microscopy that has been developed in this thesis. Indeed, we do find a measurable discontinuity, characterised by a dimensionless temperature  $t_0$ , defined earlier, that sets the stage for the other experiments described in this chapter.

In Chapter 3, we predicted, theoretically, a measurable dependence of  $t_0$  on an external magnetic field. In this chapter, we describe experimental results for a study of an applied magnetic field on the discontinuity  $t_0$  in 8CB. Although a non-analytic dependence of the fluctuations on the applied magnetic field is expected, we do not find such a dependence, to the resolution of our experiment.

Then, we look at the effect of thickness and try to induce a tricritical point with an anchoring field. This produced unexpected, but interesting results.

Next, we look at the zero-field  $t_0$  and its field dependence in a mixture of 0.41 (mole-fraction) 10CB in 8CB, which has been established in previous studies by other groups [15, 46] to be at the Landau tricritical point (LTP). At this point, HLM theory is on more solid ground, as the neglect of smectic fluctuations is more reasonable here.

Finally, we look at the variation of  $t_0$  as a function of mixture concentration. One of the goals here was to extend the known dependence of the discontinuity as a function of concentration in the 8CB-10CB system, all the way to pure 8CB.

The results of the above experiments put bounds on the validity of HLM theory; these consequences are discussed in a concluding section.

## 6.2 Fluctuations in 8CB

### 6.2.1 Zero-Field Measurements

Samples of 8CB of varying thicknesses were studied. The data for two of them are shown here:

1. The first is a  $7.5\ \mu\text{m}$  planar-anchored sample [140]. This sample is made between glass

slides and analysed on the commercial hot-stage and an 8-bit CCD camera. This experiment motivated the design of the new set-up. In this case, the gradient was not applied perpendicular to the anchoring direction; rather, the gradient was simply picked out by pre-existing temperature inhomogeneities in the hot-stage. Too, the quantity  $\zeta$  is averaged over 16 images in this case. In the second data set shown, such an averaging is not done, as the primary limitation to improved resolution are systematic errors, not statistical errors. The plot of fluctuation as a function of temperature above  $T_{NA}$  is shown in Fig. 6.3.

2. The second sample is a  $30\ \mu\text{m}$  sample made between glass cubes, and analysed in the gradient hot-stage set-up described in Chapter 4. Here, the applied temperature gradient was perpendicular to the anchoring direction. The plot of fluctuation as a function of temperature for this sample is shown in Fig. 6.6.

### Interface Calibration

A nematic–smectic-A interface was obtained by tuning the temperature to straddle  $T_{NA}$ . The interface was calibrated as described in the Section 5.2; the dependence of interface position on temperature in Sample 1 is shown in Fig. 6.1. One can fit a straight line through the data; the slope of this straight line gives the temperature gradient per pixel  $G = (3.2 \pm 0.2) \times 10^{-5}\text{K/pixel}$ .

For samples in the second set-up, the applied temperature gradient across the field of view was somewhat larger—shown in Fig. 6.2 is an interface calibration for Sample 2.

### $\zeta$ vs. $T$ in 8CB: Sample 1

Once we have calibrated the position of the NA interface against temperature, we calculate  $\zeta$  individually for each isothermal strip parallel to the interface. The resulting fluctuation-vs.-temperature profile for Sample 1 ( $d = 7.5\ \mu\text{m}$ ,  $G = 0.17 \pm 0.01\ \text{K/cm}$ ) is plotted in Fig. 6.3. There are three distinct sections to the graph:

1. The smectic section: Here,  $\zeta = 1 \pm 2 \times 10^{-6}$ , and the smectic fluctuation level is flat and indistinguishable from the noise.

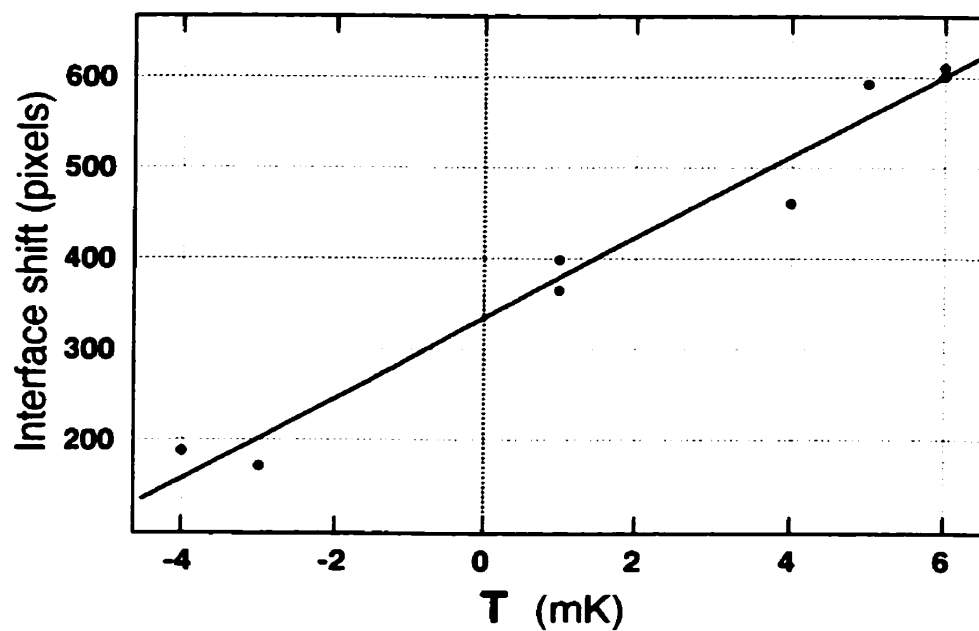


Figure 6.1: Sample 1: Calibration of interface position vs. temperature. The temperature gradient is given by the slope  $G = (3.2 \pm 0.2) \times 10^{-5}$  K/pixel, equivalent to  $0.17 \pm 0.01$  K/cm.

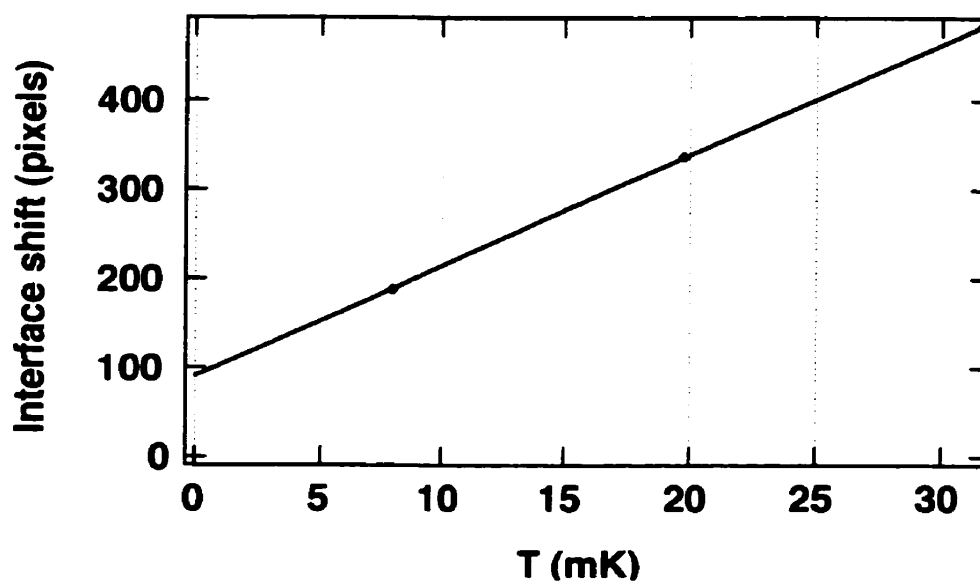


Figure 6.2: Sample 2: Calibration of interface position vs. temperature. The temperature gradient is given by the slope  $G = (8.06 \pm 0.05) \times 10^{-5}$  K/pixel, equivalent to  $0.59 \pm 0.02$  K/cm.

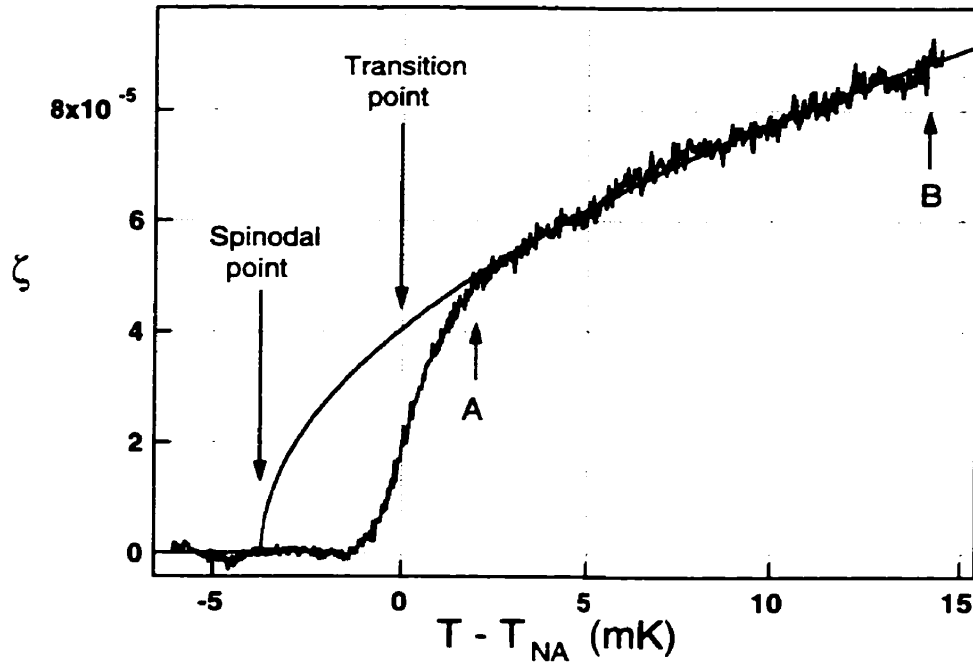


Figure 6.3: The fluctuations in the nematic are well fit by a power law with an exponent 0.5 that extrapolates to zero at the phantom divergence point (spinodal point)  $T^*$ . (The range of the fit is the region between the points A and B marked on the graph.) This divergence is preempted by a discontinuous transition at  $T_{NA}$ . In dimensionless units, the discontinuity strength is  $t_0 = (T_{NA} - T^*)/T_{NA} = 1.2 \pm 0.1 \times 10^{-5}$ . Data obtained from 16 images of a pure 8CB sample.  $d = 7.5 \mu\text{m}$ ,  $G = 0.17 \pm 0.01 \text{ K/cm}$ .

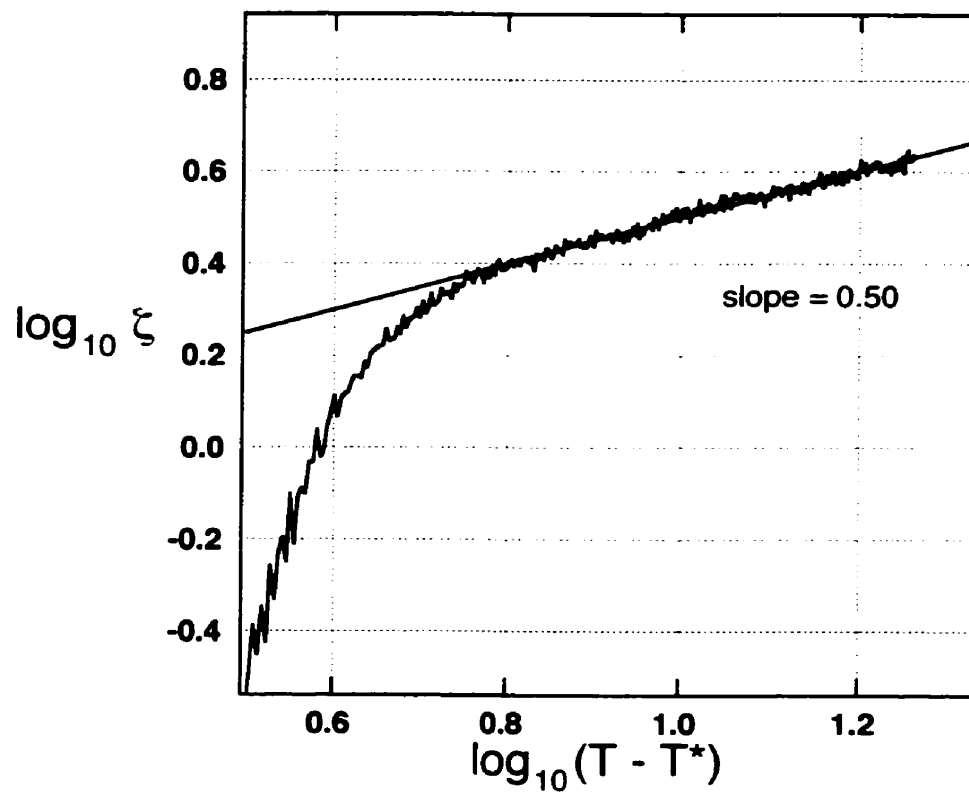


Figure 6.4: Log-log plot is consistent with the best-fit slope of 0.50.

2. The nematic section: The data here fit a power law of the form

$$w_0 + w_1(T - w_2)^{w_3} \quad (6.1)$$

with  $w_0 = 0.1 \pm 1.0 \times 10^{-6}$ ,  $w_1 = 2.10 \pm 0.01 \times 10^{-5}$ ,  $w_2 = 3.74 \pm 0.38$  mK, and  $w_3 = 0.50 \pm 0.05$ . The fit was done over the largest temperature range that still kept the residuals (top curve in Fig. 6.3) flat. The coefficient  $w_0$  was held to the smectic level, while  $w_3$  is the exponent of the power law. The coefficient  $w_2$ , the divergence point of the power law, is identified with the spinodal temperature  $T^*$  introduced in Chapter 3. However, it is a phantom divergence point, as the actual phase transition is located at the interface, i.e., at  $T - T_{NA} = 0$  mK. We will see below that we can fit for the location of  $T_{NA}$  in the interfacial region. Plotting  $\log_{10} \zeta$  vs.  $\log_{10}(T - T^*)$  (Fig. 6.4) yields a straight line whose slope is consistent with the fitted exponent.

3. The interfacial section: This region appears to be linear, and, as a starting point, we make the ansatz that it arises from a temperature gradient in the thickness direction. This would result in a smearing of the interface that would, to a first approximation, be linear. With this ansatz, we can fit the data  $\zeta_{meas}$  to a model function that is a power law with local averaging

$$\zeta_{meas}(T) = \int_{-\infty}^{\infty} \zeta_{model}(T') K(T - T') dT' \quad (6.2)$$

where  $K(T - T')$  is the kernel, which we choose to be

$$K(T - T') = \begin{cases} 1/w_4 & \text{if } -w_4/2 < T - T' < w_4/2 \\ 0 & \text{otherwise} \end{cases} \quad (6.3)$$

$$\zeta_{model}(T') = \begin{cases} w_0 + w_1(T' - w_2)^{w_3} & \text{if } T' > w_5 \\ w_0 & \text{otherwise} \end{cases} \quad (6.4)$$

The parameter  $w_5$  locates  $T_{NA}$  in the interfacial region, while the parameter  $w_4$  is a measure of the (linear) temperature gradient (i.e. the width of the interfacial region).

Some important points are well worth noting here. First, there is an abrupt change in fluctuations at the NA transition, quantified by the difference between the transition

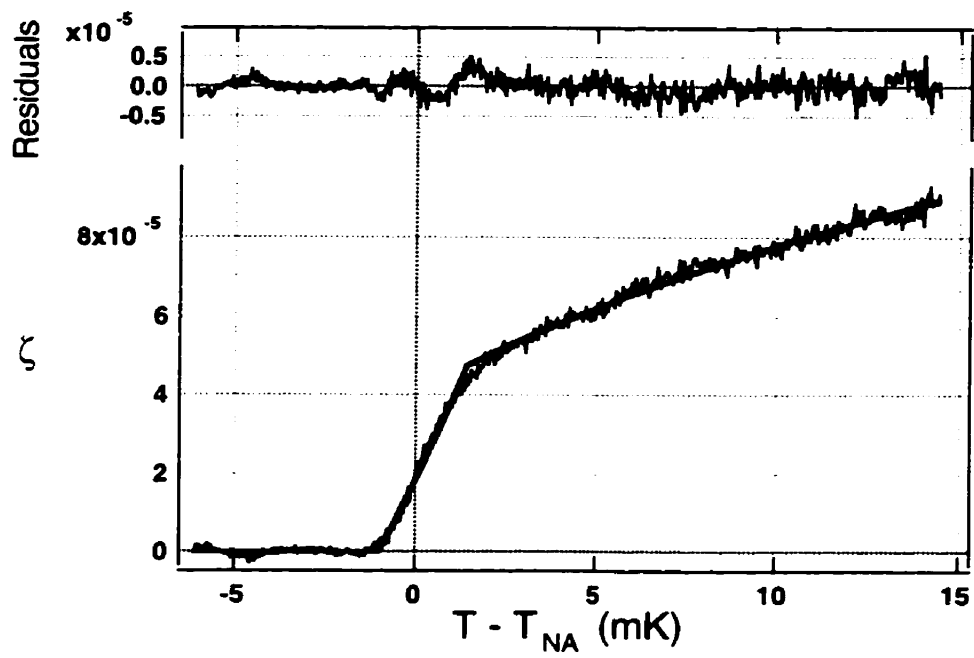


Figure 6.5: Data from Fig. 6.3 fit to a convolution of a power law with a temperature gradient. The top curve in the graph shows the residuals between the data and the convolution fit.

temperature and the spinodal temperature  $T_{NA} - T^* = 3.7 \pm 0.4$  mK.<sup>1</sup> We can characterise this *discontinuity* with the dimensionless measure defined in Chapter 3

$$t_0 = (T_{NA} - T^*)/T_{NA} = 1.2 \pm 0.1 \times 10^{-5}. \quad (6.5)$$

We also get a measure of the temperature gradient across the thickness of the sample,

$$\delta T_{thick} = 1.2 \pm 0.1 \text{ mK}. \quad (6.6)$$

Finally, one notices that the convolution curve fit is systematically off from the data over a small temperature range near the crossover from the nematic section to the interfacial section (around  $T - T_{NA} \approx 1.4$  mK). The “rounding” observed here in the data (see Fig. 6.5) could be due to a non-linear meniscus effect, sketched in Section 4.4.5 (Fig. 4.11).

### $\zeta$ vs. $T$ in 8CB: Sample 2

Having described the data analysis procedure above, in detail, we may now simply state the results for the 30  $\mu\text{m}$ -thick Sample 2 (see Fig. 6.6). Here, we find that

$$T_{NA} - T^* = 5.0 \pm 0.5 \text{ mK} \quad (6.7)$$

$$t_0 = 1.6 \pm 0.2 \times 10^{-5} \quad (6.8)$$

$$\delta T_{thick} = 2.0 \pm 0.1 \text{ mK}. \quad (6.9)$$

## 6.2.2 Magnetic Field Measurements

The magnetic field effect at the transition was probed with a field that could be varied from 0 T to 1.2 T. The initial runs were done at 1.5 T, but the magnet was unable to provide 1.5 T for long-enough runs without damage to the power supply. Later runs were limited to 1.2 T. Contrary to initial expectations, no suppression of the fluctuations was seen within 50 mK of the transition point. Two curves are shown in Fig. 6.7. The data curves (black representing zero field, and grey representing measurements at a field of 1.2 T) practically fall on top of each other. Likewise, we see no shift in  $t_0$

<sup>1</sup>In an early realisation of this experiment we had reported a discontinuity of 2 mK. The discontinuity is in fact a fit parameter and is sensitive to the baseline of the fit; it turns out to be important to correctly account for the shot-noise contribution to the intensity fluctuations.

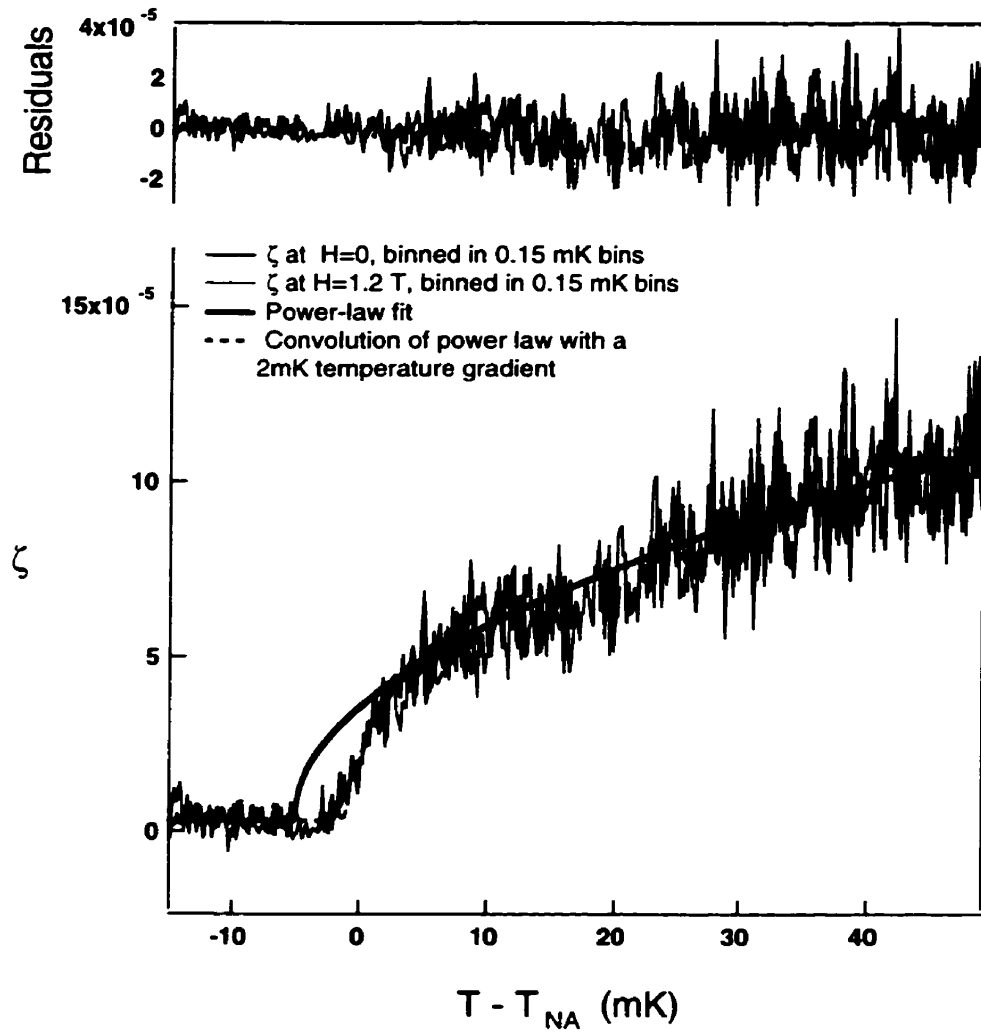


Figure 6.6: Data obtained from two images of a pure 8CB sample,  $d = 30 \mu\text{m}$ ,  $0.59 \pm 0.02\text{K/cm}$ . Here,  $t_0 = \frac{5.0 \pm 0.5 \text{ mK}}{307 \text{ K}} = 1.6 \pm 0.2 \times 10^{-5}$ .

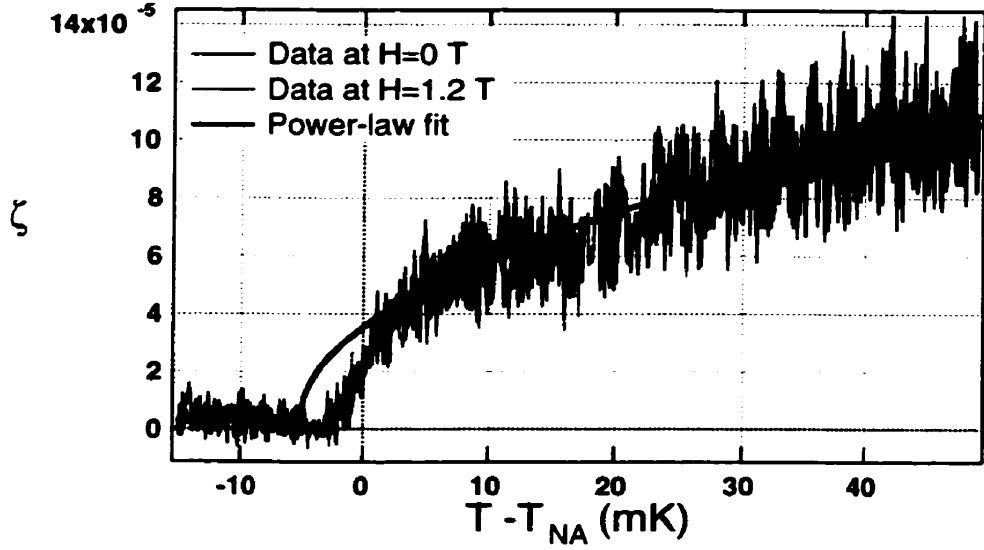


Figure 6.7: Effect of magnetic field on 8CB critical behaviour: the black data curve, which represents the zero-field measurement, falls on top of the grey data curve, which is obtained at a magnetic field of 1.2 T. The data is fit to the exponent  $\bar{\nu} = 0.5$  (grey fit line). Pure 8CB,  $d = 30 \mu\text{m}$ ,  $G = 0.59 \pm 0.02 \text{K/cm}$ .

However, deep in the nematic, we do see a suppression of the fluctuations. Plotting  $\zeta$  vs.  $H$  (see Fig. 6.8), we find that this depression falls off quadratically with increasing field:

$$\zeta = \zeta_0 - g_H H^2. \quad (6.10)$$

The temperature dependence of the coefficient  $g_H$  is shown in Fig. 6.9. The slope of the data in Fig. 6.9,  $g_H$ , can be plotted as a function of temperature (Fig. 6.9). The reduction in the field-effect on approaching  $T_{NA}$  reflects quite clearly the fact that the (twist and bend) elastic constants are getting stiffer as one approaches  $T_{NA}$ . In fact, since the magnetic coherence length is  $\xi_H = (\frac{K}{\xi})^{\frac{1}{2}} \frac{1}{H}$ , one reasonably expects that the field dependence is always a function of  $\xi_H$ ; i.e., the coefficient must obey  $g_H \propto \frac{1}{K}$ , where  $K$  is a diverging elastic constant. Fitting to the value of  $\bar{\nu} = 0.5$  that is consistent with other experiments, and with our earlier fit in zero field, we find that the data clearly agrees with this.

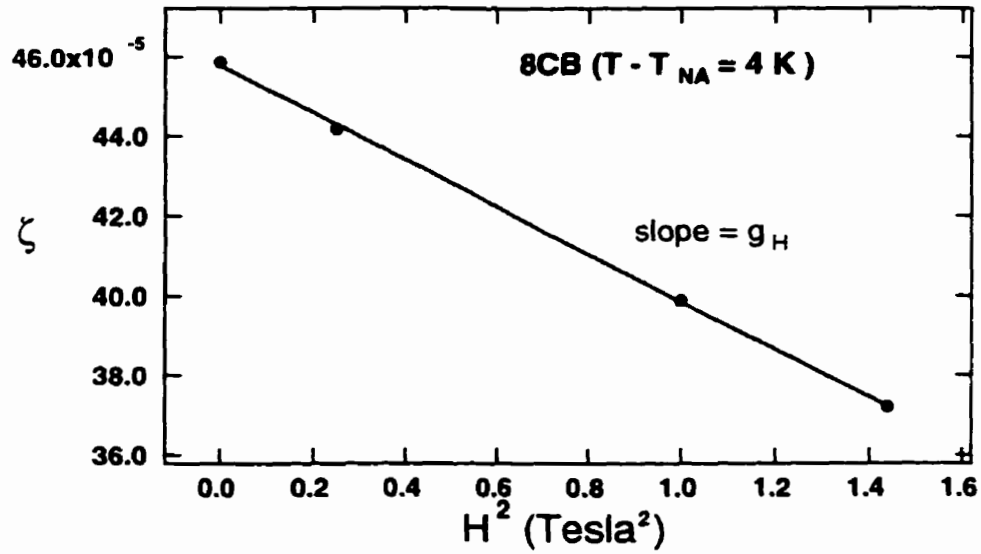


Figure 6.8: Deep in the nematic, the field suppresses the fluctuations, the strength of this suppression being measured by the coefficient  $g_H$ . Pure 8CB,  $d = 30 \mu\text{m}$ .

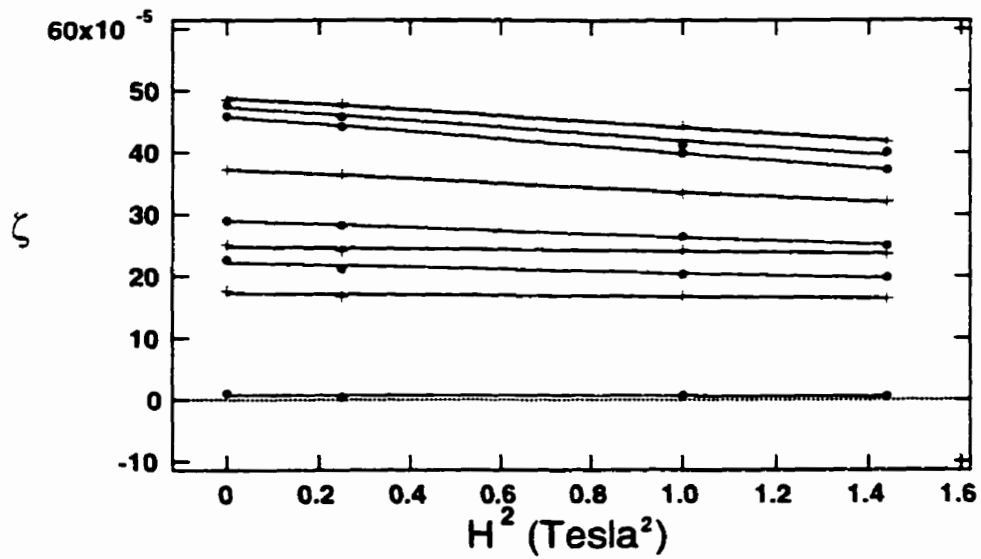


Figure 6.9: The field-suppression of the fluctuations becomes weaker as  $T \rightarrow T_{NA}$ . Top to bottom field-suppression curves at  $T - T_{NA} = 6.2^\circ\text{C}$ ,  $5.0^\circ\text{C}$ ,  $3.8^\circ\text{C}$ ,  $2.6^\circ\text{C}$ ,  $1.5^\circ\text{C}$ ,  $1.1^\circ\text{C}$ ,  $0.7^\circ\text{C}$ ,  $0.3^\circ\text{C}$ , and  $-0.1^\circ\text{C}$ , respectively.

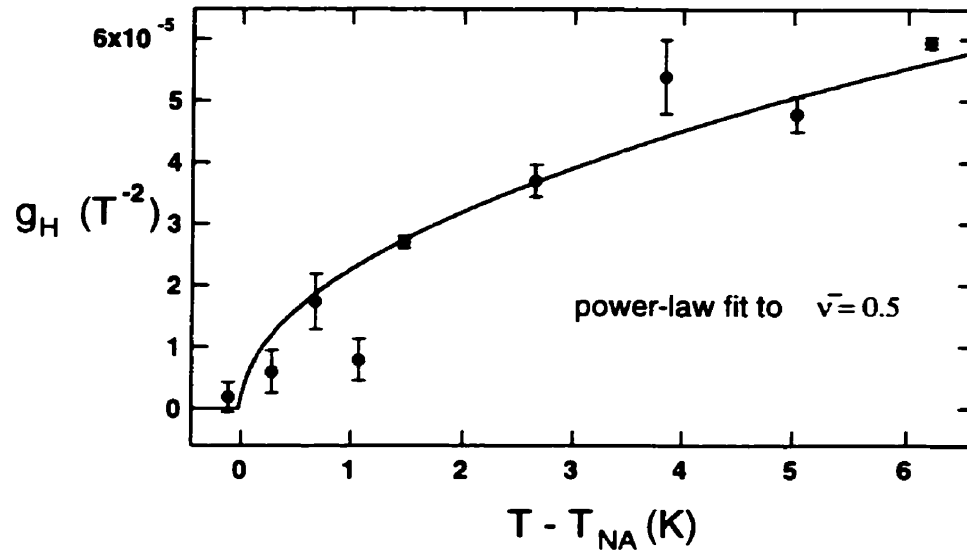


Figure 6.10: The field-suppression coefficient  $g_H$  is smaller at temperatures close to  $T_{NA}$ , reflecting the stiffer elastic constants as one approaches the transition. Pure 8CB,  $d = 30 \mu\text{m}$ .

### 6.2.3 Summary of Results in 8CB

First, we find a clear discontinuity in the fluctuations in 8CB. The strength of this discontinuity in data from the two samples shown was

$$\begin{aligned} t_0 &= (1.2 \pm 0.1) \times 10^{-5}, \text{ and} \\ t_0 &= (1.6 \pm 0.2) \times 10^{-5}, \end{aligned} \quad (6.11)$$

respectively. The difference in these values is well above the error bars in the individual values. As we do not know where this variability originates, we shall explore the possibility that it arises from the differing sample thickness.

Next, we find, surprisingly, no magnetic field effect on the discontinuity  $t_0$ . What do the magnetic field studies on a  $0\text{ T} - 1.5\text{ T}$  field tell us about the critical field of  $\approx 10\text{ T}$  predicted via the HLM scenario? A weaker effect than predicted would correspond to a larger critical field. We do not need to suppress the fluctuations completely to detect the effect—all we must show is a linear suppression for small  $\frac{H}{H_c}$ . The HLM scenario predicts a linear suppression of  $t_0$  as a function of  $|H|$ . For small  $|H|$ , we calculate numerically a

dependence

$$t_0(H)/t_0 = 1 - m H/H_c, \quad (6.12)$$

where  $m = (2.17 \pm 0.01)$  is the slope of the linear suppression shown in Fig. 3.1 in Chapter 3. In our case, our confidence level for  $t_0$  is roughly 10%;<sup>2</sup> i.e., the largest suppression of  $t_0$  that we would *not observe* is

$$t_0(H)/t_0 = 0.9 \quad (6.13)$$

This puts a lower bound on the value of  $H_c$ . The maximum field used is

$$H = H_{max} = 1.5 \text{ T} \quad (6.14)$$

Thus, for 8CB, we can calculate  $H_c$ :

$$\begin{aligned} H_c &= \frac{m H}{1 - t_0(H)/t_0} \\ &= \frac{(2.17 \pm 0.01) H}{1 - t_0(H)/t_0} \\ &\approx 21.7 \times 1.5 \text{ T} \\ &= 33 \text{ T}. \end{aligned} \quad (6.15)$$

Thus, the lower bound for the critical field in our measurements is  $\approx 30 \text{ T}$ .

### 6.3 The effect of varying thickness

Two independent motivations led us to study the effect of varying sample thickness on the discontinuity  $t_0$ . First, we wished to establish whether or not the variability in values from sample to sample arose from thickness effects.

Second, and more importantly, we wished to explore the idea that an anchoring field could, in principle, play a role similar to a magnetic field in suppressing nematic director fluctuations. The magnetic field sets a length scale, the magnetic coherence length  $\xi_H$ . We expect to see magnetic field effects when  $\xi_H \approx \lambda$ , where  $\lambda$  is a penetration length. Similarly, we expect to see some suppression of fluctuations when  $d \approx \lambda$ , where  $d$  is the sample thickness.

This test, however, is fraught with complications:

---

<sup>2</sup>The effect of systematic errors on the magnetic-field behaviour is smaller because there is an easily identifiable correlation between the systematics in the field-off and field-on case.

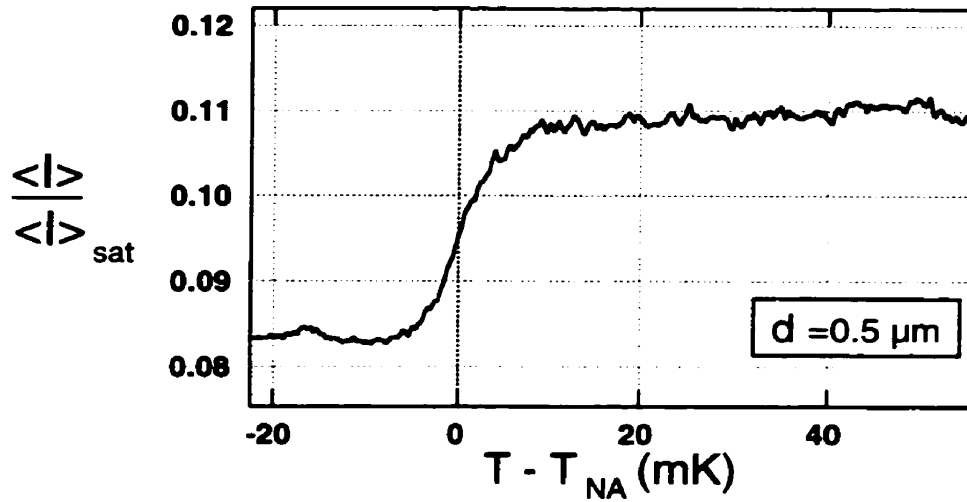


Figure 6.11: Discontinuity in the mean intensity in the 8CB wedge sample (normalised to the CCD saturation value.) Data shown for  $d = 0.5 \mu\text{m}$ .

1. The magnetic field is a clean bulk effect. The anchoring field, on the other hand, is stronger at the surface and is thus intrinsically non-uniform.
2. Because the expected critical field is small, the magnetic field has a weaker effect on smectic fluctuations than on nematic director fluctuations. The anchoring field suppresses the smectic fluctuations to the same order, and cannot therefore be a clean test of the HLM effect.
3. As one goes to thinner samples, finite-size effects should round off the transition, whether first order or second order and convert it to a crossover. It is not clear whether this effect would in principle be separable from the effect on the nematic director fluctuations.
4. Related to this, we also do not have a good estimate for  $\lambda$  that goes beyond HLM theory.

Nevertheless, the effect of the anchoring field was also probed, simply to see if it provided any new information at all. We looked at a thin wedge sample, where the thickness was varied from  $d \approx 0.5 \mu\text{m}$  to  $d \approx 2.5 \mu\text{m}$ .

In this sample, we observed (see Fig. 6.11) a rather sharp discontinuity in the *mean*

*intensity*. Since the fluctuation level in the smectic is indistinguishable from the shot-noise, one can still analyse the divergence of fluctuations in the nematic. We looked at three regions of the sample, at the thin end ( $\approx 0.5 \mu\text{m}$ ), the thick end ( $\approx 2.5 \mu\text{m}$ ), and at a point roughly in the centre. The data and a fit to a power-law exponent  $\bar{\nu} = 0.5$  are shown in Fig. 6.12.

It is worthwhile to try to understand the possible cause of this sharp discontinuity in the mean intensity, for two reasons:

1. It is not seen in any of the data on the thicker samples; all that is seen typically is a kink in the mean-intensity curve, not a jump discontinuity.
2. A similar sharp discontinuity, suggesting to the eye a value of  $t_0$  on the order of several 100 mK, was observed by Lelidis and Durand in their electric-field studies on 8CB. This result is in conflict both with our data, which gives a discontinuity strength of  $\approx 4$  mK, and with adiabatic calorimetry results of Thoen and coworkers [65] which put an upper bound on the discontinuity at  $\approx 5$  mK.<sup>3</sup>

One possible explanation for this discontinuity is twist. Boundary conditions that impose a twist (if the anchoring directions on the two plates are rotated with respect to each other) could make a continuous NA transition first order, because the twist in the nematic phase must be expelled in the smectic-A. It is akin to a cholesteric-smectic-A transition, which is always first order.

As discussed in Chapter 4, the twist angle between the two bounding glass surfaces in the prepared samples is less than  $0.2^\circ$  in the glass cubes and less than  $0.6^\circ$  in samples prepared with the glass slides. It is thus moderately larger for the glass-slide samples. No systematic difference between the “cube samples” and the “slide samples” was observed, and no systematic change was seen between the  $7.5 \mu\text{m}$ , the  $30 \mu\text{m}$  and the  $50 \mu\text{m}$  samples, leading us to be certain that imposed twist did not affect our measurement of  $t_0$  at the transition.

The thin sample in this experimental run was prepared between glass slides. The effect of a twist in the centre of the sample should scale as the twist angle divided by the sample thickness. (See below.) Clearly, the effect is magnified by at least an order of magnitude for

---

<sup>3</sup>The adiabatic calorimetry puts an upper bound on the latent heat at the NA transition. This can be translated to a value of  $t_0$  using the Landau parameters in Ref. [15]. See Appendix B for a detailed discussion.

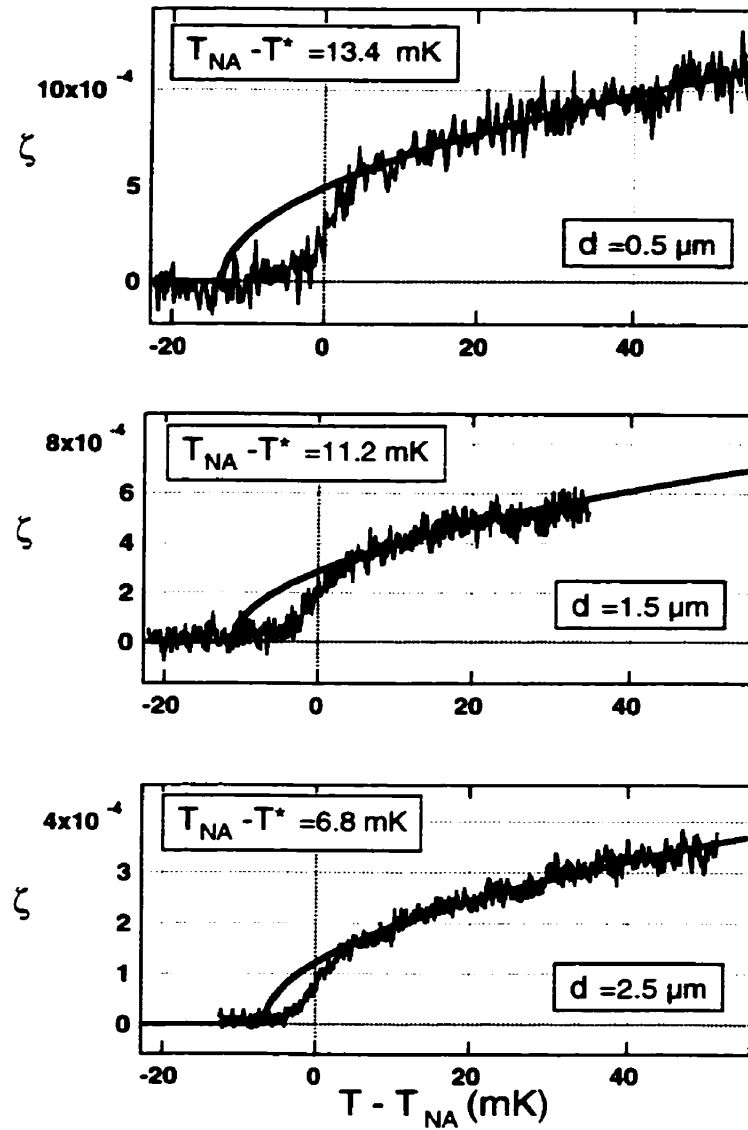


Figure 6.12: The divergence of fluctuations at three points in a thin wedge sample of 8CB, with thicknesses  $0.5 \mu\text{m}$ ,  $1.5 \mu\text{m}$ ,  $2.5 \mu\text{m}$ . The applied gradients for the three data sets, from top to bottom, are  $G = 1.06 \pm 0.02 \text{ K/cm}$ ,  $G = 0.57 \pm 0.01 \text{ K/cm}$ , and  $G = 0.53 \pm 0.01 \text{ K/cm}$ , respectively.

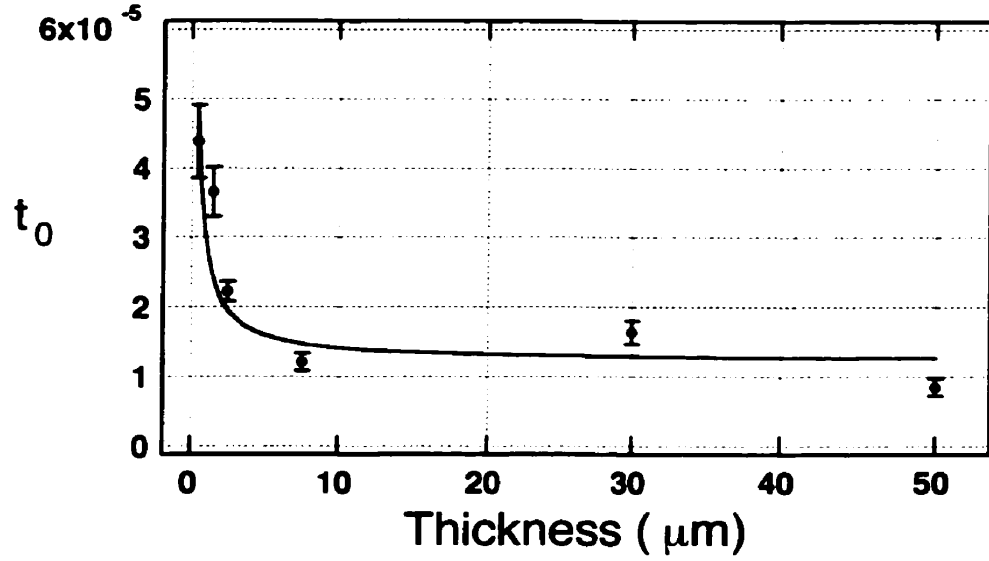


Figure 6.13:  $t_0$  is roughly constant for thick samples ( $d = 7.5 \mu\text{m}$ ,  $d = 30 \mu\text{m}$ , and  $d = 50 \mu\text{m}$ ). There is, however, a drastic increase for the thin sample  $0 \mu\text{m} < d < 2.5 \mu\text{m}$ . The data are fit to the form  $t_\infty + k/d$ .

a sample that is on the order of  $1 \mu\text{m}$ ! It is thus possible that the large discontinuity in the *mean intensity* arises from the combination of a small twist and a small sample thickness.

We can try to estimate (order of magnitude) whether such an effect makes sense. The discontinuity at the cholesteric smectic-A transition is predicted to be [141]<sup>4</sup>

$$t_0 = (2K_2C/\alpha^2)^{1/2}q_0, \quad (6.16)$$

where  $C = |C_0|(x - x^*)$  and  $\alpha = A/t$  are the quartic coefficient and the temperature-independent part of the quadratic Landau coefficient, respectively. The pitch  $q_0 = \Delta\theta/d$ , where  $\Delta\theta$  is the twist angle and  $d$  the sample thickness.

In the above equation, the quantity inside the parentheses has units of length and we denote it  $\ell_t$

$$\ell_t = (2K_2C/\alpha^2)^{1/2}. \quad (6.17)$$

Experimentally, at the NA transition in a sample with a constant imposed rotation  $\Delta\theta$  of

<sup>4</sup>Note that the calculation for a twisted nematic is more complicated, and what follows is simply intended as a crude order-of-magnitude estimate.

the two anchoring boundaries, one therefore expects a dependence

$$t_{0twist} = t_{\infty} + \Delta\theta\ell/d \quad (6.18)$$

where  $t_{\infty}$  is the discontinuity for zero twist and  $\ell$  will be compared to the predicted  $\ell_t$ . A plot of  $t_0$  vs. thickness  $d$  is shown in Fig. 6.13. The fit to the above form yields a value of  $t_{00} = 1.2 \pm 0.4 \times 10^{-5}$ , well within the systematic errors for samples with thickness ranging from  $7.5 \mu\text{m}$  to  $50 \mu\text{m}$ . The second coefficient gives

$$\Delta\theta\ell = 1.8 \pm 0.4 \times 10^{-5} \mu\text{m}. \quad (6.19)$$

Using a value of  $\Delta\theta \approx 0.6^\circ \approx 10^{-2} \text{rad}$ ,<sup>5</sup> we find

$$\ell \approx 2 \text{nm}. \quad (6.20)$$

Based on

$$K_2 \approx 2 \times 10^{-6} \text{dyne (at the transition)}$$

$$C/\alpha^2 \approx 10^{-8} \text{cm}^2/\text{dyne}, \quad (6.21)$$

$$(6.22)$$

we can estimate  $\ell_t$ ,

$$\begin{aligned} \ell_t &= (2K_2C/\alpha^2)^{1/2} \\ &\approx 1.4 \times 10^{-7} \text{cm} \\ &\approx 1.4 \text{nm}, \end{aligned} \quad (6.23)$$

Thus  $\ell$  from our measurement is roughly the same order of magnitude as  $\ell_t$ . Collecting the fitted values of  $t_0$  from samples of different thickness, we find the dependence shown in Fig. 6.13. For thickness  $d > 5 \mu\text{m}$ , the systematic trend is negligible. For extremely thin samples, an *increase* in  $t_0$  is observed, which is plausibly due to an imposed twist. An obvious experiment, which we had no time to try, would be to redo these measurements using a  $\Delta\theta$  deliberately set to be, say, ten times larger.

---

<sup>5</sup>The wedge sample was not prepared in the set-up described in Chapter 4 for accurately controlling the various degrees of freedom. To get the small thickness, much more force had to be used than could be used with the rather delicate adjustments entailed by that set-up. The two glass plates were scribed lightly close to the edge and the scribes were lined up by eye. For this, we estimate a tolerance in angle of  $\approx 0.6^\circ$ .

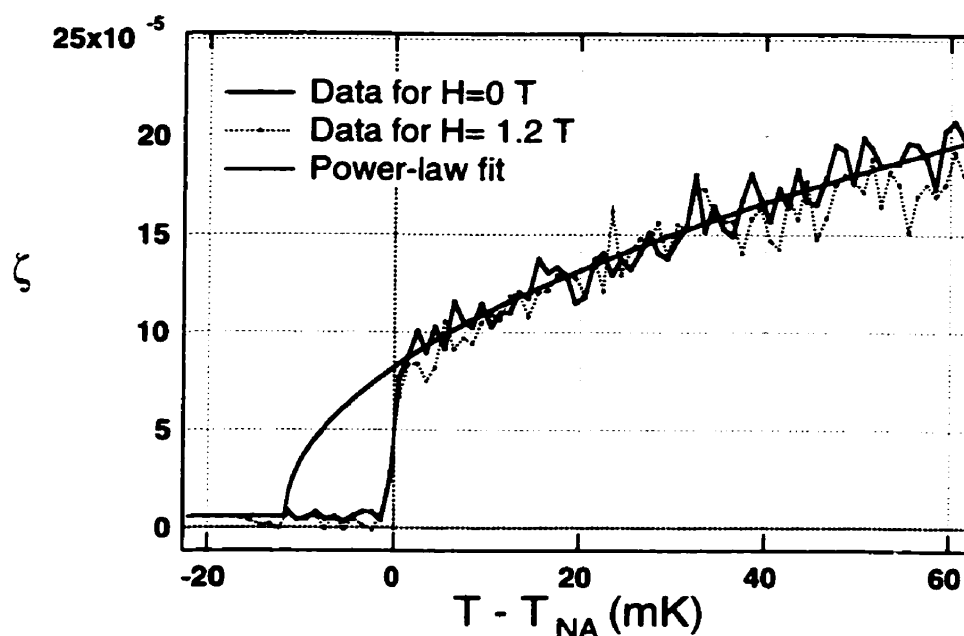


Figure 6.14: The fluctuations go to zero in the LTP mixture ( $x = 0.41$ ); in this case,  $t_0 = 3.8 \pm 0.8 \times 10^{-5}$ . Once again, there is no field effect (grey curve) close to  $T_{NA}$

#### 6.4 Measurements at the LTP

Once again, as shown in Fig. 6.14, there is no discernible effect of the field on the fluctuations within 40 mK of  $T_{NA}$ . Repeating the analysis of Section 6.2.2, one again finds a non-critical suppression of the fluctuations for larger  $T$ . The coefficient  $g_H$  (Fig. 6.15) is once again consistent with a  $\bar{\nu} = 0.5$  power law. Close to  $T_{NA}$ , the suppression is weak enough to be below the noise level.

#### 6.5 The variation of the first-order discontinuity in 8CB-10CB mixtures

The variation of the latent heat in 8CB-10CB mixtures was studied by Marynissen *et al.*, and later reanalysed by Anisimov *et al.*. These studies largely focussed on the cross-over from mean-field first order behaviour in the proximity of the Landau tricritical point (LTP), which is at  $x = x^* \simeq 0.42$ , where  $x$  is the mole fraction of 10CB in the mixture. The

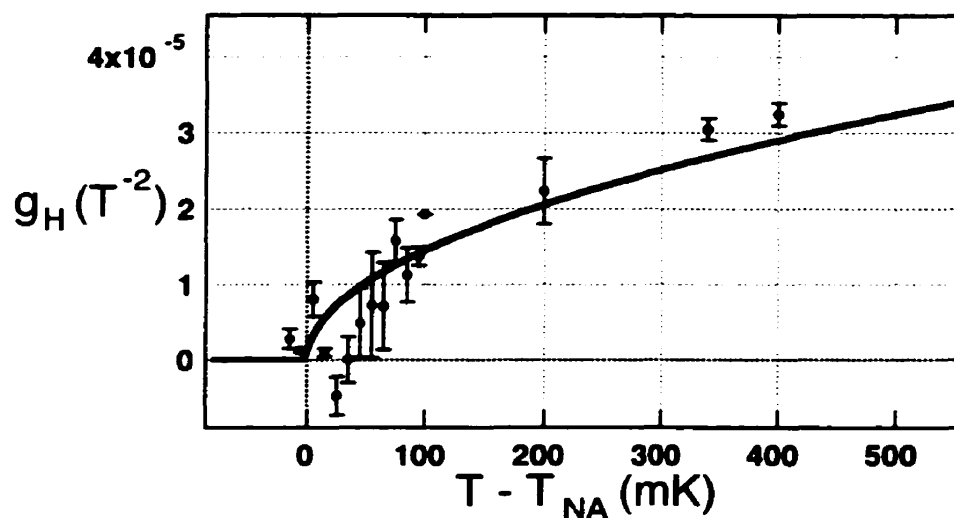


Figure 6.15: In the LTP mixture ( $x = 0.41$ ), the magnetic-field suppression is again a function of temperature, and is consistent with a  $\bar{\nu} = 0.5$  scaling.

dynamical measurements of Cladis *et al.* extended the study all the way to 8CB ( $x = 0$ ), well past the LTP; however, the experimental error bars in that regime were large enough that they make any check on the validity of a fit based on the HLM theory very weak.

We studied the dependence of  $t_0$  on mixture concentration because it provides a handy way of comparing our technique to previous measurements. Moreover, this technique extends the previous HLM curve all the way to pure 8CB. Using the previously determined parameters, we can test for a deviation of the experimental curve from HLM fit form as we probe the more and more weakly first-order region of the phase diagram.

We have already seen the dependence of fluctuations in pure 8CB and in 0.41 mole-fraction 10CB in 8CB (“C04,” the LTP mixture). We also studied mixtures C03 and C02, corresponding to  $x = 0.3$  and  $x = 0.2$  (mole-fraction of 10CB in 8CB).

### 6.5.1 Zero-field results in 8CB-10CB mixtures

The dependence of  $t_0$  on mixture concentration in the 8CB-10CB system between  $x = 0$  and  $x = 0.44$  was then measured. This dependence can be used as an independent measure

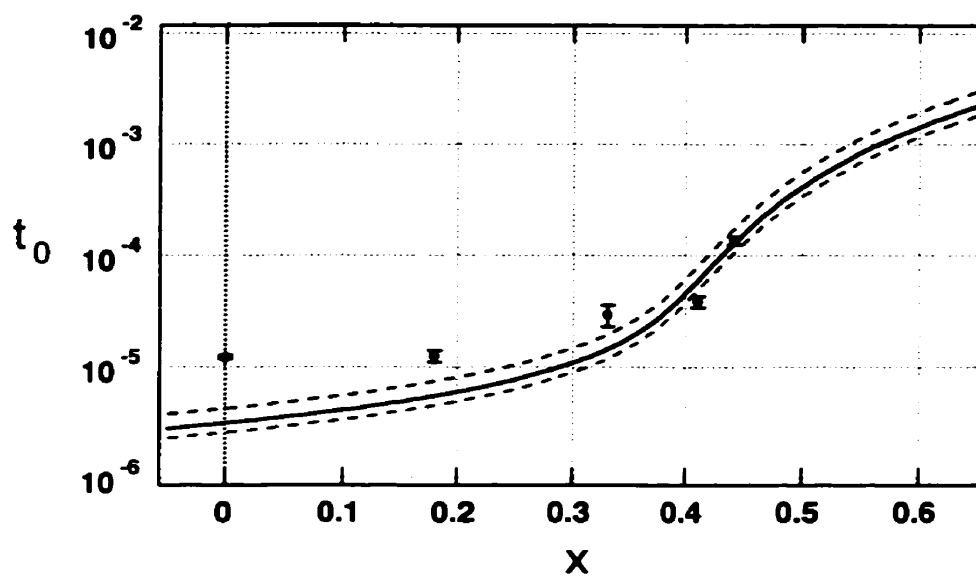


Figure 6.16: Fit of  $t_0$  data (this thesis) to the Anisimov parameters, with  $C_0$  as a fit parameter. The fit to  $t_0$  is based on solution for  $\psi$  at the transition, and equations Eq. B.7 and Eq. B.15. Top and bottom dashed curves show fits to  $t_0$  for  $\bar{\nu} = 0.6$  and  $\bar{\nu} = 0.4$ , respectively. (The data points for these exponent values are not shown.)

$\bar{\nu}$	$C_0$
0.4	$0.74 \pm 0.03$
0.5	$0.79 \pm 0.03$
0.6	$0.88 \pm 0.03$

Table 6.1: Fitted value of  $C_0$  for different choices of the exponent  $\bar{\nu}$  for the data shown in Fig. 6.16.

of the phenomenological Landau parameters.<sup>6</sup> We summarise briefly below.

The earlier fits in Ref. [15] and Ref. [69] determine only 2 of 3 relevant Landau parameters. The fourth parameter is the co-factor of the sixth-order term, and is set to be 1 (in units of  $k_B T/\nu_0$ ). This data in the current study, however, is sensitive to all 3 relevant Landau parameters. Using the previously determined parameters,  $\alpha$  and  $B$ , we can use the third parameter  $C_0$  as a free parameter to fit the data.  $C_0$  is the prefactor to the quartic coefficient, defined by  $C \equiv C_0(x - x^*)$ ; it is negative and should be of order unity.

We use the Anisimov *et al.* parameter set (see Appendix B)

$$\begin{aligned}\beta &= 0.993 \\ \Delta S^*/R &= 0.0261\end{aligned}\tag{6.24}$$

to calculate  $\psi$  and  $A$ , from which we can calculate  $t_0 \equiv A/\alpha$ . We fit for  $C_0$ , while holding  $E = 1$ . The exponent is fixed at  $\bar{\nu} = 0.5$ . The error bars on a free fit without the exponent held are  $\approx 0.1$ . Plotted in Fig. 6.16 is the data for a fitted exponent of  $\bar{\nu} = 0.5$  and the HLM fit to this data. Also shown, for perspective, are HLM fits for data fit to exponents  $\bar{\nu} = 0.4$  and  $\bar{\nu} = 0.6$ . The values of  $C_0$  in the three fits are shown in Table 6.1.

Given a value of  $C_0$  one can then calculate the latent heat corresponding to the discontinuity  $C_0$ . This is shown in Fig. 6.17; shown, too, for comparison is the latent heat data of Marynissen *et al.* [46]. In particular the calculated entropy change per mole for 8CB is

$$\Delta S/R \approx 6 \times 10^{-4}.\tag{6.25}$$

---

<sup>6</sup>A detailed derivation of the fit function based on HLM theory for  $t_0$  vs.  $x$ , where  $x$  is the 10CB mole fraction in 8CB, is given in Appendix B.

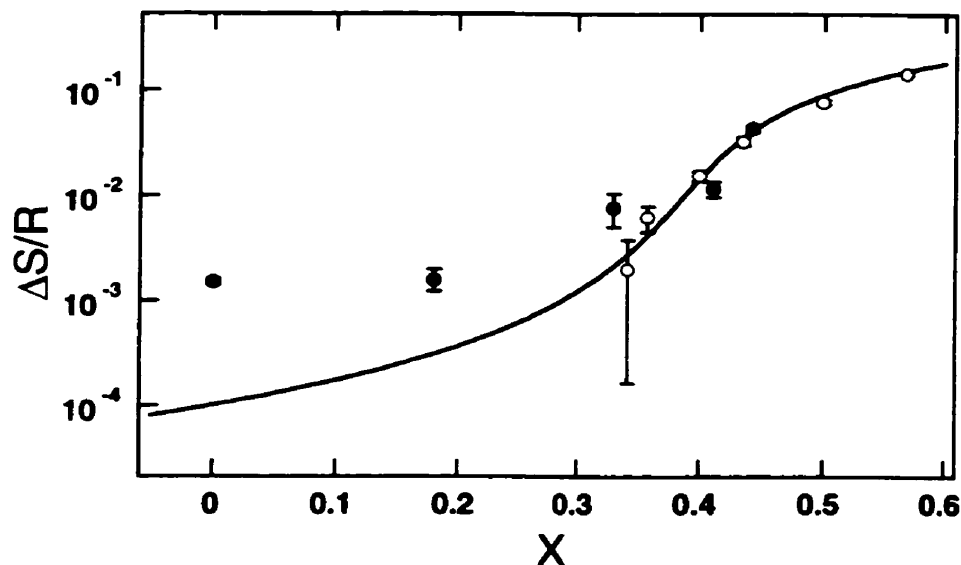


Figure 6.17: Latent-heat estimate based on the fitted Landau parameters. Also shown is the HLM fit and the latent-heat data of Marynissen *et al.* .

## 6.6 A Note on Errors

There is a fundamental distinction between characterising the discontinuity at the phase transition with  $t_0$  as opposed to a latent heat. The fluctuation variance fits a functional form

$$\zeta = w_0 + w_1(T - w_2)^{0.5}, \quad (6.26)$$

where typically  $w_0$ , the smectic baseline, is very close to zero.

Alternatively, we can define

$$h(T) \equiv (\zeta - w_0)^{1/0.5} \quad (6.27)$$

$$= k(T - w_2), \quad (6.28)$$

where  $k = w_1^{1/0.5}$ . For equivalent data sets in different mixtures, the error in the slope is roughly the same; thus the *percentage error* is unchanged for different mixtures. As a result, the absolute error in  $\Delta t_0$  *increases* as  $t_0$  gets larger. In our experiment, the relative error is  $\Delta t_0/t_0 \approx 0.1$ .

In contrast, in the measurement of latent heat, the limitation is an absolute instrumental resolution, and thus the absolute error is constant. This arises from a basic difference in the

analysis: we use the power-law divergence in the nematic to extract the value  $t_0$ . We are thus primarily limited by the range of the fit and not by instrumental resolution. The range of the fit is currently limited by the absence of a theoretical form to account for non-critical contributions to the intensity fluctuations that become important farther away from  $T_{NA}$ .

One advantage with our measuring  $t_0$  is that, being technique independent, the measurements can be supplemented by any other high-resolution technique that measures a power law dependence in the nematic, such as light-scattering, x-ray scattering, or Fréedericks' transition measurements.

## 6.7 Summary of Results

### 6.7.1 Zero-field Results in 8CB

We have designed a new experimental technique to study fluctuation effects at the NA transition. With this technique we probe the order of the transition in 8CB. We find the transition to be clearly *first order*, with a discontinuity in fluctuations  $t_0 = 1.2 \pm 0.1 \pm 0.4 \times 10^{-5}$  (where the first errors refer to the statistical errors in analysing a single sample, while the second refers to systematic variations from one sample to another).

### 6.7.2 Zero-field Results in 8CB-10CB mixtures

We can alter the fourth-order Landau coefficients by using binary mixtures 8CB and 10CB. The discontinuity gets larger as we approach the Landau tricritical point. In particular, we find that the data near the LTP agree with the HLM prediction for reasonable values of the quartic coefficient  $C_0$ . However, for lower concentrations of 10CB in 8CB, there is a clear deviation from the HLM prediction. This suggests that the HLM theory *underestimates* the latent heat in this region of the phase diagram. This is a bit surprising, given the expectation that the  $B$  term, which is induced by director fluctuations, should get smaller with increasing nematic range. However, given that the physics in this region of the phase diagram is rather complex, we defer this question until further theoretical study.

The exponent of the power law  $\bar{\nu}$  in all cases was held fixed to  $\bar{\nu} \approx 0.5$ , which was close to the value obtained from a free fit. However, in a free fit, there was always an uncertainty of  $\approx \pm 0.1$  in the value of  $\bar{\nu}$ . Forcing the fits with an exponent  $\bar{\nu} = 0.4$  and

Concentration $X$	$t_0$
0	$1.21 \times 10^{-5} \pm 0.10 \pm 0.4$
0.18	$1.24 \times 10^{-5} \pm 0.15 \pm 0.4$
0.33	$2.9 \times 10^{-5} \pm 0.6 \pm 0.4$
0.41	$3.8 \times 10^{-5} \pm 0.4 \pm 0.4$
0.44	$13.6 \times 10^{-5} \pm 1.1 \pm 0.4$

Table 6.2:  $t_0$  for different mixture concentrations, with a fitted exponent  $\bar{\nu} = 0.5$ . The errors quoted are tolerances for one sample, and systematic variations from sample to sample. The latter error does not affect the magnetic field measurements.

$\bar{\nu} = 0.6$  systematically *reduces* and *increases* the value, respectively, of  $t_0$  for all samples. The magnitude of this variation due to choice of exponents is shown by the dashed lines in Fig. 6.16. The qualitative nature of the dependence described above is, however, unchanged: the one fit parameter  $C_0$ , does not allow us to change the *shape* of the HLM fit, there is still a qualitative and systematic disagreement between the HLM fit and the data.

These experimental results are fairly robust and suggest an unambiguous deviation from both the deGennes-McMillan form and HLM theory. Given that  $t_0$  for the mixtures could be determined by other techniques, it would be interesting to see other  $t_0$  measurements on the 8CB-10CB system.

### 6.7.3 Magnetic-Field Studies

We have measured the effect of a magnetic field in pure 8CB, in the C02 mixture (0.18 mole fraction 10CB in 8CB) and the LTP mixture. In none of these samples do we observe a suppression of fluctuations close to  $T_{NA}$ .

The theoretical predicted critical field to drive the transition second-order in 8CB is  $H_c \approx 10$  T. This critical field implies a depression of  $t_0$  by 30% at 1.5T. This depression is something clearly within the reach of this technique. With our technique, we can unambiguously measure a depression as small as 10%. This sets a bound on the critical field, in all the experiments, of  $\gtrsim 30$ T.

In the C02 mixture (0.2 mole-fraction 10CB in 8CB), as well, there is no field effect on the critical behaviour, with the lower bound on the critical field, once again, being set by

30 T.

For the LTP mixture, we found theoretically in Chapter 3 that the critical field calculated from the field-HLM mechanism is 300 T. In this case, our experiments, which again set a lower bound of 30 T on the critical field, are weakly consistent with theory, but, clearly, one must go to much larger fields to test this prediction.

We emphasise that we do, however, measure the expected non-critical magnetic field effect, the suppression of the fluctuations in the nematic phase. The suppression of the variance goes as  $H^2$ , as expected. The coefficient of this field suppression,  $g_H$ , displays a temperature dependence that is consistent with a critical divergence with a power law  $\bar{\nu} = 0.5$ . This, in turn, is internally consistent with our zero-field results.

#### 6.7.4 Thickness Studies

The dependence on thickness yielded two results: First, there was no decrease in  $t_0$  with decreasing thickness. A decrease was expected because the anchoring field should also have the effect of suppressing fluctuations. This was not observed; instead, a dramatic *increase* in  $t_0$  was observed for extremely small thickness ( $0 < d < 2.5 \mu\text{m}$ ). We explain this effect by conjecturing that a very small degree of twist could, at small thicknesses, have a measurable effect on the phase transition discontinuity. An order-of-magnitude estimate suggests that this conjecture is indeed plausible. A more systematic test would entail using substantially larger twists—since the wedge sample was prepared in order to observe a completely different effect, we were attempting to minimise the twist angle. This result is also of note from the point of view of the NA transition as it implies that with experiments done at the NA transition with thin samples ( $d \lesssim 5 \mu\text{m}$ ) one must be cautious in the interpretation of an observed discontinuity.

Second, for larger thickness, there was no systematic variation in  $t_0$ . This confirms that there is no effect of thickness on our other measurements.

## Chapter 7

# CONCLUSIONS AND FUTURE DIRECTIONS

Fluctuation effects at the NA transition have previously been studied in mixtures of liquid crystals. Mean-field effects of electric and magnetic fields have also been studied quite extensively. In this thesis, we have for the first time studied the effect of a magnetic field on fluctuations at the NA transition. The effect of a field allows one to probe the parameter dependence of thermodynamic quantities without changing the materials, the techniques, the experimental set-up, or indeed, the sample and its positioning. The critical phenomena at the NA transition have proved to be quite sensitive to changes in these experimental parameters, and the scatter in different experimental results is rather large. In this study, for example, we found that sample thickness was a relevant parameter for extremely thin samples.

Two main results arise out of this thesis, and both constrain theories in the weakly type-1 region of the NA transition. The first is the absence of a magnetic field effect on the critical behaviour in pure 8CB, and in the “C02” and “LTP” mixtures (0.2 and 0.4 mole fraction 10CB in 8CB, respectively). We predicted in Chapter 3 within the Halperin-Lubensky-Ma formalism that an external field would suppress nematic director fluctuations and drive the transition back to second order. Experimentally, we see a non-critical suppression of the fluctuations but observe no change in the critical behaviour. In particular, the strength of the first-order transition, measured by the dimensionless number  $t_0$ , is unchanged. We

thereby establish a lower bound of 30 T on the critical magnetic field. We expected the critical field to be around 10 T in 8CB and only marginally higher in the C02 mixture. In both cases, therefore, our experiments disagree with HLM predictions. This implies that the neglect of smectic fluctuations is clearly not valid in this region of the phase diagram. At the Landau tricritical point (LTP), which is in the strongly type-1 region, the HLM prediction suggests a substantially larger critical field of 300T, and our null measurement implies that the critical field exceeds 30 T. Thus, we have not tested for the “field HLM” effect in LTP mixtures, and that remains an open problem.

Second, the variation of  $t_0$  in mixtures has yielded the surprising result that  $t_0$  on the weakly first-order side of the LTP is larger than the HLM predicted value, and not smaller. This result puts a strong constraint on any theory of the tricritical point.

In addition, for thin samples ( $d < 2.5 \mu\text{m}$ ), we find that it is likely that twist is always an important experimental consideration at the NA transition.

There are some broad themes for future work. First, the external field can be used to shed light on the nature of the critical behaviour at the NA transition. We have seen (Chapter 3) that an external field can affect a *qualitative feature* of the NA transition, that of phase transition order. Since a field changes the symmetries of the system by imposing a preferred direction, it could also change the critical exponents at the phase transition. This is an important point to pursue in the future, because the presence of an external field is implicit in most experiments (via the anchoring field), yet its effects have not been explicitly studied. Moreover, in the type-2 limit where the NA transition should be second order, the theoretical expectation is that, regardless of the nature of the zero-field NA transition, applying a field should be a relevant perturbation that changes the universality class of the transition to the usual 3DXY class. It would be very interesting to probe the experimental consequences of this crossover to the 3DXY fixed point.

One such consequence would be the suppression of spatial anisotropy in the critical region. The Patton-Andereck [43] model predicts a broad, weakly anisotropic crossover between an isotropic, high-temperature region and a strongly anisotropic, low-temperature region. They contend that experiments probe only the weakly anisotropic region, the strongly anisotropic region being experimentally inaccessible. It would be interesting to incorporate a magnetic field in their model, to study the effect of the field on the crossover regime.

In addition to the broad issue of tweaking fluctuation effects with external fields, there

are numerous other avenues that are promising:

1. The much higher critical field at the LTP can be accessible with a combination of better temperature control and a heftier magnet. In 8CB, it would be interesting to see the effect of an order-of-magnitude increase in the applied magnetic field. Unfortunately, larger magnetic fields are usually available only in solenoidal magnets, while our experiment was designed for a transverse-bore magnet. Although there is no reason that one cannot design an experiment to work in a solenoidal magnet, the present apparatus probably cannot be modified to do so. An entirely new design is needed.
2. It is possible that multiple scattering effects can be avoided by adapting a more two-dimensional imaging technique, such as confocal scanning microscopy. This would allow for easier interpretation of the signal and would also allow an increase in the temperature range of usable data.
3. The electric-field version of the HLM effect would also be interesting. The challenge here is to achieve sub-milliKelvin temperature control in a system where one is periodically pulsing heat in the form of electric-field-induced heating.
4. Another interesting project (discussed earlier in a footnote in Section 2.1.9) is the NA transition with the nematic director confined to two dimensions. Here, fluctuations effects are predicted to be stronger [45]; experimentally this could be achieved with a material of negative dielectric (diamagnetic) anisotropy so that the director is confined to the plane perpendicular to the field direction. For the electric fields of  $30 \text{ V}/\mu\text{m}$  achieved by Lelidis and Durand [54], the electric coherence length  $\xi_E \approx \sqrt{\pi K/(\Delta\epsilon)E^2} \approx 20 \text{ nm}$ . The effects of planar anisotropy would be felt when the correlation length exceeds this 20 nm length-scale.
5. The effect of a small amount of twist could perhaps be used as a technique to improve signal to noise at the NA phase transition. It can be a tool to increase sensitivity in an optical technique only if it has no qualitative effect on the nature of the phase transition. It is plausible that it could have a qualitative effect because of the change of symmetry between the nematic and the twisted nematic. This problem deserves more attention.

6. We designed this apparatus for temperature stability and for control of the direction of the temperature gradients. While we achieved the desired temperature stability, there were moderately large unintended gradients in the plane transverse to the applied temperature gradient. Both were due to the large thermal mass of the glass blocks that made up the sample. Since the temperature stability was better than we needed for this experiment, we could in retrospect have designed the system with shorter time constants and improved our control of the temperature gradients at the expense of stability.
7. Systematic errors in the fluctuation normalisation restricted the temperature range of the measurements made in this thesis to roughly 0.1 K. A better theoretical understanding of these non-critical optical effects could allow experimenters to extend the range upwards relatively easily.
8. A more challenging, yet feasible project, would be to increase the temperature stability by at least another order of magnitude. This would allow more direct confrontation with the predictions made by the Patton-Andereck theory. In particular, one needs a very large temperature range to test the predictions of this theory, because it predicts a change in the critical exponents as a function of temperature. Experimentally, this is a tall order because it increases the number of free parameters in the fit.
9. Finer temperature control could also be of use in the studies of the layer-compression modulus, discussed in Section 2.2.4. Here, an experimental observation indicating the finiteness of  $B$  at the NA transition was reported [62], but more recent experiments [64] have suggested that these results are incorrect and show instead that  $B$  obeys a power-law up to the resolution of the experiment ( $\approx 1$  mK). However, the Landau-Peierls argument given in Section 2.2.4 suggests that a saturation of  $B$  should be observed at smaller reduced temperatures. This would be interesting to observe.
10. No numerical simulations have been done at the nematic-smectic-A tricritical point. The Bartholomew simulation [44] was done for the superconducting free energy, without the splay term, while the Dasgupta simulation [47] was done with the splay term but in the strongly type-2 limit. Moreover, the recent advances in simulation system sizes could improve on the results of these decade-old simulations. The addition of a

magnetic field to these simulations would again be an interesting project.

At this point, we have arrived at the end of my studies of the nematic–smectic-A phase transition. As remarked several years ago by de Gennes and Prost [2]: “It seems that we almost understand, but not quite.”

## Appendix A

# 8CB MATERIAL PARAMETERS

It is useful to know the material parameters of the liquid crystal 8CB, as these parameters played a major role in all the estimates and order-of-magnitude calculations that aided in the design of the experiment. These data were gleaned from several sources. The references [142, 143, 144, 135, 145, 146, 147, 72, 99, 148, 77, 149, 65, 150], in particular, were useful. In what follows, we reproduce data on the physical properties on 8CB and 10CB, and more detailed temperature dependence of the elastic constants and X-ray correlation lengths of 8CB.

### A.1 Structure and Properties of 8CB and 10CB

8CB exhibits a nematic and a smectic –  $A_d$  phase. 10CB has an alkyl chain that is longer by two units, and a direct isotropic–smectic-A transition, with no intervening nematic phase. Table A.1 shows the phase sequence for 8CB and 10CB. Fig. A.1 shows their chemical structures; the cyanobiphenyl group is the rigid part of the molecule, while the alkyl chain is the flexible part. The longer the flexible chain, the more favoured is the smectic phase.

8CB	Isotropic	$\xrightarrow{40.5^\circ\text{C}}$	Nematic	$\xrightarrow{33.5^\circ\text{C}}$	Smectic – A	$\xrightarrow{21.5^\circ\text{C}}$	Solid
10CB	Isotropic	$\xrightarrow{50.5^\circ\text{C}}$	Smectic – A	$\xrightarrow{44^\circ\text{C}}$	Solid		

Table A.1: Phase sequence in 8CB and 10CB.

The smectic- $A_d$  phase is a partial-bilayer smectic, with the layer spacing,  $d \approx 3\text{nm}$ , being roughly 35% larger than the molecular length. The mass density of 8CB is  $\rho \approx 0.98\text{ g/cc}$ .

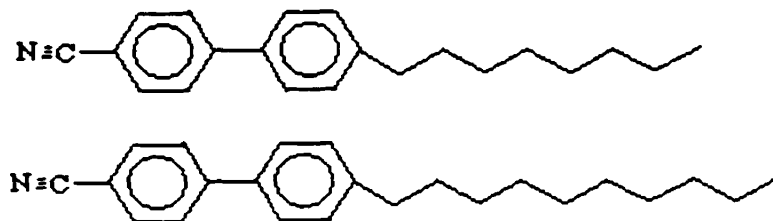


Figure A.1: Chemical structure of 8CB and 10CB, both cyanobiphenyls, with the aliphatic-chain made up of 8 and 10 carbon atoms, respectively.

## A.2 8CB-10CB Phase Diagram

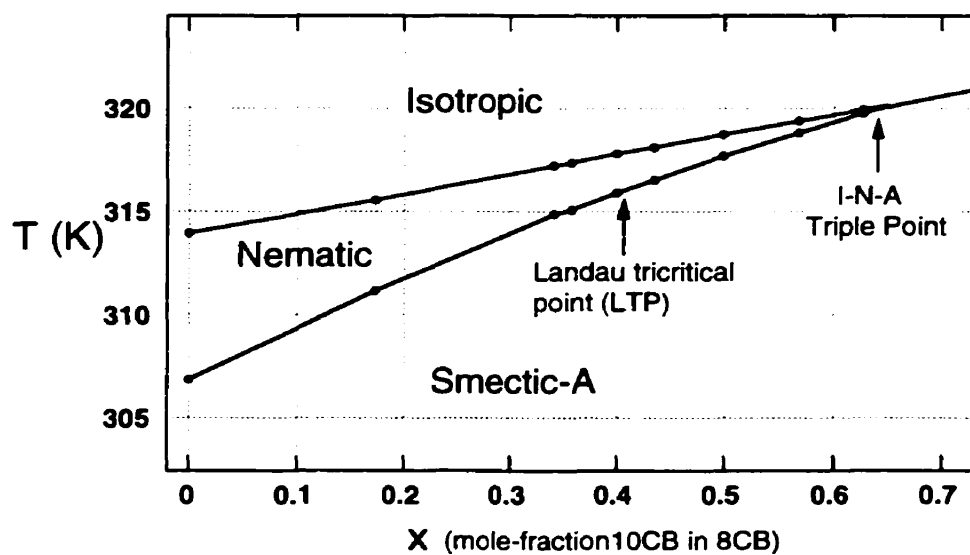


Figure A.2: 8CB-10CB phase diagram (from data in Ref. [46]).

### A.3 Temperature dependence of Elastic constants and Correlation Lengths

A number of temperature-dependent 8CB material parameters are reproduced here for reference. They are:

1. X-ray correlation lengths (Fig. A.3)
2. Elastic constant measurements (Fig. A.4).
3. Measurements of the nematic order parameter magnitude  $S$ , the dielectric anisotropy  $\Delta\epsilon$ , the diamagnetic anisotropy  $\Delta\chi$  (Figures A.5, A.5, and A.7).
4. Measurements of the thermal conductivity and thermal diffusivity (Figures A.8 and A.9).

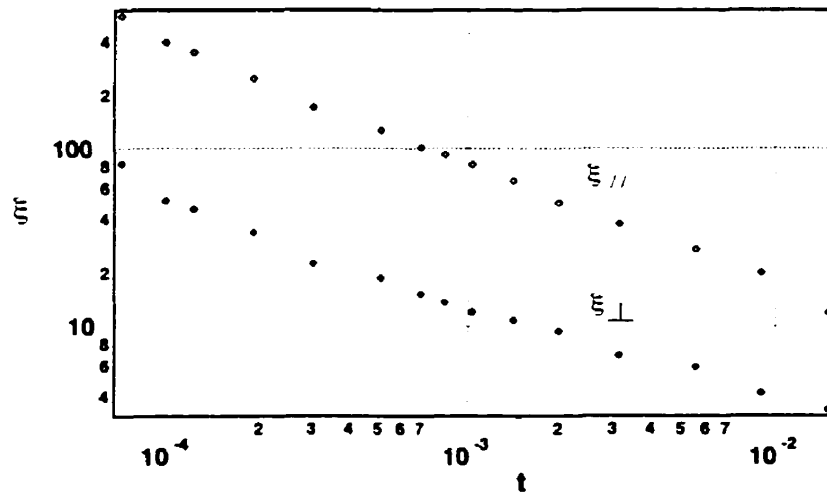


Figure A.3: High-resolution x-ray scattering study of correlation lengths  $\xi$  vs.  $t$  (Ref. [144]). The top curve is  $\xi_{||}$  and the bottom one is  $\xi_{\perp}$ .

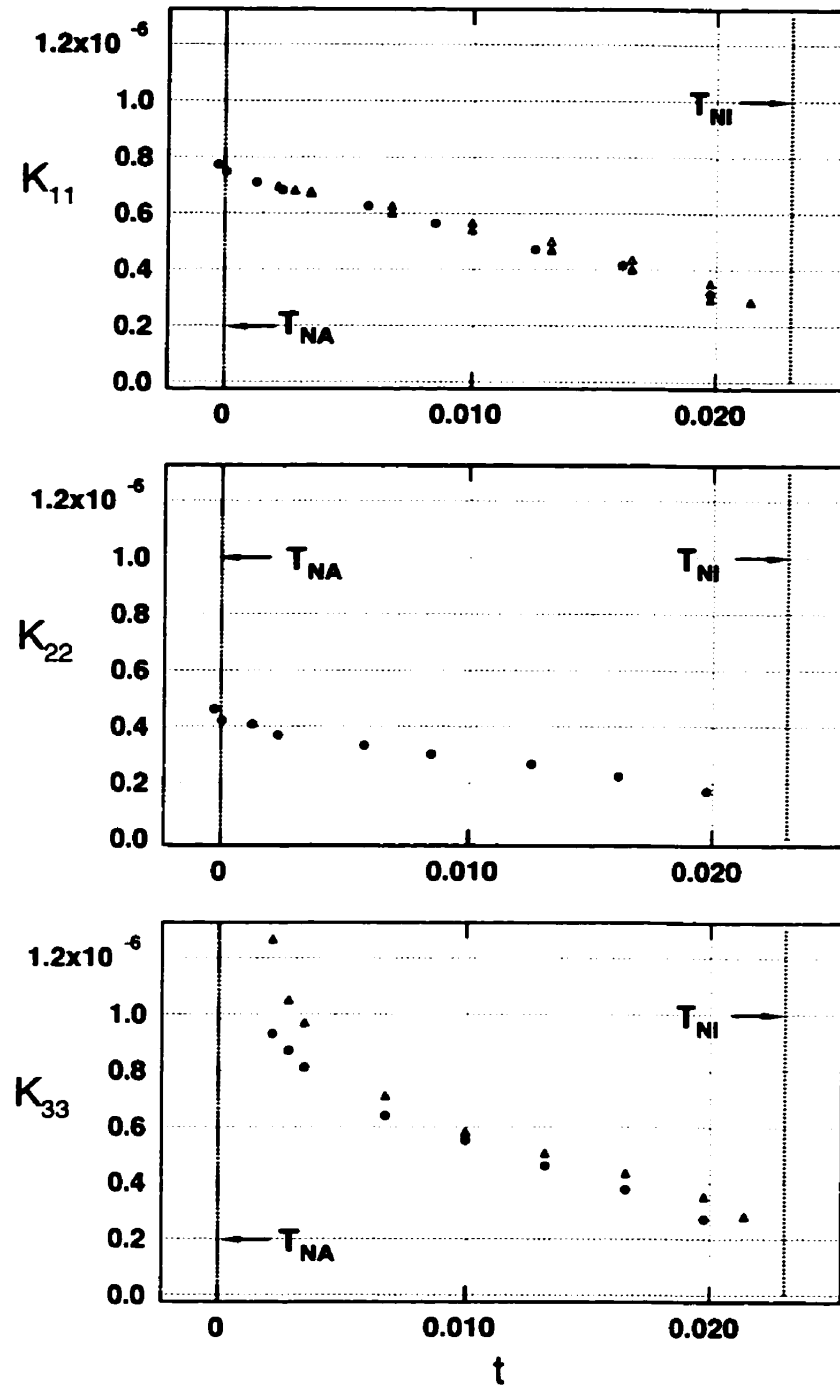


Figure A.4: Temperature dependence of  $K_{33}$  vs.  $t$  (Ref. [142, 143]). The two sets of data points in the top and bottom graphs correspond to different experiments.

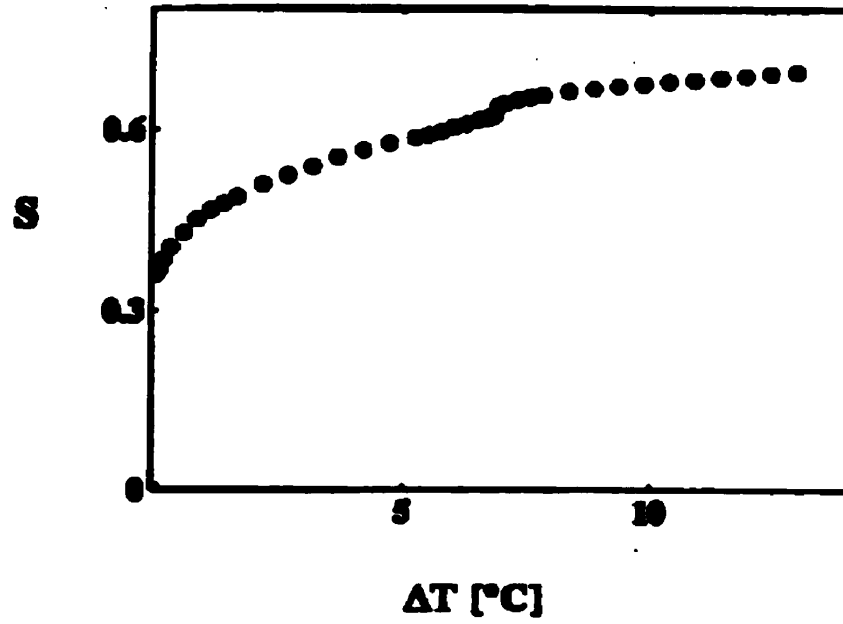


Figure A.5: Temperature dependence of  $S$  vs.  $\Delta T \equiv T_{IN} - T$ . (Ref. [77]).

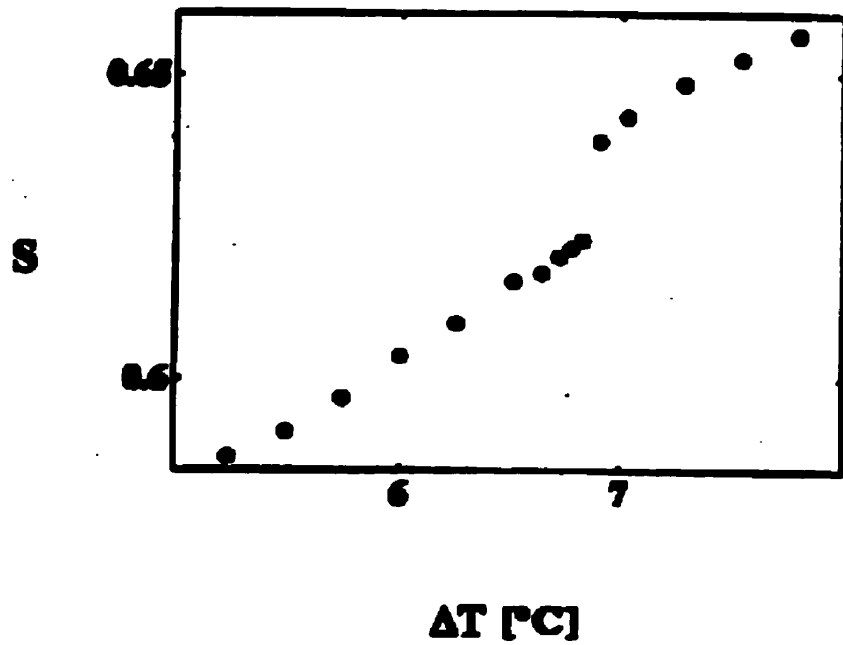


Figure A.6: Temperature dependence of  $S$  vs.  $\Delta T \equiv T_{IN} - T$  (close to  $T_{NA}$ ). (Ref. [77]).

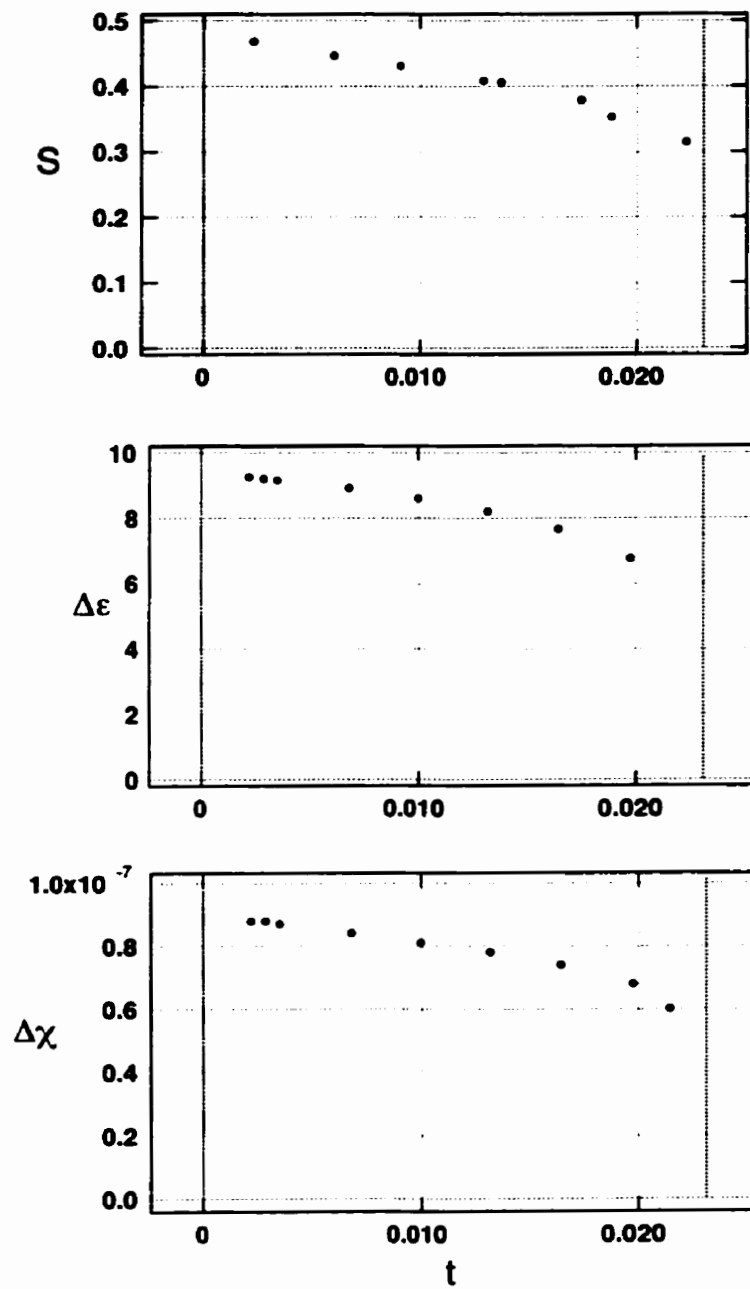


Figure A.7: Temperature dependence of  $S$ ,  $\Delta\epsilon$ , and  $\Delta\chi$  vs. reduced temperature  $t = (T - T_{NA})/T_{NA}$  (Ref. [135]).

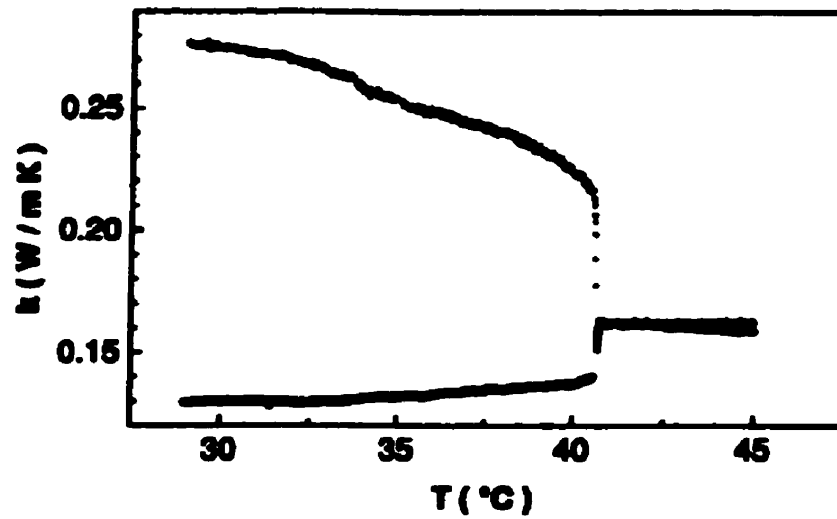


Figure A.8: Thermal conductivity vs. Temperature (Ref. [99]): data from homeotropic sample is gray, while planar sample is dark.

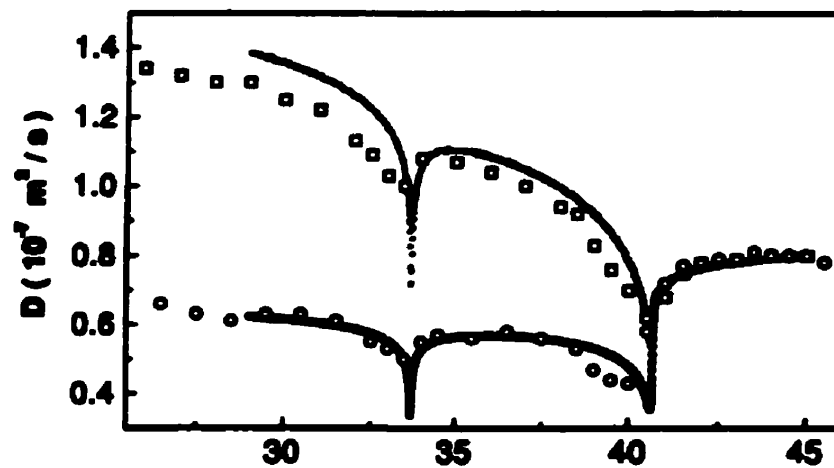


Figure A.9: Thermal diffusivity vs. Temperature (Ref. [99]): data from homeotropic sample is gray, while planar sample is dark.

## Appendix B

# LANDAU THEORY ESTIMATES

### B.1 Introduction

In Landau theory, the coefficient of each term is a phenomenological parameter. Comparing Landau parameters from different experiments is a useful way of checking that they give us a consistent description of the underlying physics. Four sets of measurements that yield direct or indirect information on the Landau parameters have been made in the 8CB-10CB system. They are the latent-heat data of Marynissen and coworkers [46], the front-velocity measurements of Cladis and coworkers<sup>1</sup>, the capillary-length measurements by Tamblyn *et al.* [69], and the electric field studies of Lelidis and Durand [77]. In this appendix, we outline the relationship of  $t_0$ , measured in our experiment, to the Landau parameters. The experimentally determined Landau parameters in the four other experiments are also presented.

We start with the free energy

$$F = \frac{1}{2}A\psi^2 - \frac{1}{3}B\psi^3 + \frac{1}{4}C\psi^4 + \frac{1}{6}E\psi^6, \quad (\text{B.1})$$

We can write  $A = \alpha t$ ,  $t = (T - T^*)/T^*$  being the reduced temperature. The quartic term  $C$  changes sign at the LTP; close to the LTP, we can write

$$C = C_0 \cdot (x - x^*), \quad (\text{B.2})$$

---

<sup>1</sup>The data from these two measurements were re-analysed in Ref. [15].

where  $x$  is the mole-fraction of 10CB, with a value  $x^*$  at the LTP. Since the HLM theory ignores smectic fluctuations, the temperature dependence of the cubic coefficient,  $B$ , in this approximation is contained entirely in its linear  $k_B T$  dependence. This temperature dependence is weak:  $k_B T$  changes by less than 3% over the entire nematic range, and can thus be assumed to be a constant. In the absence of special circumstances, all Landau parameters should be of the order  $k_B T/v_0$ , where  $v_0$  is a molecular volume. The results are least sensitive to variations in  $E$ , and thus it is reasonable to take  $E \approx 1$  (in units of  $k_B T/v_0$ ).<sup>2</sup> The typical procedure is to express experimentally obtained quantities in terms of  $\alpha, B$  and  $C_0$ .

### B.1.1 Latent-heats

The latent heat is most conveniently measured in units of  $RT_{NA}$ , where  $R$  is the universal gas constant;  $R = 8.3144 \text{ J}/(\text{K}\cdot\text{mole})$ , and  $T_{NA} \approx 319\text{K}$  (the appropriate value for  $T_{NA}$  is used for each mixture). We can derive, in mean-field theory, the dependence of the latent heat on the Landau parameters. Starting from the Landau free energy, we look for the non-trivial  $\psi \neq 0$  solution to the simultaneous equations  $f = 0$  and  $\frac{df}{d\psi} = 0$ . The NA transition point occurs when the  $\psi = 0$  and the  $\psi \neq 0$  solution, have the same free energy. We can thus write

$$\begin{aligned} 0 = \frac{1}{\psi^2} f &= \frac{1}{2}A - \frac{1}{3}B\psi + \frac{1}{4}C\psi^2 + \frac{1}{6}E\psi^4 \\ 0 = \frac{1}{\psi} \frac{df}{d\psi} &= A - B\psi + C\psi^2 + E\psi^4 \end{aligned} \quad (\text{B.3})$$

Eliminating  $A$ , one gets the cubic equation

$$\psi^3 + \left(\frac{3C}{4E}\right)\psi - \frac{B}{2E} = 0 \quad (\text{B.4})$$

This cubic equation is solved by reading off the solution from a book on mathematical tables [151], setting  $q = \frac{1}{3}\left(\frac{3C}{4E}\right) = \frac{C}{4E}$ , and  $r = -\frac{1}{2}\frac{B}{2E} = \frac{B}{4E}$ , and  $q_r = (q^3 + r^2)$ . The equation has one real root for  $q_r > 0$ , and 3 real roots for  $q_r < 0$ . Examining the real root for  $q_r > 0$ , one finds the following solution:

$$\psi = \left[ \frac{B}{4E} + \sqrt{\left(\frac{C}{4E}\right)^3 + \left(\frac{B}{4E}\right)^2} \right]^{\frac{1}{3}} + \left[ \frac{B}{4E} - \sqrt{\left(\frac{C}{4E}\right)^3 + \left(\frac{B}{4E}\right)^2} \right]^{\frac{1}{3}}. \quad (\text{B.5})$$

<sup>2</sup>Replacing with the value  $E = 2$  changed the fitted values of  $t_0$  by *approx*10%.

For  $C \gg B$ ,  $\psi = 0$ . When  $q_r \leq 0$ , there are now 3 real roots, but by continuity the root is the same one as for  $q_r > 0$ . The root now seems to be complex but is in fact real. Setting  $i\Delta = \sqrt{(\frac{C}{4E})^3 + (\frac{B}{4E})^2}$ , one finds, after some manipulation, that

$$\psi = 2(r^2 + \Delta^2)^{\frac{1}{6}} \cos \left[ \frac{1}{3} \tan^{-1} \left( \frac{\Delta}{r} \right) \right]. \quad (\text{B.6})$$

Now, going back to Eq. B.4, one gets, by eliminating  $E$ :

$$A = \frac{-C}{4}\psi^2 + \frac{B}{2}\psi. \quad (\text{B.7})$$

The quantity  $\Delta S \equiv \frac{L}{T}$  is simply the entropy change associated with the phase transition; it can therefore be related to the free energy:

$$\frac{\Delta S}{R} = \frac{df}{dt} = \alpha\psi^2 = (A/t_0)\psi^2. \quad (\text{B.8})$$

One nominally needs 4 parameters to specify  $\frac{\Delta S}{R}$ :  $B, C, E$ , and either  $\alpha$  or  $t_0$ . In this analysis we take  $E = 1$  (in units of  $k_B T/v_0$ ).  $C_0$  and  $\alpha$  (in units of  $E$ ) would typically be of order unity. However, Anisimov *et al.* [80] have argued that when the smectic phase is closely spaced in temperature to the isotropic phase, smectic fluctuations have the effect of renormalising these bare parameters so it is essential not to make any assumptions about these parameters and fit them to the data.

Anisimov *et al.* [15] found a way of reducing the number of required parameters to two, by normalising the latent heat with the corresponding value at the LTP. Thus a theoretical parameter is traded for an experimentally measured quantity. Thus their fitting form was<sup>3</sup>

$$\left[ \frac{\Delta S}{\Delta S^*} \right] - \left[ \frac{\Delta S}{\Delta S^*} \right]^{-1/2} = \frac{\beta R}{\Delta S^*} (x - x^*), \quad (\text{B.9})$$

where  $\beta = -\frac{3}{8}(\alpha C_0/E)$ . Hence, the experimental parameters extracted from the latent heat data on the 8CB-10CB system are[15]

1.  $\beta = -\frac{3}{8}(\alpha C_0/E) = 0.993$
2.  $\Delta S^*/R = 0.0261$ .

Note (Fig. B.1) that the position of the LTP,  $x^* = 0.42$ , is deduced from the linear part of the data.

---

<sup>3</sup>The parameter  $\beta$  here corresponds to  $\alpha$  in Ref. [15].

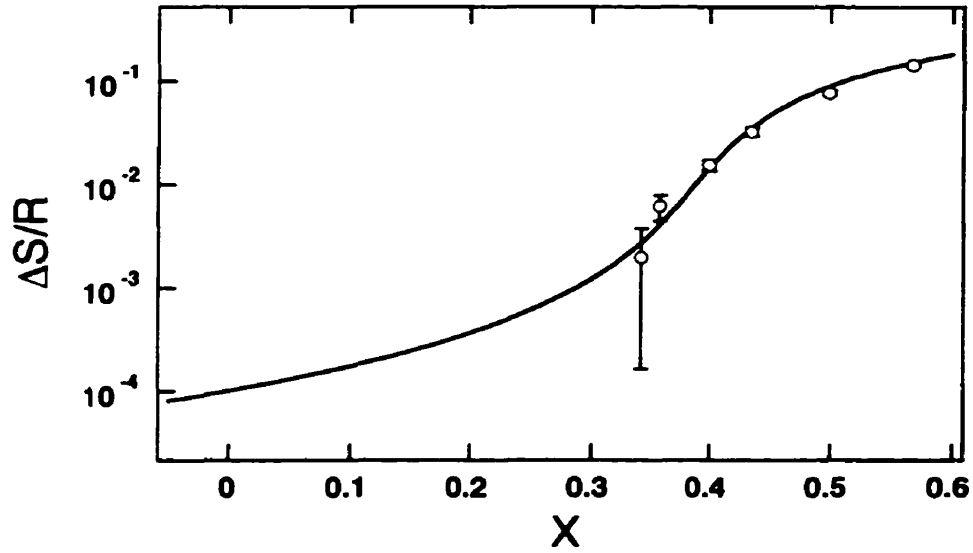


Figure B.1: Fit of latent heat data of Ref. [46] to the Anisimov parameters, which is based on an effective mean field free energy with a negative cubic term that has a constant coefficient  $B$ .

### B.1.2 Front Velocity

Front velocity measurements are in principle more sensitive than adiabatic calorimetry, because, as mentioned earlier in Section 5.2, driving a system slightly out of equilibrium is often a very sensitive way of measuring equilibrium properties. However, to translate the functional dependence of the front velocity into a form purely dependent on the Landau parameters, one must also measure the coherence length at the transition. This adds uncertainty, as the coherence-length measurements are typically obtained from independent experiments such as X-ray scattering, and the consistency of mixture preparation is not guaranteed. Moreover, the coherence lengths are intrinsically anisotropic, and which coherence length to use is unclear.

A more accurate method is to use the experimental parameters obtained from the latent heat data in order to extend the fit to the unprobed region between mole fractions  $x = 0$  and  $x = 0.3$ . The data fall roughly on the Anisimov *et al.* fit, *with no additional fit parameters*; however, near  $x = 0$  (i.e. pure 8CB) there is considerable deviation from the HLM-inspired fit. The larger experimental error in this region, however, prevents one from drawing any strong conclusions from this deviation.

### B.1.3 Capillary Length

The capillary-length measurements of Tamblyn *et al.* [69] were also used to determine the parameters  $\beta$  and  $\Delta S^*/R$ , previously determined from latent heat measurements. Thus they provide an independent measure in the same region. Unfortunately, this technique could not be extended to the limit of pure 8CB. The authors determined the experimental parameters to be

1.  $\beta = -\frac{3}{8}(\alpha C_0/E) = 1.2 \pm 0.2$ .
2.  $\Delta S^*/R = 0.020 \pm 0.005$

### B.1.4 Electric Field Studies

Lelidis and Durand [54] determined the values for the quadratic and quartic Landau coefficients from electric field studies in a mixture of 0.75 (mole fraction) 10CB in 8CB. The determined values (in our notation) were:

$$\begin{aligned}\alpha &= 0.115 \times 10^7 \text{ erg/Kcm}^3 \times T^* \\ &= 3.68 \times 10^8 \text{ erg/cm}^3\end{aligned}\tag{B.10}$$

$$C(x = 0.75) = 0.35 \times 10^7 \text{ erg/cm}^3\tag{B.11}$$

$$\tag{B.12}$$

This unusually large value of  $\alpha$  is related to a correspondingly large estimated value of  $\psi_0 = 0.58$  at the transition. The two are related simply:

$$\alpha = 2L/\psi_0^2\tag{B.13}$$

Using the latent heat value of  $\approx 2.83$  kJ/mole for the isotropic-smectic-A transition in an 10CB and  $\psi_0 = 0.58$ , gives a self-consistent value for  $\alpha$ :

$$\alpha = 5.44 \times 10^8 \text{ erg/cm}^3\tag{B.14}$$

That this large value of  $\alpha$  is in fact consistent with a smaller value of  $\alpha$  near the LTP is evidenced by the fact the  $\psi_0$  itself increases sharply for  $0.6 < x < 1$  in the 8CB-10CB system. Experimental measurements of  $\psi_0$  in these mixtures would help clarify this issue.

### B.1.5 Intensity Fluctuation Microscopy

In our own data analysis, we use the experimental fit parameters from Section B.1.1 [15] to compare our data with HLM theory. A fit for  $t_0$  is determined from Eq. B.7 by putting

$$t_0 = A/\alpha. \quad (\text{B.15})$$

Since one can calculate both  $t_0$  and  $\Delta S^*/R$  from Landau parameters  $\alpha$ ,  $B$ , and  $C_0$ , ( $E = 1$ ), direct comparison can be made with one set of parameters to both the latent heat data of Ref. [46] and the  $t_0$  data from this thesis. The dependences of  $t_0$  and the entropy change per mole  $\delta S/R$  as a function of mixture concentration are shown in Chapter 6. (See Fig. 6.16 and 6.17.) The fit to the latent heat is independent of the value of  $C_0$ , while the  $t_0$  fit is not. Thus, in our fit, we use  $C_0$  as a free parameter. The HLM theory is expected to be valid close to the LTP; we can then look for deviations from HLM theory as  $x \rightarrow 0$ .

# Bibliography

- [1] P. Collings, *Liquid Crystals: nature's delicate phase of matter*, 1st ed. (Princeton University Press, Princeton, 1992).
- [2] P. G. de Gennes and J. Prost, *The Physics of Liquid Crystals*, 2nd ed. (Clarendon Press, Oxford, 1993).
- [3] S. Chandrasekhar, *Liquid Crystals*, 2nd ed. (Cambridge University Press, Cambridge, 1992).
- [4] W. H. de Jeu, *Physical properties of liquid crystalline materials*, 1st ed. (Gordon and Breach, Amsterdam, 1980).
- [5] S. Fraden, "Phase Transitions in Colloidal Suspensions Of Virus Particles," in *Observation, Prediction, and Simulation of Phase Transitions in Complex Fluids*, M. Baus, L. F. Rull and J. P. Ryckaert, ed., (Kluwer Academic Publishers, 1995), pp. 113 – 164.
- [6] Arun Yethiraj, private communication.
- [7] C. W. Oseen, "The Theory of Liquid Crystals," *Trans. Far. Soc.* **29**, 883–899 (1933).
- [8] H. Zöcher, "The Effect of a Magnetic Field on The Nematic State," *Trans. Far. Soc.* **29**, 945–957 (1933).
- [9] F. C. Frank, "On the Theory of Liquid Crystals." *Disc. Far. Soc.* **25**, 19–28 (1958).
- [10] W. G. Bouwman and W. H. de Jeu, "Critical behaviour of the nematic to smectic A phase transition," in *Modern Topics in Liquid Crystals*, Agnes Buka, ed., (World Scientific Pub. Co. Pte. Ltd., Singapore, 1993), pp. 161 – 186.

- [11] K. G. Wilson, "Renormalization Group and Critical Phenomena. I Renormalization Group and the Kadanoff Scaling Picture," *Phys. Rev. B* **4**, 3174 (1971).
- [12] N. Goldenfeld, *Lectures on Phase Transitions and the Renormalization Group*, 1st ed. (Addison-Wesley, Reading, 1992).
- [13] P. Pfeuty and G. Toulouse, *Introduction to the Renormalization Group and to Critical Phenomena*, 1st ed. (Wiley-Interscience, Chichester, 1978).
- [14] B. I. Halperin, T. C. Lubensky, and S. K. Ma, "First-Order Phase Transitions in Superconductors and Smectic-A Liquid Crystals," *Phys. Rev. Lett.* **32**, 292–295 (1974).
- [15] M. A. Anisimov, P. E. Cladis, E. E. Gorodetskii, D. A. Huse, V. E. P. V. G. Taratuta, W. van Sarloos, and V. P. Voronov, "Experimental test of a fluctuation-induced first-order phase transition: The nematic-smectic-A transition," *Phys. Rev. A* **41**, 6749–6762 (1990).
- [16] P. E. Cladis, W. van Sarloos, D. A. Huse, J. S. Patel, J. W. Goodby, and P. L. Finn, "Dynamical Test of Phase Transition Order," *Phys. Rev. Lett.* **62**, 1764–1767 (1989).
- [17] C. W. Garland and G. Nounesis, "Critical behavior at nematic–smectic-A phase transition," *Phys. Rev. E* **49**, 2964–2971 (1994).
- [18] J. A. Lipa and T. C. P. Chui, "Very High-Resolution Heat-Capacity Measurements near the Lambda Point of Helium," *Phys. Rev. Lett.* **51**, 2291–2294 (1983).
- [19] B. S. Andereck and B. R. Patton, "Anisotropic Critical Behaviour in a Model of the Nematic-Smectic A / Superconductor System," In *Bull. Am. Phys. Soc.*, (1999).
- [20] B. S. Andereck, "Anisotropy of the nematic-smectic A phase-transition," *Int. J. Mod. Phys. B* **9**, 2139–2155 (1995).
- [21] C. Dasgupta, "Numerical Studies of Phase-Transitions and Critical Phenomena in Liquid Crystals," *Int. J. Mod. Phys. B* **9**, 2219–2245 (1995).
- [22] M. A. Anisimov, "Critical Phenomena in Liquid Crystals," *Mol. Cryst. Liq. Cryst.* **162A**, 1–96 (1988).

- [23] P. E. Cladis, "Fluctuations and Liquid Crystal Phase Transitions," in *Physical Properties of Liquid Crystals*, D. Demus, J. W. Goodby, G. W. Gray, H.-W. Spiess, V. Vill, ed., (Wiley-VCH, 1999), pp. 277–288.
- [24] L. Onsager, "The effects of shape on the interactions of colloidal particles," *Ann. N. Y. Acad. Sci.* **51**, 627–659 (1949).
- [25] D. Frenkel, "Statistical mechanics of liquid crystals," in *Liquids, Freezing and Glass Transition Part II*, J. P. Hansen and D. Levesque and J. Zinn-Justin, ed., (Elsevier Science Publishers, 1989), pp. 689–762.
- [26] B. M. Mulder, "Density-functional approach to smectic order in an aligned hard-rod fluid," *Phys. Rev. A* **35**, 3095–3101 (1987).
- [27] B. M. Mulder and D. Frenkel, "The hard ellipsoid-of-revolution fluid. I. MonteCarlo Simulations," *Mol. Phys.* **55**, 1171–1192 (1985).
- [28] J. Tang and S. Fraden, "Magnetic-Field-Induced Isotropic-Nematic Phase Transition in a Colloidal Suspension," *Phys. Rev. Lett.* **71**, 3509–3512 (1993).
- [29] Z. Dogic and S. Fraden, "Smectic Phase in a Colloidal Suspension of Semiflexible Virus Particles," *Phys. Rev. Lett.* **78**, 2417–2420 (1997).
- [30] K. K. Kobayashi, "Theory of Translational and Orientational Melting with Application to Liquid Crystal," *J. Phys. Soc. Jpn.* **29**, 101–105 (1970).
- [31] W. L. McMillan, "Simple Molecular Model for the Smectic A phase of Liquid Crystals," *Phys. Rev. A* **4**, 1238–1246 (1971).
- [32] W. Maier and A. Saupe, "Eine einfache molekular-statistische Theorie der nematischen kristallinflüssigen Phase. Teil I," *Z. Naturforschg.* **14a**, 882–889 (1959).
- [33] W. Maier and A. Saupe, "Eine einfache molekular-statistische Theorie der nematischen kristallinflüssigen Phase. Teil II," *Z. Naturforschg.* **15a**, 287–292 (1960).
- [34] P. Sheng and E. B. Priestley, "The Landau-de Gennes Theory of Liquid Crystal Phase Transitions," in *Introduction to Liquid Crystals*, E. B. Priestley, P. J. Wojtowicz, and P. Sheng, eds., (Plenum Press, 1974), pp. 143–201.

- [35] C. Rosenblatt, "Magnetically Induced Nematic - Smectic A Tricritical Point," *J. Phys. (Paris) Lett.* **42**, L9-L12 (1981).
- [36] R. B. Meyer, B. Stebler, and S. T. Lagerwall, "Observation of Edge Dislocations in Smectic Liquid Crystals," *Phys. Rev. Lett.* **41**, 1393-1395 (1978).
- [37] T. C. Lubensky, "Soft Condensed Matter Physics," cond-mat/9609215, to appear in *Solid State Communications*, (1999).
- [38] W. G. Bouwman and W. H. de Jeu, "3D XY Behaviour of a Nematic-Smectic-A Phase Transition: Confirmation of the de Gennes Model," *Phys. Rev. Lett.* **68**, 800-803 (1992).
- [39] C. W. Garland, G. Nounesis, and K. J. Stine, "XY behaviour for the heat capacity at nematic-smectic-A1 liquid crystal transitions," *Phys. Rev. A* **39**, 4919-4922 (1989).
- [40] D. R. Nelson and J. Toner, "Bond-orientational order, dislocation loops, and melting of solid and smectic-A liquid crystals," *Phys. Rev. B* **24**, 363-387 (1981).
- [41] C. Dasgupta and B. I. Halperin, "Phase transition in a lattice model of superconductivity," *Phys. Rev. Lett.* **47**, 1556-1560 (1981).
- [42] B. S. Andereck and B. R. Patton, "Anisotropic renormalization of thermodynamic quantities above the nematic-smectic-A phase-transition," *Phys. Rev. E* **49**, 1393-1403 (1994).
- [43] B. R. Patton and B. S. Andereck, "Extended isotropic-to-anisotropic crossover above the nematic smectic-A phase-transition," *Phys. Rev. Lett.* **69**, 1556-1559 (1992).
- [44] J. Bartholomew, "Phase structure of a lattice superconductor," *Phys. Rev. B* **28**, 5378-5381 (1983).
- [45] T. C. Halsey and D. R. Nelson, "Nematic to smectic-A transitions with planar director fluctuations," *Phys. Rev. A* **26**, 2840-2853 (1982).
- [46] H. Marynissen, J. Thoen, and W. van Dael, "Experimental evidence for a nematic to smectic A tricritical point in alkylcyanobiphenyl mixtures," *Mol. Cryst. Liq. Cryst.* **124**, 195-203 (1985).

- [47] C. Dasgupta, "Critical-behavior of a lattice model of the nematic to smectic-A transition," *J. Phys. (Paris)* **48**, 957–970 (1987).
- [48] H. Kleinert and F. Langhammer, "Lattice model for the tricritical point of the nematic–smectic-A phase transition," *Phys. Rev. A* **40**, 5988–5997 (1989).
- [49] H. Kleinert and F. Langhammer, "Lattice model for layered structures," *Phys. Rev. A* **44**, 6686–6692 (1991).
- [50] J. Toner, "Renormalization-group treatment of the dislocation loop model of the smectic-A—nematic transition," *Phys. Rev. B* **26**, 462–465 (1982).
- [51] T. C. Lubensky and J. H. Chen, "Anisotropic critical properties of the de Gennes model for the nematic–smectic-A phase transition." *Phys. Rev. B* **17**, 366–376 (1978).
- [52] D. L. Johnson, C. Maze, E. Oppenheim, and R. Reynolds, "Evidence for a Smectic-A—Nematic Tricritical Point: Binary Mixtures," *Phys. Rev. Lett.* **34**, 1143–1146 (1975).
- [53] J. Thoen, H. Marynissen, and W. van Dael, "Nematic–smectic-A tricritical point in alkylcyanobiphenyl liquid crystals," *Phys. Rev. Lett.* **52**, 204–207 (1984).
- [54] I. Lelidis and G. Durand, "Electrically-induced isotropic-nematic-smectic-A phase-transitions in thermotropic liquid-crystals," *Phys. Rev. Lett.* **73**, 672–675 (1994).
- [55] A. Caillé, "Remarques sur la diffusion des rayons X dans les smectiques A," *C. R. Acad. Sc. Paris* **274B**, 891–893 (1972).
- [56] J. Als-Nielsen, R. J. Birgeneau, M. Kaplan, J. D. Litster, and C. R. Safinya, "High-Resolution X-Ray Study of a Second-Order Nematic–Smectic-A Phase Transition," *Phys. Rev. Lett.* **39**, 352–355 (1977).
- [57] C. W. Garland, M. Meichle, B. M. Ocko, A. R. Kortan, C. R. Safinya, L. J. Yu, J. D. Litster, and R. J. Birgeneau, "Critical behavior at the nematic–smectic-A transition in butyloxybenzylidene heptylaniline (4O.7)," *Phys. Rev. A* **27**, 3234– (1983).

- [58] W. G. Bouwman and W. H. de Jeu, "Difference in the critical behaviour of the phase transitions nematic-smectic  $A_1$  and nematic-smectic  $A_d$ ," *J. Phys. II* **4**, 787–804 (1994).
- [59] T. C. Lubensky, "The nematic–smectic-A Transition: A theoretical overview," *J. Chim. Phys. (Paris)* **80**, 31 (1983).
- [60] C. Gooden, R. Mahmood, D. Brisbin, A. Baldwin, D. L. Johnson, and M. E. Neubert, "Simultaneous Magnetic-Deformation and Light-Scattering Study of Bend and Twist Elastic-Constant Divergence at the Nematic–Smectic-A Phase Transition," *Phys. Rev. Lett.* **54**, 1035–1038 (1985).
- [61] R. Mahmood, D. Brisbin, I. Khan, C. Gooden, A. Baldwin, and D. L. Johnson, "Light-scattering Study of the Nematic Twist Constant near the Smectic-A Transition," *Phys. Rev. Lett.* **54**, 1031–1034 (1985).
- [62] M. Benzekri, T. Claverie, J. P. Marcerou, and J. C. Rouillon, "Nonvanishing of the Layer Compressional Elastic Constant at the Smectic-A-to-Nematic Phase Transition: A Consequence of Landau-Peierls Instability?," *Phys. Rev. Lett.* **68**, 2480–2483 (1992).
- [63] S. K. Ma, *Statistical Mechanics*. 1st ed. (World Scientific, Singapore, 1985).
- [64] P. Martinoty, J. L. Gallani, and D. Collin, "Hydrodynamic and Nonhydrodynamic Behaviour of Layer Compression Modulus  $B$  at the Nematic-Smectic-A Phase Transition in 8OCB," *Phys. Rev. Lett.* **81**, 144–147 (1998).
- [65] J. Thoen, H. Marynissen, and W. van Dael, "Temperature dependence of the enthalpy and the heat capacity of the liquid-crystal octylcyanobiphenyl (8CB)," *Phys. Rev. A* **26**, 2886–2905 (1982).
- [66] C. W. Garland, "High-Resolution Ac Calorimetry And Critical-Behavior At Phase-Transitions," *Thermochimica Acta* **88**, 127–142 (1985).
- [67] P. Brisbin, R. DeHoff, T. E. Lockhart, and D. L. Johnson, "Specific-Heat Near The Nematic-Smectic-A Tricritical Point," *Phys. Rev. Lett.* **43**, 1171–1174 (1979).

- [68] K. J. Stine and C. W. Garland, "Calorimetric study of nematic-smectic-A tricritical behaviour," *Phys. Rev. A* **39**, 3148–3156 (1989).
- [69] N. Tamblyn, P. Oswald, A. Miele, and J. Bechhoefer, "Investigating the Nematic-Smectic-A Transition by Capillary-Length Measurements Near An Apparent Tricritical Point," *Phys. Rev. E* **51**, 2223–2236 (1995).
- [70] N. Tamblyn, "Is the Nematic-Smectic-A Transition Always First Order? Measurements of Surface Tension Near an Apparent Tricritical Point," M.Sc. thesis, Simon Fraser University, 1994.
- [71] M. Marinelli, F. Mercuri, U. Zammit, and F. Scudieri, "Dynamical critical behaviour of thermal parameters at the smectic-A-nematic phase transition," *Phys. Rev. E* **53**, 701–705 (1996).
- [72] M. Marinelli, F. Mercuri, S. Foglietta, U. Zammit, and F. Scudieri, "Anisotropic heat transport in the octylcyanobiphenyl (8CB) liquid crystal," *Phys. Rev. E* **54**, 1–6 (1996).
- [73] Y. Poggi and J. C. Filippini, "Magnetic-Field Dependence of the Order Parameter in a Nematic Liquid Single Crystal," *Phys. Rev. Lett.* **39**, 150–152 (1977).
- [74] I. Lelidis, M. Nobili, and G. Durand, "Electric-field-induced change of the order-parameter in a nematic liquid-crystal," *Phys. Rev. E* **48**, 3818–3822 (1993).
- [75] P. G. de Gennes, "Fluctuations d'orientation et diffusion Rayleigh dans un cristal nématique," *C. R. Acad. Sci., Ser. B* **266**, 15–17 (1968).
- [76] I. Lelidis and G. Durand, "Electric-field-induced isotropic-nematic phase-transition," *Phys. Rev. E* **48**, 3822–3824 (1993).
- [77] I. Lelidis, "Transitions de phases induites par un champ électrique dans les cristaux liquides," Ph.D. thesis, Université de Paris-Sud U.F.R. Scientifique D'Orsay, 1994.
- [78] B. M. Ocko, R. J. Birgeneau, and J. D. Litster, "Crossover to tricritical behaviour at the nematic to smectic A: An x-ray scattering study," *Z. Phys. B* **62**, 487–497 (1986).

- [79] R. Mukhopadhyay, A. Yethiraj, and J. L. Bechhoefer, "External-field-induced tricritical point in a fluctuation-driven nematic-smectic-A transition," cond-mat/9905045, submitted to Phys. Rev. Lett. (1999).
- [80] M. A. Anisimov, V. P. Voronov, E. E. Gorodetskii, and V. E. Podnek, "Observation of the Halperin-Lubensky-Ma effect in a liquid crystal," JETP Lett. **45**, 425-429 (1987).
- [81] H. Hama, "Effects of a Magnetic Field on the Nematic-Smectic-A Transition in Liquid Crystals," J. Phys. Soc. Jpn. **54**, 2204-2209 (1985).
- [82] A. Yethiraj and J. Bechhoefer, "Using nematic director fluctuations as a sensitive probe of the Nematic-Smectic-A Phase Transition in Liquid Crystals," Mol. Cryst. Liq. Cryst. **304**, 301-307 (1997).
- [83] MK1-SI; Instec Inc., 1898 S. Flatiron Court, Boulder, CO 50301, U.S.A., Tel: (303)444-2564, Fax: (303)541-9354, <http://www.instec.com>.
- [84] MSPlan 10; Olympus Corp., Two Corporate Center Drive, Melville, NY 11747-3157 U.S.A., Tel: (516)844-5000, Fax: (516)844-5930, <http://www.olympus.com>.
- [85] A. Bailey, "Early Stage Spinodal Decomposition," Ph.D. thesis, University of California, Santa Barbara, 1993.
- [86] LS 1130-4, EG&G Electro-optics, 35 Congress St., Salem, MA 01970, U.S.A., Tel: (508)745-2000, Fax: (508)745-0894, <http://www.egginc.com>.
- [87] EG&G Electro-optics Datasheets, EG&G Electro-optics, 35 Congress St., Salem, MA 01970, U.S.A., Tel: (508)745-2000, Fax: (508)745-0894, <http://www.egginc.com>.
- [88] S. Inoué and K. R. Spring, *Video Microscopy: The Fundamentals*, 2nd ed. (Plenum Press, New York, 1997).
- [89] G. W. Ellis, "Microscope Illuminator with Fiber Optic Source Integrator," Journal of Cell Biology **101**, 83A (1985).
- [90] Optical Coating Laboratory, Inc., 2789 Northpoint Parkway, Santa Rosa, CA 95407-7397, Tel: (707) 545-6440, Fax: (707) 525-7410, <http://www.ocli.com>.

- [91] BK7 glass cubes; Esco Products Inc., 171 Oak Ridge Road, Oak Ridge, NJ 07438, USA, Tel: (973)697-3700, Fax: (973)697-3011, <http://www.escoproducts.com/index.html>.
- [92] KAF1400 Sensys camera; Photometrics, 3440 East Britannia Dr., Tucson, Arizona 85706, U.S.A., Tel: (520)889-9933, Fax: (520)295-0299, <http://www.photometrics.com>.
- [93] Macintosh G3 Computer.
- [94] IPLAB Spectrum Image-Processing software, Scanalytics Inc., <http://www.scanalytics.com>.
- [95] Igor Pro v3.1, Wavemetrics Corp., <http://www.wavemetrics.com>.
- [96] Klinger-Newport Optics, 1171 Deere Ave., Irvine, CA 92606, U.S.A., Tel: (714)863-3144, Fax: (714)253-1680, <http://www.newport.com>.
- [97] R. C. Weast, *Handbook of Chemistry and Physics*, 53rd ed. (CRC Press, Cleveland, Ohio, 1972).
- [98] J. A. Dean, *Lange's Handbook of Chemistry*, thirteenth ed. (McGraw Hill Book Company, New York, 1985).
- [99] M. Marinelli, F. Mercuri, U. Zammit, and F. Scudieri, "Thermal conductivity and thermal diffusivity of the cyanobiphenyl (nCB) homologous series." *Phys. Rev. E* **58**, 5860–5866 (1998).
- [100] Neslab RTE-110, Neslab Instruments Inc., 25 Nimble Rd., Newington, NH 03801, U.S.A., Tel: (603)427-2877, Fax: (603)436-8411.
- [101] W2152 (2000 ohm) Thinfilm Platinum RTD; Omega Engineering, Inc., One Omega Drive, P.O. Box 4047, Stamford, CT 069707-0047, U.S.A.; Tel: (1-800) 826-6342, Fax: (203) 359-7980, <http://www.omega.com>.
- [102] Melcor Corp., 1040 Spruce St., Trenton, N.J. 08648, U.S.A., Tel: (216)248-0400, Fax: (216)248-6168, <http://www.melcor.com>.

- [103] Maxell SR1130W 1.55 V Micro Silver Oxide Battery.
- [104] Model 2001; Keithley Instruments Inc., Instruments Div., 28755 Aurora Rd., Cleveland, Ohio 44139, U.S.A., Tel: (216)248-0400, Fax: (216)248-6168, <http://www.keithley.com>.
- [105] SR850 DSP Lock-in Amplifier; Stanford Research Systems, 1290 D Reamwood Ave., Sunnyvale, CA 94089, Tel: (408)744-9040, Fax: (408)744-9049, <http://www.wombat.net/srsys/>.
- [106] National Instruments, 11500 N Mopac Expwy, Austin, TX 78759-3504, Tel: (512)794-0100, Fax: (512)683-8411, <http://www.natinst.com>.
- [107] XTD 15-4 power supply, Xantrex, 8587 Baxter Place, Burnaby, British Columbia, Canada V5A4V7, Tel: (604) 421 3031, Fax: (604) 421 3029, <http://www.xantrex.com>.
- [108] Prime Technology Inc., P.O. Box 185, Twin Lakes Rd., North Branford, CT 06471, U.S.A.. Tel: (203)481-5721.
- [109] K. Dutton, S. Thompson. and B. Barraclough, *The Art of Control Engineering*, 1st ed. (Addison-Wesley Press, Essex, 1997).
- [110] Micro-90, International Products Corp., P.O.Box 70, Burlington, NJ 08016-0070, U.S.A., Tel: (609)386-8770, Fax: (609)386-8438.
- [111] Branson 1200, Branson Ultrasonics Corp., P.O.Box 1961, Danbury CT 06813-1961, U.S.A., Tel: (203)796-0400.
- [112] Kimwipes EX-L wipers; Kimberly-Clark Corp., Roswell, GA 30076-2199, U.S.A.
- [113] Simco static neutralising gun; Simco, 257 N. Penn Rd., Hatfield, PA 19440-1998, Tel: (215)822-2171, Fax: (215)822-3795, <http://www.simco-static.thomasregister.com/olc/simco-static/home.htm>.
- [114] D. W. Berreman, "Solid Surface Shape and the Alignment of an Adjacent Nematic Liquid Crystal," *Phys. Rev. Lett.* **28**, 1683-1686 (1972).
- [115] J. L. Jannings, "Thin film surface orientation for liquid crystals," *App. Phys. Lett.* **21**, 173 (1972).

- [116] Auto Tech II; C.H.A. Industries, 4201 Business Center Drive, Fremont, CA 94538, U.S.A., Tel: (510) 683-8554, Fax: (510) 683-3848, <http://www.chaindustries.com>.
- [117] R. D. Mathis and Co., 2840 Gundry Ave., Long Beach, CA 90806, U.S.A., Tel: (310) 426-7049.
- [118] CERAC Inc., 407 N.13th St., Milwaukee, WI 53233, U.S.A., Tel: (414)289-9800, Fax: (414)289-9805.
- [119] Fisher Isotemp 500; Fisher Scientific. Tel: (800)234-7437, Fax: (800)463-2996, <http://www.fishersci.ca>.
- [120] Liquicoat PI kit ZLI 2650; E. Merck, D-6100 Darmstadt, Germany. Tel: (061 51)72-3360, Fax: (061 51)72-1171.
- [121] A. A. Sonin, private communication.
- [122] J. Cognard, "Alignment of Nematic Liquid Crystals and Their Mixtures." *Mol. Cryst. Liq. Cryst. Suppl. Ser. 1*, 1-77 (1982).
- [123] NOA 91; Norland Products Inc., 695 Joyce Kilmer Ave., New Brunswick, NJ 08902, U.S.A., Tel: (908)545-7828, <http://www.norlandprod.com>.
- [124] NOA 61; Norland Products Inc., 695 Joyce Kilmer Ave., New Brunswick, NJ 08902, U.S.A., Tel: (908)545-7828, <http://www.norlandprod.com>.
- [125] D. H. van Winkle and N. A. Clark, "Direct Measurement of Orientational Correlations: Observation of the Landau-Peierls Divergence in a Freely Suspended Tilted Smectic Film," *Phys. Rev. Lett.* **53**, 1157-1160 (1984).
- [126] I. Rehberg, S. Rasenat, W. S. M. de la Juárez, G. Ahlers, and H. R. Brand, "Thermally Induced Hydrodynamic Fluctuations below the Onset of Electroconvection," *Phys. Rev. Lett.* **67**, 596-59 (1991).
- [127] U. Bisang and G. Ahlers, "Bifurcations to Worms in Electroconvection," preprint, (1999).

- [128] Y. Galerne, I. Poinsoot, and D. Schaegis, "Direct absolute measurements of the two-dimensional elastic constants in smectic-*C*" films," *App. Phys. Lett.* **71**, 221–224 (1997).
- [129] A. P. Y. Wong and P. Wiltzius, "Dynamic light scattering with a CCD camera," *Rev. Sci. Inst.* **64**, 2547–2550 (1993).
- [130] NIH Image, Image-Processing Software, Wayne Rasband, National Institute of Health, U.S.A., <http://www.rsb.info.nih.gov/nih-image>.
- [131] "High Performance CCD Cameras"; Princeton Instruments, Inc. (1995).
- [132] T. W. Stinson and J. D. Litster, "Pretransitional phenomena in the Isotropic Phase of a Nematic Liquid Crystal," *Phys. Rev. Lett.* **25**, 503–506 (1970).
- [133] T. W. Stinson and J. D. Litster, "Correlation Range of Fluctuations of Short-Range Order in the Isotropic Phase of a Liquid Crystal," *Phys. Rev. Lett.* **30**, 688–692 (1973).
- [134] B. Jaggi, B. Pontifex, J. Swanson, and S. S. S. Poon, "Performance Evaluation of a 12-Bit, 8Mpel/s Digital Camera," *SPIE* **1901**, 99–108 (1993).
- [135] P. P. Karat and N. V. Madhusudana, "Elastic and Optical Properties of some 4'-n-alkyl-4-cyanobiphenyls." *Mol. Cryst. Liq. Cryst.* **36**, 51–64 (1976).
- [136] R. Mukhopadhyay, private communication.
- [137] P. Galatola, "Light-scattering in anisotropic stratified media," *Phys. Rev. E* **49**, 4552–4562 (1994).
- [138] V. V. Belyaev, S. A. Ivanov, and M. F. Grebenkin, "Temperature dependence of rotational viscosity  $\gamma_1$  of nematic liquid crystals," *Kristallografiya* **30**, 674–680 (1985).
- [139] TM-7CN 8-bit CCD Camera; Pulnix America Inc., 1330 Orleans Drive, Sunnyvale, CA 94089, U.S.A., Tel: (408)747-0300, Fax: (408)747-08806, <http://www.pulnix.com>.
- [140] Linkam Systems, 8 Epsom Downs, Metro Centre, Waterfield, Tadworth, Surrey, KT205HT, U.K., Tel: 440-1737-363476, Fax: 440-1737-363480, <http://www.linkam.co.uk>.

- [141] L. Benguigui, "The cholesteric-smectic-A transition," *Liq. Cryst.* **25**, 1 (1998).
- [142] H. J. Coles and M. S. Sefton, "Pretransitional Behavior Of The Splay And Twist Elastic And Viscotic Constants For The Nematic To Smectic A Phase-Transition In Octyl Cyanobiphenyl (8CB)," *Mol. Cryst. Liq. Cryst.* **4**, 123-130 (1987).
- [143] M. J. Bradshaw, E. P. Raynes, J. D. Bunning, and T. E. Faber, "The Frank constants of some nematic liquid crystals," *J. Phys. (Paris)* **46**, 1513-1520 (1985).
- [144] D. Davidov, C. R. Safinya, M. Kaplan, S. S. Dana, R. Schaetzing, R. J. Birgeneau, and J. D. Litster, "High-resolution x-ray and light-scattering study of critical behaviour associated with the nematic-smectic-A transition in 4-cyano-4'-octylbiphenyl," *Phys. Rev. B* **19**, 1657-1663 (1979).
- [145] P. P. Karat and N. V. Madhusudana, "Elasticity and Orientational Order in some 4'-n-alkyl-4-cyanobiphenyls: Part II," *Mol. Cryst. Liq. Cryst.* **40**, 239-245 (1977).
- [146] A. Buka and W. H. de Jeu, "Diamagnetism and orientational order of nematic liquid crystals," *J. Phys. (Paris)* **43**, 361-367 (1982).
- [147] A. J. Leadbetter, J. L. A. Durrant, and M. Rugman, "The density Of 4 n-Octyl-4'-Cyano-Biphenyl (8CB)," *Mol. Cryst. Liq. Cryst.* **34**, 231-235 (1977).
- [148] A. Zywockinski and S. A. Wiczorek, "Critical Exponents for Thermal Expansion and Isothermal Compressibility near the Nematic to Smectic-A Transition," *J. Phys. Chem. B* **101**, 6970-6976 (1997).
- [149] H. Schad and G. Meier, "Investigation of the dielectric constants and the diamagnetic anisotropies of cyanobiphenyls (CB), cyanophenylcyclohexanes (PCH), and cyanocyclohexylcyclohexanes," *J. Chem. Phys.* **71**, 3171-3181 (1979).
- [150] S. Sprunt, L. Solomon, and J. D. Litster, "Equality of X-Ray and Light Scattering Measurements of Coherence Lengths at the Nematic-Smectic-A Phase Transition," *Phys. Rev. Lett.* **53**, 1923-1926 (1984).
- [151] M. Abramowitz and I. A. Stegun, *Handbook of Mathematical Functions*, ninth ed. (Dover, New York, 1972).